PMAI

www.pmai.in

TRANSACTIONS OF POWDER METALLURGY ASSOCIATION OF INDIA

Vol. 40 No.2, December 2014

Chief Editor - P. Ramakrishnan

PMAI

www.pmai.in

TRANSACTIONS OF POWDER METALLURGY ASSOCIATION OF INDIA

Chief Editor - P. Ramakrishnan

Powder Metallurgy Association of India

Office Bearers

President
  Mr. N. Gopinath

Vice President
  Mr. N. Chandrachud
  Mr. D. Grover
  Mr. R.K. Kandoi

General Secretary
  Dr. Deep Prakash

Hon. Treasurer
  Dr. Murli Gopal K.

Joint Secretary
  Mr. Aniket Gore
  Mr. Jayesh Patel

Price Rs. 500/-

Editorial

Transactions PMAI Vol. 40. No. 2. 2014 features the papers from the International Conference & Exhibition and 40th Annual Technical Meeting held at Hotel Le Royal Meridian, Chennai during Jan. 2014. The transaction cover wide topics from synthesis of powders, important behavior of powders, densification, furnace atmospheres, sintering process to modeling IT solutions.

Initial presentation describe the importance of spherical WC-Co powders for coating applications produced by spray agglomeration of the milled powders, the electrochemical behavior of nano structural Mg_2Ni_xNb inter metallic compound synthesized by high energy ball milling. The next paper deals with surface modification approach to enhance the bioactivity and antibacterial property of Titanium metal by incorporating silver nanoparticles which will find applications in various orthopedic implants.

Important patented work on furnace atmosphere control system developed by Linde and Höganäs for the successful control of carbon potential in sintering process to facilitate a higher quality product at a lower production cost and the densification mechanism in spark plasma sintering of oxide dispersion strengthened martensitic stainless steel will be of interest to readers.

This is followed by a paper dealing with the consolidation of mechanically alloyed Al-5083, nano- Yttria composite by equal channel angular pressing and a paper on the effect of Tungsten content on the microstructure and mechanical properties of Co containing heavy alloys with varying Tungsten. Hot forging studies on Al-2.5%TiO_2.Gr hybrid powder metallurgy composite is dealt with in the next paper. This is followed by an article on continuous hot isostatic pressing-possible design, which is expected to make hipping a more affordable manufacturing process. The wok on a comparative study of nano size reinforcement on peak broadening analysis of Al-6061 alloy reinforced with 2 Wt. % TiC and 2 Wt % Al_2O_3 is illustrated in the nest paper.

Impregnated agglomerate pelletization technique has been developed for advanced fuel fabrication facility for manufacturing UO_2 mixed oxide fuel pellets in comparison with other routes such as coated agglomerate pelletization and powder oxide pelletization. This new process will reduce the powder handling and improve the homogeneity of the fuel pellets. The next paper highlights the Ti (TiB + TiC) composites prepared by sintering of Titanium and B_4C compacts and their corrosion behavior. This is followed by a paper on investigation of piezoelectric and dielectric properties of Strontium doped lead free piezoelectric BNKT ceramics. The final paper is on the IT solutions to ware house design approach and the optimization of the same is expected to result in cost effective operations.

P. Ramakrishnan.

CONTENTS

PROCESSING OF SPHERICAL POWDERS OF WC-Co FOR COATING APPLICATIONS

Aditya Kavalur and P S Jayan

Electro Minerals Division, Carborundum Universal Limited, Chennai, India

Abstract: *Coating applications using WC-Co cermets require powders with high and consistent flowability, which are characteristic of nearly dense spherical powders. However, most milling systems tend to produce irregular shaped-particles. To address this concern, powders are milled to finer than required sizes and then aggregated to a spherical shape of the required size. Spray agglomeration used in this work enables fabrication of powders with different constituents through co-drying of mixed slurries. This aggregation can be provided temporary green strength through the addition of a binder. The rapid heat and mass transfer which occurs during spray drying combined with the slurry stability and viscosity, decides the shape and size of the dried powders. A study has been performed on the effect of slurry properties and spray drying variables to obtain near spherical powders suitable for coating applications. Experiments were performed with different slurry media (Acetone and Water), slurry viscosities and spray drying temperatures to study their effect on the size of the aggregation as well the shape. Mostly dense spherical powders were obtained (due to the dispersion state). However, the afore-mentioned variables had a considerable effect on the sizes produced. The chemical integrity of the powders post-spray drying was examined through XRD. The main concern during processing of WC-Co is the pickup of Oxygen either in free or combined state which leads to the oxidation of Cobalt and Tungsten, especially in aqueous media and/ or at elevated temperatures and/ or acidic pH solution. Earlier works have focused on dissolution and depths of surface oxidation of WC and Co powders in all these conditions. The present work focuses on building further, to develop an Industry acceptable WC-Co grade.*

Keywords: *WC-Co, Spray Drying, Wear Coating, Thermal Spraying*

1. Introduction

Tungsten Carbide-Cobalt powders are widely used for high wear resistant coatings for low temperature exposure surfaces such as pump housings, steel rolls, sink rolls, exhaust fans, conveyor screws, sucker rod couplings etc. [1]. Due to the severe shortage of Tungsten Carbide, many reclaiming processes have been developed, in which scrap parts of WC-Co composition are refined to near original purity, the most popular among these methods is Zinc Melt Method which produces powders of sufficient purity to be utilized for the wear resistant coating applications [2]. These coatings are generally done using HVOF (High Velocity Oxy-Fuel) technique where it is essential to have a powder with high density and good flowability, to get dense and even coating. Powder physical properties especially powder morphology, size distribution, density

have been shown to have great effect on not only the deposition efficiency but also the coating characteristics [3]. So it is essential to optimize the same for any powder producer. Agglomeration of powders through spray drying have been used to produce various shapes: elongates, spherical, irregular as well as dense or hollow structures[4].
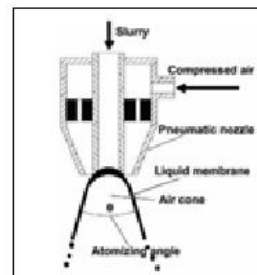

Fig 1: Schematic diagram of pneumatic nozzle and formation of droplets [5]

The two-fluid nozzle shown in Fig. 1 shows the technique of atomization adopted, where liquid slurry is vigorously agitated at the tip of the nozzle with a circumferential column of compressed air to produce droplets which dry in a heated atmosphere without coming into contact with any surface.

2. Experimental Procedure

Materials

Two pre-cursor powders WC & Co were selected with a combined average size < 3 μm, the Cobalt powders were being suitably finer to facilitate the binding in the coating application. The slurry preparation was done through addition of appropriate aqueous or acetone based binders to the slurry media, after which the powder was slowly added, and stirred for 1 hour to obtain homogeneity. The pH of the solution was adjusted with diluted solutions of HCl (1N) or NaOH (1N). Different solid loading percent of the powders in aqueous media were studied to monitor their viscosities.

Spray Drying

The spray drying trials were carried out in a 2 kg/h lab scale spray drier. The atomization was attained through a two-fluid nozzle, with a 2 bar atomization pressure while the feed rate was maintained at 1l/h for all the trials. For studying the effect of solid loading percentage on the mean size the inlet temperature was maintained at 225°C for the aqueous based slurries and 150°C for the acetone based trials as higher temperatures lead to nozzle blockage resulting from the rapid evaporation of acetone. The solid loading percentage in the slurry was varied from 25wt% to 66.67wt%. Subsequently inlet temperature was varied while maintaining a 50% solid loading percentage to between 175–225°C, reducing the inlet temperature below a certain limit leads to a substantial increase in the amount of retained moisture of the powders, which reduces its green strength. Only product collected in the chamber outlet was considered for analysis as the output of the cyclone is mostly un-agglomerated and hence fit only for recycling.

3. Results and Discussion

The mean size of the spray dried agglomerates showed a direct correlation with the solid loading percentage and slurry viscosity (Figs. 2 and 3), with an increase in the solid content leading to an increase in the mean size.
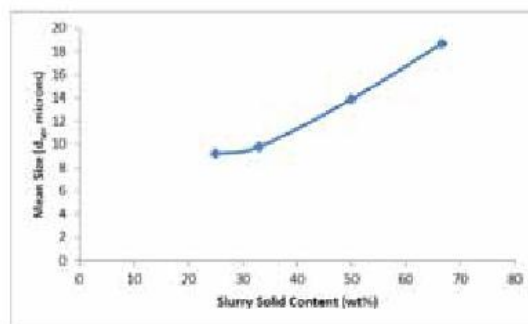
Fig 2: Mean Size (microns) of chamber product of Spray Drying vs Slurry solid content (wt% - WC-Co powder)
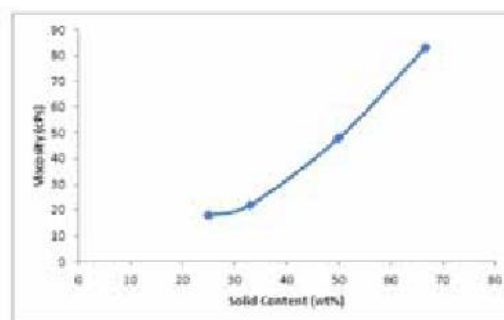
Fig 3: Viscosity (cPs) vs Slurry Solid Content (wt% - WC-Co powder)

This can be explained through factors such as mechanism of atomization and increased powder/ dispersion media ratio. This is because the higher solid loading percent slurry had a higher viscosity and required more energy to produce the droplets due to its higher surface tension. The atomization pressure being constant, the increased slurry viscosity resulted in larger droplets of the powder. Secondly, the higher powder/ dispersion-media i.e. higher volume% of solid in the slurry meant that in

the bigger droplets there was a further increase in the amount of powder present. Since the surface charge and other powder related properties were kept constant for both the trials, the slurry stability and ergo the dried powder interaction i.e. the inter particle affinity/ distance were expected to be the same resulting in an increase in the size of the powder obtained after drying.
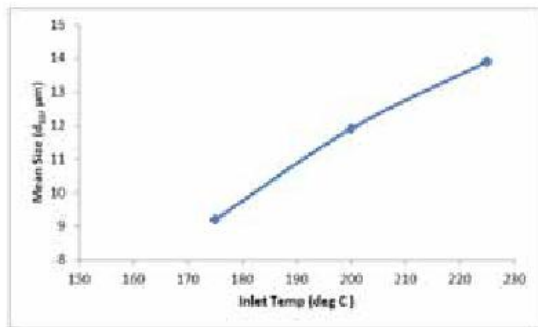
Fig. 4: Inlet air temperature vs Mean size of powders

Fig. 4 shows mean size of particles as a function of inlet air temperature. The increase in the mean size of powders with the increase in the inlet temperature could be due to the enhanced diffusion rate of the moisture and PVA towards the outer surface of the droplet in comparison with the evaporation rate of the moisture at the surface. As the PVA doesn't evaporate, its concentration on the surface layer increased which had a negative effect on the evaporation rate of moisture and ergo on the shrinkage of the powder. The above mechanism lead to surface hardening of the droplet at substantially reduced times, thus not providing enough time for its shrinkage. SEM images of initial and spray-dried powders are shown in Fig. 5(a)&(b).
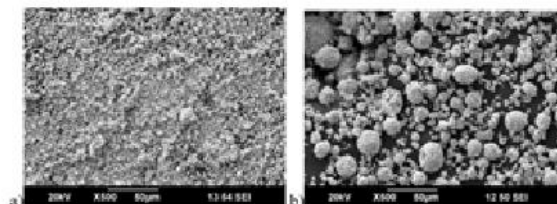
Fig 5: SEM images of WC-Co: a) Initial powder, b) Spray-dried powder

The chemical stability of the powders in particular their Oxygen content is important. It has earlier been shown that WC and Co powders have a tendency to oxidize and dissolve in water [6]. The oxygen content was measured through EDX technique for surface content [Fig. 6(a)& (b)]. It was found that oxygen content on the surface had substantially increased from 5% to 10%(atom%) during the spray drying in aqueous slurry as compared to acetone based slurry where there was not much change.
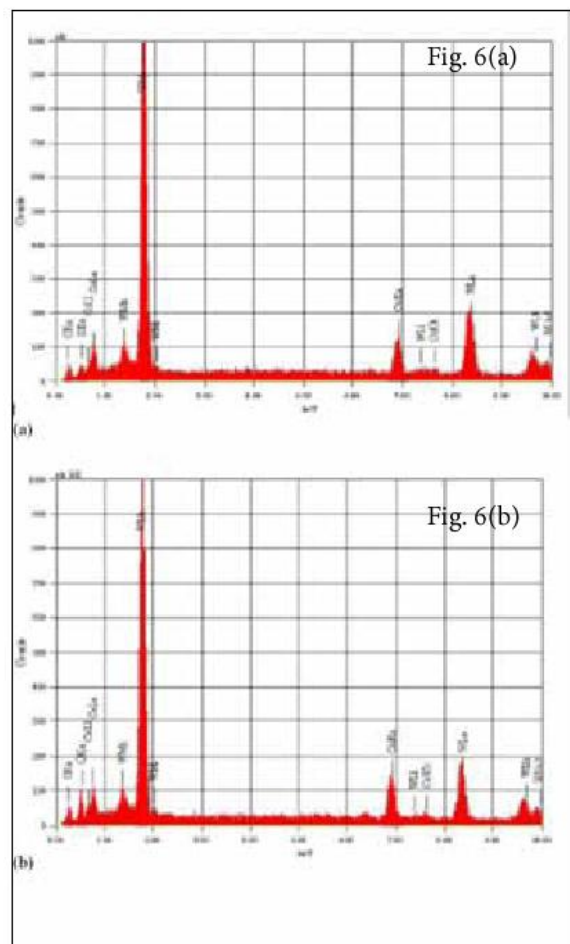
Fig 6: a) Feed powder, b) Water Spray Dried (Inlet air-225oC, solid loading -66.67 wt%),

Fig. 6(c)

Fig. 6(d)
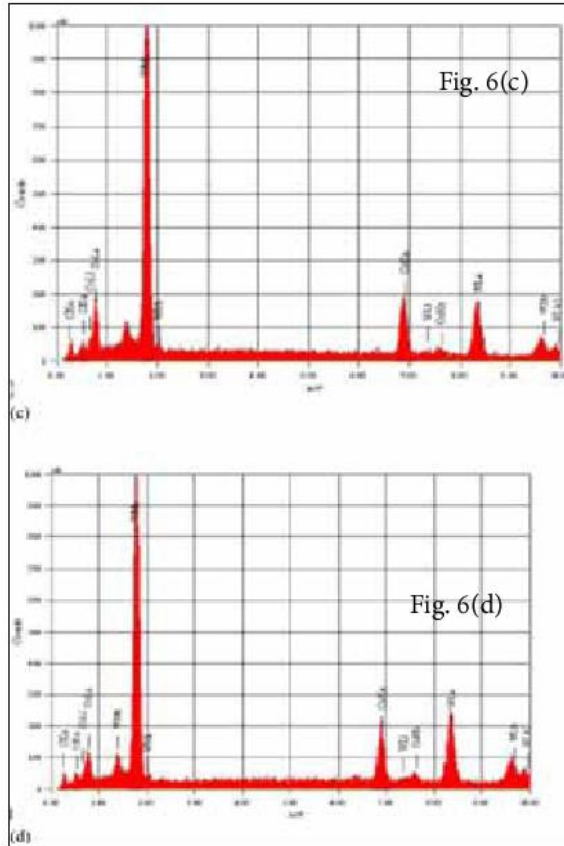
Fig 6: c) Acetone Spray Dried (Inlet air – 1 65 oC, solid loading – 66.67 wt%), d) Heating in air (100 oC)

Material	Oxygen content	
	Mass %	Atom %
Feed	0.87	5.04
Water Slurry	2.02	10.4
Acetone Slurry	0.76	4.41
Air heating (100C)	1.08	5.91

Table 1: Oxygen content measured through EDX technique

Heating of spray-drying feed powders in open atmosphere to spray drying temperatures (& similar holding time, approx. 2 minutes) showed similar oxygen levels as the acetone based powders and the feed, confirming that the majority adsorption of oxygen was from its high-temperature exposure to water during spray drying rather than air.
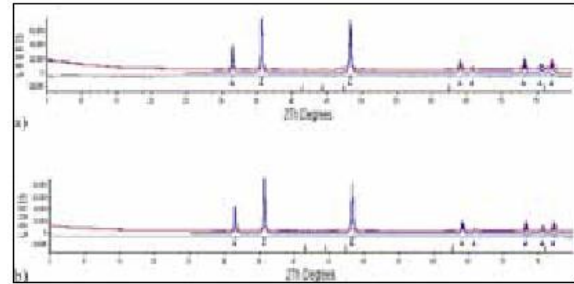
Fig 7: XRD analysis - a) before Spray Drying, b) after Spray Drying through aqueous slurry

However the XRD analysis of the feed and the aqueous slurry based spray dried powder shows identical results indicating that the oxygen adsorbed was majorly in the free state and had not formed substantial compounds of CoO, Co_3O_4, WO_3. (Fig. 7)

4. Acknowledgement

5. References

1. Thermal Spray Materials Guide, Sulzer Metco, May 2012

2. Ekrem Altuncu, Fatih Ustel, Ahmet Turk, Savas Ozturk and Garip Erdogan,. "Cutting tool recycling process with the Zinc-Melt method for obtaining Thermal Spray feedstock powder", Materials and Technology Vol. 47(1), 115-118 (2013)

3. Batur Ercan, Keith J. Bowman, Rodney W. Trice, Hsin Wang and Wally Porter "Effect of Initial powder morphology on thermal & mechanical properties of stand-alone plasma sprayed 7wt% Y_2O_3-ZrO_2 coatings", Materials

Science & Engineering A Vol. 435–436, 212-220 (2006).

4. Masters, K, Spray Drying Handbook, 4th Edition. Wiley, NY (1985).

5. Bai Yu, Yang Jian Feng, Lee Soo Wohn, Chen Huang, Yu Fang Li and Zhang Jia,. "Spray-Drying of alumina powder for APS: effect of slurry properties and drying conditions upon particle size and morphology of feedstock". Bulletin of Materials Science, 34(7), 1653-1661 (2011).

6. Karim M Andersson and Lennart Bergstrom, "Oxidation & Dissolution of Tungsten Carbide powders in Water". International Journal of Refractory Metals & Hard Materials 18, 121-129 (2000).

SYNTHESIS OF NANOSTRUCTURED Mg_2Ni_xNb INTERMETALLIC COMPOUND BY HIGH ENERGY BALL MILLING AND TO STUDY ITS ELECTRO-CHEMICAL BEHAVIOUR

A.Venkateswari, S.Kumaran

Department of Metallurgical and Materials Engineering, National Institute of Technology, Tiruchirapalli, India

Abstract: *The scope of this work is to understand the electrochemical behaviour of nanostructured Mg_2Ni_xNb intermetallic compound synthesised by high energy ball milling. Ball milling was carried at optimised milling parameters namely milling speed, ball-to-powder ratio, milling time, etc. The powders were characterised by X-ray diffraction (XRD), scanning electron microscopy (SEM), potentiostat/ galvanostat and differential thermal analysis (DTA). High energy ball milling had resulted in formation of nano-structured Mg_2Ni_xNb intermetallic compound at 30hrs. The particle size was reduced to 0.5µm with increasing milling time. Electrochemical study shows that the nanostructured Mg_2Ni compound obtained at 30hrs exhibits higher discharge capacity when compared to nanostructured Mg_2Ni compound of 50hrs milling. This is mainly due to the agglomeration of the later powder particles. DTA analysis also supports the fact that particle size influences discharge capacity since the nanostructured Mg_2Ni intermetallic compound exhibits relatively a superior enthalpy of $49.721 kJmol^{-1}$ when compared to 50 hrs milled powders ($19.91 kJmol^{-1}$).*

Keywords: *High energy ball milling, X-ray diffraction, Scanning electron microscopy, Electrochemicalanalysis, Differential thermal analysis*

1. Introduction

The idea of this work is to find ways and means to convert our transportation system from the one dominated by oil to one dominated by hydrogen, which can substantially reduce the sensitivity of our current global energy supply network to geopolitical instabilities, and provide an answer to the continuing depletion of our fossil fuel reserves [1]. The amount of research activity in the hydrogen storage field has increased substantially over the last decade or so, primarily due to the practical need for a hydrogen storage method suitable for use in hydrogen fuel cell cars and other hydrogen-based transportation technology. Hydrogen can store a large amount of chemical energy per unit mass but under ambient conditions it exists in its pure form only as a low density gas. As a consequence, a number of studies have identified the problem of storing hydrogen as a fuel, wherein posing a major threat for the smooth transition from a fossil fuel-based transportation system to one in which hydrogen is the principal

energy carrier [2-5]. This so-called hydrogen energy transition is seen by many as the answer to the numerous problems associated with our current reliance on oil, which include its finite nature and issues such as energy security and climate change. The international effort to accelerate this transition is well underway, with the recent introduction of the Honda FCX Clarity, the first production hydrogen fuel cell car, leading the way towards wider commercialization of hydrogen fuel cell technology by the automotive industry. Vehicles powered by these fuel cells produce only water as a waste product, and so a further significant benefit is the elimination of the harmful and polluting effects of the exhaust fumes from petroleum-based Internal Combustion Engines (ICEs). In the case of the latter, the storage of hydrogen in a solid state material is a very promising potential solution, and the discovery or development of a highly efficient reversible hydrogen storage material would therefore mark a step change in the transition to a hydrogen-fuelled future [6-9]. The target is a material that can satisfy

the tough demands of a practical hydrogen store for use in the automotive transportation sector: one that can store large amounts of hydrogen in a light, compact form, can be re-fuelled rapidly, and is affordable, safe and easy to produce in large quantities. Hydrogen can be stored as (i) Pressurized gas (ii) cryogenic liquid (iii) solid fuel as chemical or physical combination with material such as metal hydride, complex hydride and carbon material [10-11]. The hydrogen atom binds easily with the Mg atoms i.e., enthalpy of formation of the metal hydride is too large, so that the hydride needs to be heated to very high temperature and to release hydrogen gas at high enough pressure. In order to improve the kinetics metal hydrides are mixed with chemical elements like Nickel and Niobium [12]. Metals differ in the ability to dissociate hydrogen, this ability being depended on surface structure morphology and purity. The mechanical alloying can be used to blend these metals together then it forms nano-composite structure. The nano material has significant features such as absorption on the surface and inter-intra grain boundaries [13]. This property creates major influence on the thermodynamics and kinetics of hydrogen absorption by increasing diffusion rate [14-15]. However, the practical measurement of hydrogen uptake and release, particularly for storage applications can be technically demanding mainly due to the physical properties of hydrogen required for the same. Elemental powders were mechanically alloyed and subsequently electrochemical studies were done in order to evaluate the hydrogen uptake-release behavior of the electrode material (nano and amorphous scale particles) [16].

2. Experimental part

Elemental powders of magnesium, nickel and niobium with a particle size distribution of ~100-150 μm and to purity of 99.9% was mechanically alloyed using planetary ball mill (Insmart systems, Hyderabad, India). The niobium based alloy with different particle size was prepared by mechanical alloying in an argon atmosphere. The crystallinity

and phase evolution of the samples were analysed by X-ray diffractometer (Rigaguultima III X ray at a scan rate of 0.02˚ per 3s using Cu-Kα radiation (λ=1.5418 A˚). Wet alloying was done using a stainless steel container. The ball to powder ratio was 10:1. The milling duration was 30 and 50 hours using planetary ball mill with milling speed 260 rpm. The particle morphology and presence of various elements were observed by ZEISS SUPRATAM 50 VP scanning electron microscope (SEM) equipped with an energy dispersive spectrometer (EDS). The activation energy was measured by Simultaneous Thermal Analyzer (Perkin Elmer STA6000). Kissinger analysis was used to calculate the activation energy of metal hydrides at varying heating rates namely 4, 6, 8 and 10°C/min. The heating was performed in an argon atmosphere. Electrochemical studies were done using a three electrode cell set up. The test was performed using potentiostat/ galvanostat unit (SP150 Biologic) at room temperature. The working electrode of hydrogen absorbing alloys were compacted at 20 MPa by mixing 0.3g alloy powder with 0.7g nickel powder and then cold pressed to pellets of 10mm diameter. NiOOH/ Ni(OH)$_2$ was used as counter electrode and Hg/ HgO as reference electrode in 6M KOH electrolyte solution. The charge/discharge behaviour of alloy with various milling hours was carried out between the potential limits of –0.8 and – 1.1 V at the current density of 20mAg^{-1}. EIS measurement was carried out using potentiostat/ galvanostat at a frequency of 1MHz-100 mHz with sinusoidal amplitude of 10mV.

3. Structural analysis

Fig. 1 shows the x-ray pattern of 30 and 50 hours milled Mg$_{67}$Ni$_{32}$Nb$_1$ alloy powder. 30 hours (nanocrystalline) milled powders with higher volume fraction of Mg$_2$Ni provides higher discharge capacity when compared with 50 hours milled powders (amorphous) with increasing NbO$_2$ content. Higher the oxide content in the alloy powders higher will be the barrier for electron-ion transport since the individual powder particles will

be coated with an oxide layer which restricts the chemical kinetics from thereon. After 30 hours milling reflections from Mg$_2$Ni phase broadens wherein decrease in crystallite size (40nm) was observed. After 50 hours milling crystallite size of 90nm with a noisy pattern of long range order was observed [17-18].
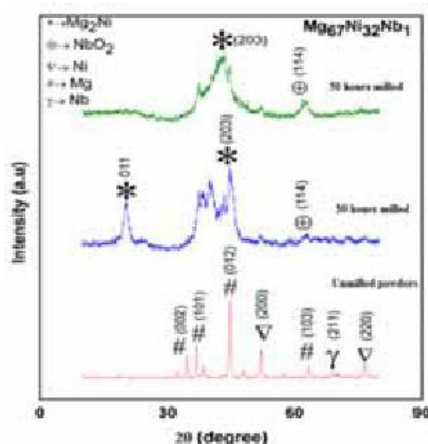
Fig. 1 XRD patterns of Mg$_{67}$Ni$_{32}$Nb$_1$ alloy with different structure

SEM images of 30 and 50 hours are shown in Fig. 2. Initial particle size distribution was in the range of 25μm wherein after 30 hours milling particles of 1-5 μm are obtained. Subsequently, after 50hours milling smaller particles merge together to form conglomerates leading to a spongy morphology. The EDS results confirm the presence of magnesium, nickel and niobium compound.
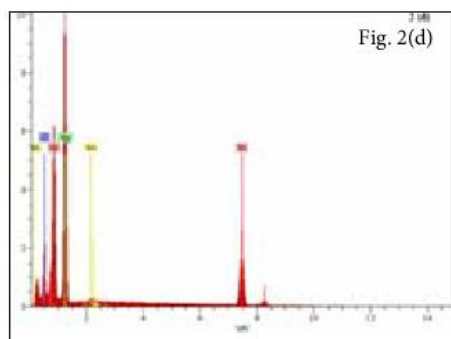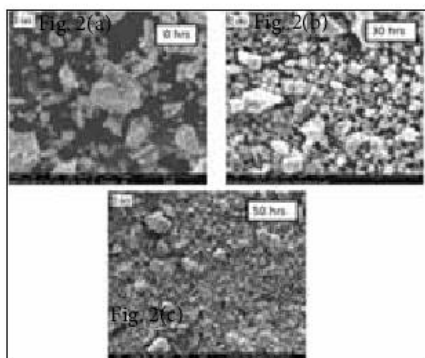
Fig. 2 (a) SEM image of premixed Mg$_{67}$Ni$_{32}$Nb$_1$ powder (b) SEM image of 30 hours milled Mg$_{67}$Ni$_{32}$Nb$_1$ alloy powder (c) SEM image of 50 hours milled Mg$_{67}$Ni$_{32}$Nb$_1$ alloy powder (d) EDS analysis of Mg$_{67}$Ni$_{32}$Nb$_1$ alloy powder

4. DSC analysis

The DSC results of 30 hours and 50 hours milled powders are shown in Fig. 3-4. Considerable shift in the peak temperature was observed with increasing heating rate for both 30 hours (nano) and 50 hours (amorphous) milled powders. Major reason behind peak shift is the increased milling hours. In addition, shift in the peak temperature can be seen as a shift in the point where maximum rate of the chemical reaction takes place [19]. Fig. 5 shows that, change in enthalpy of 30 hours milled powders (nano powder particles) was found to be relatively high when compared to the 50 hours milled powder (amorphous powder). Thus nano powders exhibit better electrochemical properties when compared to amorphous powders.
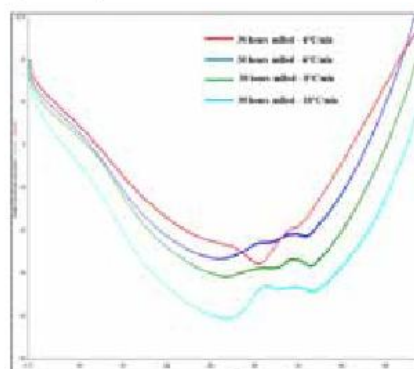
Fig. 3 DSC curves of 30 hours milled powders at various heating rate
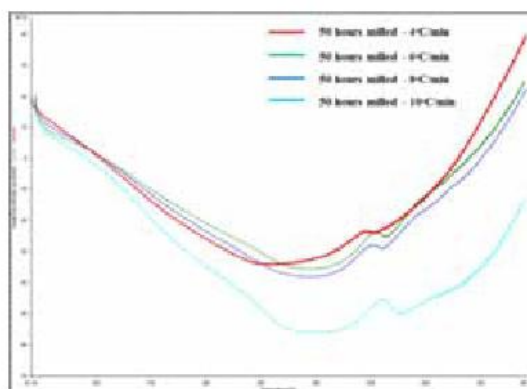
Fig. 4 DSC curves of 50 hours milled powder at various heating rates

Figs. 5-8 show the strong dependence of particle size in deciding the chemical kinetics of the metal hydride systems [20]. In case of nano particles change in system enthalpy was relatively high, presumably due to 30 hours milled powder particles sharing a larger surface area as compared to amorphous (50 hours) powder particles.
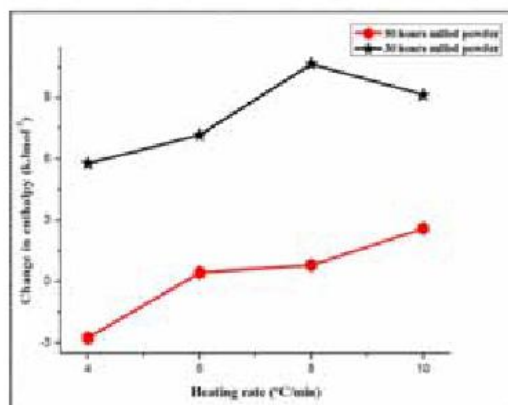
Fig. 5 Effect of particle size (ball milling time) and heating rate on change in system enthalpy

Peak temperature is a point in the DSC curve where the maximum rate of the chemical reaction is expected to happen. Considerable amount of peak shift was observed in 50 hours milled powder when compared to 30 hours milled powder possibly due to increased milling hours. This indicates the relative

thermal stability of nano particles when heating rate was increased. Also it is evident from figure 6 that the developed nano metal hydrides (30 hours milled powder) exhibited a steady state chemical kinetics when compared to amorphous powders (50 hours milled powders) [21].
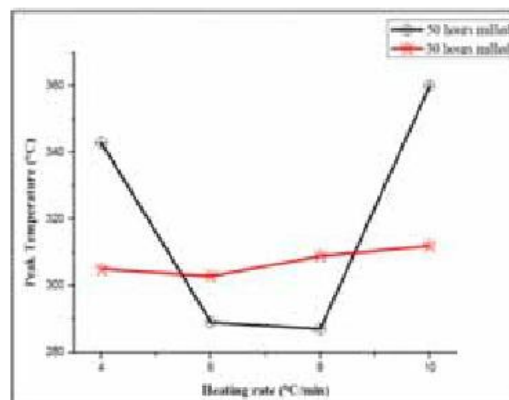
Fig. 6 Effect of heating rate and ball milling time on peak temperature

Fig. 7 shows that nano particles (30 hours milled powder) advanced in onset temperature pertaining to the chemical reaction with increase in heating rate, and, also, that 30 hours milled nano particles showed much better chemical kinetics by advancing the chemical reaction when compared to 50 hours milled powders.
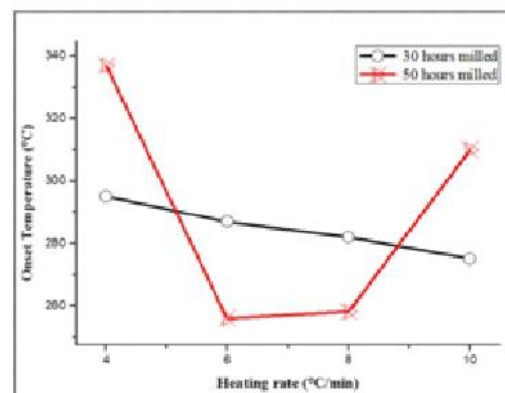
Fig. 7 Effect of ball milling time and heating rate on the shift of onset temperature
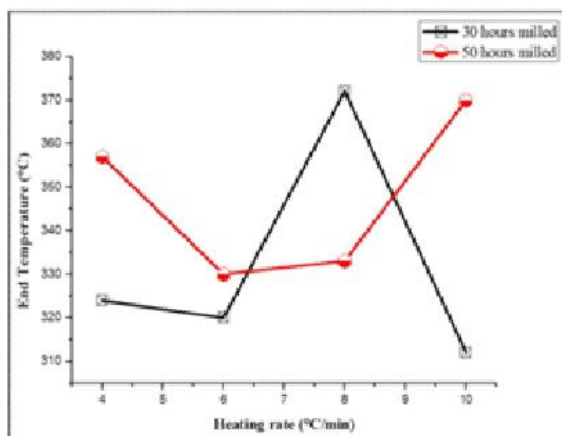
*Fig. 8 Effect of heating rate and ball milling time
on the shift of end temperature*

Fig. 8 reveals the relation between peak temperature and particle size. In case of 30 hours milled powder the peak temperature increased with increasing heating rate, while a huge variation with respect to peak temperature was observed for 50 hours milled powder. Hence, the nano particles (30 hours milled powder) are comparatively thermally stable with increase in peak temperature when compared to the amorphous powders (50 hours milled powder). At the same time, from Fig. 8 the end (chemical reaction) temperature of 30 hours milled powder under varying heating rate predominantly showed a delaying response when compared to amorphous powders, which is an expected behaviour from a hydrogen storage material.

Fig. 9 shows the Kissinger analysis of 30 hours and 50 hours milled powders. It is very much evident that 30 hours milled powder (nano powder particles) revealed very high activation energy when compared to 50 hours milled powder (amorphous powder). Consequently, the powders with higher activation energy will yield a better electrochemical behaviour when compared to the amorphous powders. Since 30 hours milled powder has more activation energy compared to 50 hours milled powder, the later can easily overcome the barrier that prevents the same to transport ions during the electrochemical studies

[22]. Or in other words the 30 hours milled powder has molecules with sufficient activation energy to overcome the barrier that prevents the chemical reaction.
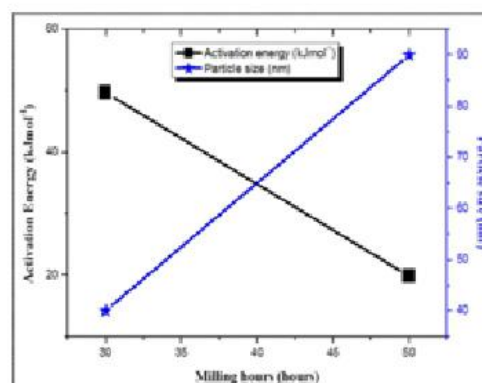
*Fig. 9 Kissinger analysis depicting the effect of
particle size on E$_a$ of the developed Mg$_{67}$Ni$_{32}$Nb$_1$*

5. Electrochemical analysis

5.1 Impedance analysis

Fig.10 shows the Nyquist plot of nanostructured Mg$_{67}$Ni$_{32}$Nb$_1$ alloy. 30hours milled nanostructured Mg$_2$Ni powders exhibit a small semicircle, lower Rct and higher capacitance value when compared to 50 hours milled powders, which may be due to high electrode surface area. The values are shown in Table 1. This result indicates lower resistance to charge transfer and more efficient diffusion of electrons. Hence nanostructure has high hydrogen absorption capacity [22-23].

*Fig. 10 Nyquist plot of Mg$_{67}$Ni$_{32}$Nb$_1$alloy with
different structure*

Structure	R$_s$(Ω/g)	R$_{ct}$(Ω/g)	C$_{dl}$ (μF)	Dx10^{10} (cm^{2}s^{-1})
Nano	0.11	1.11	10.62	9.7
Amorphous	0.08	1.70	6.99	1.12

Table. 1 Impedance analysis of Mg$_{67}$Ni$_{32}$Nb$_1$ compacts

5.2 Discharge capacity analysis

Fig. 11 describes the charge-discharge behaviour of Mg$_{67}$Ni$_{32}$Nb$_1$ alloy carried out between the potential limits of –0.8 and –1.1V at a current density of 20 mAg-1 using 6 M KOH solutions. In the first cycle, the discharge capacity of 30hrs and 50hrs are 388 and 327 mAhg-1 respectively. The maximum discharge capacity occurred in first cycle then it decreased as the number of cycle increased. The nano structured powder particles exhibited good discharge capacity and capacity retention characteristics when compared to agglomerated nano structured powders (50hrs). This is mainly due to small particle size, since the particle size reduction leads to increased interaction between powder particle and electrolytic solution. Further, smaller particles have a larger surface area which enhances the hydrogen interaction into host structure thereby resulting in high ionic current. The discharge capacity versus cycle number is shown in figure 12. The discharge capacity of nano and amorphous structure after 10 cycles are 328, 259 mAhg-1 and their corresponding capacity retentions were 84, 79% respectively.
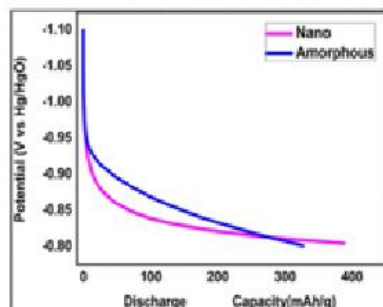
Fig. 11 Potential vs Discharge Capacity of Mg$_{67}$Ni$_{32}$Nb$_1$ alloy
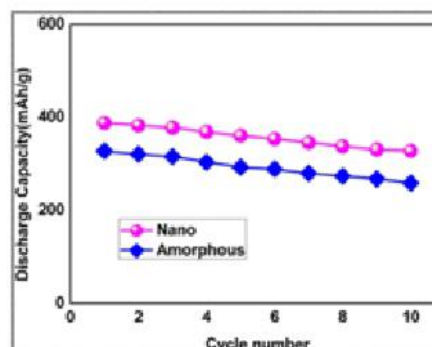
Fig. 12 Discharge Capacity Versus Cycle number of Mg$_{67}$Ni$_{32}$Nb$_1$ alloy

6. Conclusion

The two different size of Mg$_{67}$Ni$_{32}$Nb$_1$ particle were synthesized by mechanical alloying. The X-ray diffraction pattern showed that 30 hours milled nano structured metal hydride reveals a greater volume fraction of Mg$_2$Ni intermetallic compounds leading to an increased discharge capacity of the electrode material. The particle size had a great effect on the electrochemical properties of Mg$_{67}$Ni$_{32}$Nb$_1$ alloy. The electrode composed of 40 nm showed the best discharge capacity and good cyclic stability than others. SEM images confirmed the uniform distribution of nano particles whereas the EDS analysis confirmed the presence of Magnesium, Nickel, and Niobium and also few traces of oxide. It is found that the small particle with larger surface area provided more hydrogen ions for diffusion there by resulting high ionic current and discharge capacity. DSC analysis revealed a relatively high enthalpy for 30 hours milled powder which ensured high chemical kinetics, better thermal stability, advancement of onset and postponement of end temperature. Aforesaid DSC results of 30 hours milled powder promises better charge-discharge behaviour when compared to 50 hours milled powders. The Nyquist plot also expressed that the electrons and hydrogen ions can transfer more actively in nanostructure than in amorphous structure.

References

1. BillurSakintuna, Farida Lamari- Darkrim and Michael Hirscher, "Metal hydride materials for solid hydrogen storage: A review", Int J Hydrogen Energy Vol. 32, 1121-1140 (2007).

2. Fushen Yang, Xinxin Cao, Zaoxiao Zhang, ZeweiBao, Zhen Wu, NyallangNyamsi and Serge J, "Assessment on the long term performance of a LaNi5 based hydrogen storage system" Energy procedia Vol. 29, 720-730 (2012).

3. J.M. Ogden, "Developing an infrastructure for hydrogen vehicles: a southern California case study", Int J Hydrogen energy Vol. 24(8), 709-730 (1999).

4. Hydrogen storage tank systems and materials selection for transport applications ASME Dogan B,confpvp 2006-ICPVT-11, van couver, Canada, july pp 23-27, (2006) conference proceeding CD, "Track materials and fabrication session materials for hydrogen service" paper no.93868 1-8.

5. Hannes Jonsson, SveinnOlafsson, Jon Tomas Guomundsson, BragiArnason, FjolaJonsdottir and HjalmtyrHafsteinsson, "Light metal alloy for hydrogen storage" www.hi.is/~hj/HstorageBrief.pdf

6. E. David, "An overview of advanced materials for hydrogen storage" J Mater Process Technol; Vol.162-163, 169-77 (2005).

7. J. Yang, A. Sudik, C. Wolverton, DJ. Siegel, "High capacity hydrogen storage materials: attributes for automotive applications and techniques for materials discovery", Chemical Society Reviews Vol. 39, 656–675 (2010).

8. E. G. Baburaj, F. H. Froes, V. Shutthanandan, and S. Thevuthasan, "Low cost synthesis of nanocrystalline titanium aluminides," " Interfacial Chemistry and Engineering Annual Report, Pacific Northwest National Laboratory, Oak Ridge, Tenn, USA, 2000.

9. R. Schulz, S. Boily, L. Zaluski, A. Zaluka, P. Tessier, and J. O. Str¨om-Olsen, "Nanocrystalline materials for hydrogen storage," Innovation in Metallic Materials, 529–535, 1995.

10. Michael U.Niemann, Sesha S. Srinivasan, Ayala R. Phani, Ashok Kumar, D. Yogi Goswami, and Elias K. Stefanakos, "Nanomaterials for Hydrogen Storage Applications": A Review Journal of Nanomaterials, Hindawi Publishing Corporation Vol. 2008, Article 9 pages, doi:10.1155/2008/950967

11. B. Árnason, T. I. Sigfússon and V. K. Jónsson,"New Concepts in Hydrogen Production in Iceland", Int. J. Hydrogen Energy, Vol. 18, 915. (1993)

12. B. Árnason and T. I. Sigfússon, "Iceland - A Future Hydrogen Economy", Int. J. Hydrogen Energy, Vol. 25, 389 (2000).

13. The Metal-Hydrogen System - Basic Bulk Properties, Y. Fukai, (Springer-Verlag, Berlin, (1993).

14. R.Griessen and T. Riesterer, in "Hydrogen in Intermetallic Compounds", By L. Schlapbach, Topics Appl. Phys., Vol63, 219 Springer, Berlin, (1988).

15. H. Buchener and R. Povel "The Daimler-Benz Hydride Vehicle Project", Int. J. Hydrogen Energy, Vol.7, 259 (1982).

16. BorislavBogdanovic, Klaus Bohmhammel, Babett Christ , Alexander Reiser, Klaus Schlichte, Ralph Vehlen and Ulrich Wolf "Thermodynamic investigation of the magnesium–hydrogen system" Journal of Alloys and Compounds Vol. 282, 84–92 (1999).

17. X. Li, D.F. Foster and D.J. Cole-Hamilton, Polym. AdvTechnol. Vol.5, 541 (1994).

18. T.S. Fischer, A. Pfeil, N. Eisenreich, A.C. Jones, A.B. Leese, S. Rushworth and G. Williams, Proceedings of the 26th International Annual Conference of ICT, 85/1±85/6 (1995).

19. S. Duffy, P.F. Nolan, S. Rushworth, A.B. Leese and A.C. Jones, Adv. Mater. Opt. Electron Vol. 7, 233 (1997).

20. A.C. Jones, A.K. Holiday and D.J. Cole-Hamilton, J. Cryst. Growth Vol 68, 1 (1984)

21. A.C. Jones, J. Crystal Growth Vol. 129, 728 (1993).

22. N. Kuriyama, T, Sakai, H. Miyamura, I. Uehara, H. Ishikawa and T. Iwasaki, "J. Alloys Comp" Vol. 202, 183-197 (1993).

23. S. G. Real, M. G. Ortiz, E. B. Castro and A. Visitin, Int. J. Hydrogen Energy Vol. 33, 3493-3495 (2008).

SILVER NANOPARTICLE INCORPORATED POROUS NANO-STRUCTURED TITANIA LAYER ON Ti METAL : A CANDIDATE FOR ORTHOPEDIC IMPLANT

Archana Rajendran, Deepak K. Pattanayak

CSIR-Central Electrochemical Research Institute, Karaikudi, India

Abstract: *A surface modification approach to enhance the bioactivity and antibacterial property of Ti metal is reported. Ti metal when subjected to H_2O_2 solution treatment forms a porous nano-structured hydrated titania layer on its surface. Silver nanoparticles were subsequently incorporated into this porous nano-structured hydrated titania layer by treating in $AgNO_3$ solution. Ti metal subjected to H_2O_2-$AgNO_3$ treatment when heat treated formed the nano-structured titania network with well distributed silver nano-particles. Results showed that thus formed surface improves the bioactivity of Ti metal by forming an apatite layer in simulated body fluid and incorporated silver nanoparticles showed antibacterial activity to pathogenic bacteria. Results showed that Ti metal with nano-structured titania layer incorporated with silver nanoparticles can be considered as a candidate for various orthopedic implants.*

Keywords: *Ti metal, silver nanoparticles, titania, in vitro bioactivity, antibacterial study.*

Introduction:

Metallic materials such as stainless steel, Co-Cr-Mo, titanium (Ti) and Ti alloys are widely used in orthopedic and dental field [1]. The bulk properties of these metallic biomaterials, such as non-toxicity, corrosion resistance or controlled degradability, modulus of elasticity, and fatigue strength are recognized to be highly relevant in terms of the selection of the right biomaterials for a specific biomedical application. This is due to the interactions between the biological environment and artificial material surfaces, onset of biological reactions, as well as the particular response paths chosen by the body. Thus material surface plays an extremely important role in the response of the biological environment to the artificial medical devices [2].

Artificial implants made of titanium, during the manufacturing stage usually form an oxide surface layer. Such "native" surfaces either do not bond to living bone or take long time and hence, their fixation in living body is not stable for a long period. In order to improve the bonding ability of bone to implant, various surface modification approaches are adopted. Among them various bioactive calcium phosphate coating on metal surface are developed that can accelerate the bone integration. Apart from calcium phosphate coatings, various chemical treatment methods are also proposed in the literature that forms a strong direct contact between implant and living bone. Another important reason for surface modification to titanium medical devices is that specific surface properties that are different from those in the bulk are often required. For example, in order to accomplish biological integration, it is necessary to have good bone formability. The proper surface modification techniques not only retain the excellent bulk attributes of titanium and its alloys, such as relatively low modulus, good fatigue strength, formability and machinability, but also improve specific surface properties required by different clinical applications [3].

Apart from surface integration, implant associated infections due to various pathogenic bacteria are also of serious concern if proper care is not taken during the pre and post implantation period [4]. These infections might lead to implant failure and necessitates second time surgery. Some reports suggest that the presence of a foreign body reaction

in the form of sutures resulted in a dramatic reduction of the minimum inoculum required to produce pus [5].

It has been reported that the ability of bacteria to adhere to materials and to promote formation of a biofilm is the most important feature of their pathogenicity. The host defense mechanisms often seem to be unable to handle the infection and, in particular, to eliminate the microorganisms from the infected device. Since antibacterial chemotherapy is also frequently not able to cure these infections, it is important to search an alternate way to reduce bacterial infection. Among the various solutions, one concept for the prevention of bacterial infection involves the impregnation of devices with various substances such as antibacterials, antiseptics and/or metals, which needs further studies to translate the knowledge on the mechanisms of biofilm formation into applicable therapeutic and preventive strategies [6].

Antibiotic-loaded biomaterials are currently as a part of standard medical procedures for both local treatment and prevention of implant infections. Results indicated that systems designed for prolonged release of prophylactic inhibitory or sub inhibitory amounts of antibiotics, in absence of strict harmonized guidelines, raise concerns for their still weakly proved efficacy but, even more, for their possible contribution to enhancing biofilm formation and selecting resistant mutants.

Valentin reported that vancomycin covalently attached to a Ti alloy surface (Vanc-Ti) could prevent bacterial colonization [7]. The study examined the effect of this Vanc-Ti surface on Staphylococci epidermidis, a Gram-positive organism prevalent in orthopedic infections. The results indicated that antibiotic derivatization of implants can result in a surface that can resist bacterial colonization. This technology holds great promise for the prevention and treatment of periprosthetic infections [7-8].

Apart from antibiotics, silver is a well know antibacterial agent and is highly toxic to microorganisms. Thus silver ions, as an antibacterial component, have been used in the formulation of dental resin composites. Also silver nanoparticle-modified titanium (Ti-nAg) surface using silanization method and there by suggested that silver nanoparticle-modified titanium is a promising material with an antibacterial property that may be used as an implantable biomaterial [9].

This paper reports an attempt to synthesize bioactive Ti metal that can show antibacterial effect so that it can be useful in both orthopedic and dental field. We considered silver as an external antibacterial agent and developed novel methodology to separately incorporate the silver ions into titanium metal. Materials were subsequently characterized using various sophisticated characterization tools to cater the specific functions for their suitable applications as bio implants. These surface modification method is applied to porous Ti metal prepared by powder metallurgy route and both antibacterial and bioactivity are studied.

Materials and methods:

Commercially available pure titanium sheet (Grade 2) were cut in to 10 x 10 x 1mm^3 dimensions and abraded with # 400 grade SiC paper. Polished samples were ultrasonically cleaned with acetone, 2-proponol and ultrapure water for 15 min each and dried for overnight in an oven at 40°C. The cleaned samples were soaked in 10 mL of 30% H_2O_2 solution in centrifuge tubes and kept at 70°C for 3h with shaking at a speed of 120 rpm in a water bath. Then these samples were gently washed with ultrapure water and soaked in 0.05-100 mM $AgNO_3$ solution at 40°C, 120 rpm for 3h in water bath and finally washed with ultrapure water and dried. Some samples were heat treated at 600°C for 1h in a muffle furnace using air atmosphere. Fig. 1 shows the detail experimental procedure followed in the present study.

Fig 1: Schematic representation of various chemical and heat treatment followed in the present study.

For TEM observation, Ti grids were directly used after treatment with H_2O_2 solution and 100mM $AgNO_3$ solution in the same method as described above.

The specimens subjected to the H_2O_2 and 100mM $AgNO_3$ solution and heat treatment were soaked in 30 mL of an acellular simulated body fluid (SBF) with ion concentrations nearly equal to those of human blood plasma at 36.5°C [10]. The SBF was prepared by dissolving reagent-grade NaCl, $NaHCO_3$, KCl, $K_2HPO_4.3H_2O$, $MgCl_2.6H_2O$, $CaCl_2$ and Na_2SO_4 (Sigma Aldrich) into ultra pure water, and buffered at pH 7.4 with tris-hydroxymethylaminomethane $((CH_2OH)_3CNH_2)$ and 1M HCl (Fluka). Table-1 shows the ion concentration of human blood plasma and SBF. The specimens were removed from SBF after specified time period, and then the surface of the chemically treated Ti metal is characterised.

Table 1: Ion concentrations of human blood plasma and SBF

	Concentration / mM							
	Na⁺	K⁺	Mg²⁺	Ca²⁺	Cl⁻	HCO₃⁻	HPO₄²⁻	SO₄²⁻
Blood plasma	142.0	5.0	1.5	2.5	103.8	27.0	1.0	0.5
SBF	142.0	5.0	1.5	2.5	147.8	4.2	1.0	0.5

Table 2: Template for Final Placement of any Part for Storage

Standard disk diffusion method was used to evaluate the antimicrobial properties of untreated and Ti metal treated with H_2O_2, H_2O_2-$AgNO_3$ solution. For anti microbial activity study, 200 mL of nutrient medium was prepared with sterile distilled water in a conical flask and then autoclaved at 121°C for 15min. Then at the hand bearable heat the sterilized nutrient medium was poured aseptically into the sterile petri plates and allowed to solidify. After solidification, the plates were kept in an inverted position to avoid the formation of water droplets inside the plates. Lyophilized cells of Staphylococcus aureus were collected from Microbial Type Culture Collection and Gene Bank (MTCC), Dept. of Biotechnology, Chandigarh, India. The vials were cut open and the lyophilized cells were aseptically transferred into the nutrient broth (0.5 % NaCl, 0.15 % yeast extract, 0.15 % beaf extract, 0.5 % peptone) at room temperature for about 24 h. The overnight culture of Staphylococcus aureus were taken and the

cells were swabed on the nutrient agar plates using sterile cotton swab under sterile condition to avoid the over growth of cells and contamination. All the treated Ti metal plates were aseptically placed on the inoculated plates using a sterile forceps and allowed it for 24 h of incubation.

The surfaces of the Ti metals subjected to various chemical treatments described above were observed using scanning electron microscope (TESCAN, Czech Republic). The chemical composition of surfaces of chemically treated Ti metals were analysed by energy dispersive X-ray analysis attached to the SEM under an acceleration voltage of 15kV. This analysis was carried out in two different location of each sample and averaged to know the amount of silver ions incorporated into the Ti metal.

In order to identify the surface functionalisation, laser Raman spectroscopy (RENISHAW Co., UK) was used for untreated and Ti metal subjected H_2O_2, H_2O_2-100Ag and heat treatment. For this measurement He-Ne Laser with a wavelength of 630 nm was used. Morphology of Ti metal subjected to H_2O_2 and H_2O_2-$AgNO_3$ and heat treatment were observed under transmission electron microscope (TEM; Tecnai 20 G2 FEI, The Netherland). The specimen for TEM observation was prepared by directly taking Ti TEM grids and then subjected to chemical treatments. SAED pattern were also taken for each conditions. Silver released in SBF was measured by AAS (Varian co., Australia) and surface topography was observed by SPM (Molecular Imaging, USA).

Results and discussions:

Fig. 2 shows the SEM images of Ti metal as-polished and subjected to H_2O_2 treatment. It can be seen from Fig. 2 that as-polished Ti metal has very smooth surface. The scratches observed on the surface of Ti metal are formed during the course of polishing. It is well known that Ti metal is highly reactive and can form a very thin oxide layer (TiO_2) of 4-10 nm in thickness when exposed to air. This oxide layer is removed by the subsequent polishing.

Compared to as-polished image [Fig. 1(a)], fine network structures are clearly observed on the surface of Ti metal, when the Ti metal is treated with H_2O_2 solution [Fig. 1(b)]. Results showed that these fine network structures are entirely covered on the surface of Ti metal.
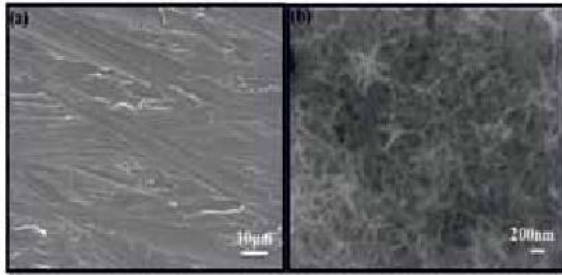

Fig. 2: SEM images of Ti metal (a) as-polished and (b) subjected to H_2O_2 treatment.

This indicates that the network structures of hydrogen titanate formed on the surface of Ti metal is due to the chemical reaction between Ti metal and H_2O_2 solution at an elevated temperature of 70ºC [3,11]. Thickness of porous network structure can be controlled by treatment duration and temperature. These hydrated titanate layer formed by H_2O_2 treatment, respectively is expected to replace Ag ions with the H+ ions by the subsequent $AgNO_3$ solution. Fig. 3 shows the SEM image of Ti metal treated with H_2O_2-100mM $AgNO_3$ and then subjected to heat treatment at 600ºC for 1 h. Results showed that these fine network structure formed by H_2O_2 treatment did not change even after subsequent $AgNO_3$ as well as heat treatment.
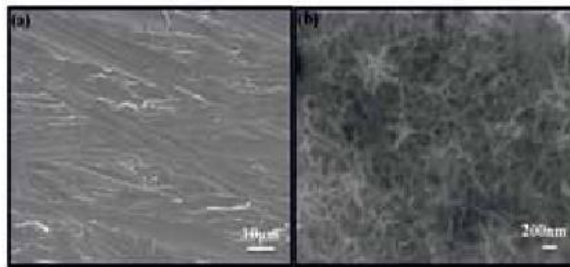
Fig. 3: SEM images of Ti metal treated with (a) H_2O_2-100$AgNO_3$ and (b) H_2O_2-100$AgNO_3$, heat treated at 600ºC.

EDX measurement results presented elsewhere showed that about 3-3.5 at % of Ag ions could be incorporated by the H_2O_2-100mM $AgNO_3$ solution treatment [12]. The amount of Ag ions could be controlled by the amount of $AgNO_3$ concentrations. This indicates that large amount of Ag ions could be incorporated by H_2O_2 treatment possibly due to the formation of surface hydrated layer. However, it is interesting to observe the effect Ag incorporation on antibacterial property and the result will be presented in latter section.

Atomic Force Microscopy study was carried out to identify the surface morphology and roughness of the surface modified titanium samples [13]. Fig. 4 shows the AFM images of untreated Ti metal (as-polished) and Ti metal subsequently treated with H_2O_2 and 100mM $AgNO_3$ solution. We can see that as-polished Ti metal surface is more smooth and about 100-200 nm roughened surface. However, after H_2O_2 treatment roughness increased to about 1μm. Comparing the 3D images, we can see that entire surface of Ti metal appeared to be uniformly etched (small hills) by the H_2O_2 treatment. However, subsequent $AgNO_3$ treatment again transformed the surface to smoother. This is possibly due to the Ag ion incorporation into Ti metal by the chemical treatment. This result indicates that the chemical treatment increased the surface area of the Ti metal by uniform etching. Such an etched surface is expected to improve the anchoring between the implant and the newly formed bone when implanted in the human body and, thus resulted implant can be easily interlocked to avoid the loosening after implantation.

Figure 4: AFM images of (a) as-polished Ti metal (b) treated with H_2O_2 and (c) H_2O_2-100$AgNO_3$ solution.

Fig. 5 shows the TEM image and corresponding SAED pattern of Ti metal subjected to H_2O_2 and subsequently treated with $AgNO_3$ solution, respectively. From Fig. 5 it was seen that the fine network structure observed in SEM appeared to be sheet like morphology. This sheet like nano structures of width 50-100 nm and 50-200 nm in length formed by the chemical reaction between Ti metal and H_2O_2 solutions and the grown layer can be controlled by controlling the treatment durations and temperatures. Ti metal when treated with H_2O_2 formed an amorphous phase as indicated in the SAED pattern. On subsequent treatment with 100mM $AgNO_3$ solution, silver nano particles of morphology 5-10nm in diameter well distributed on the fine network structures were seen and these remained stable even after heat treatment [12].
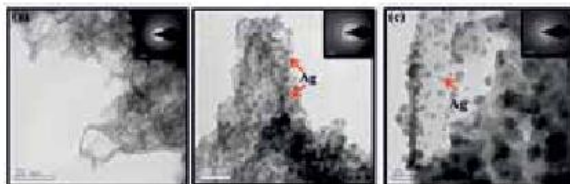
Fig. 5: TEM images of Ti metal treated with (a) H_2O_2 (b) H_2O_2-100AgNO$_3$ and (c) H_2O_2-100AgNO$_3$ and heat treatment.

Fig. 6 shows the SEM images of Ti metal treated with H_2O_2 and 100AgNO$_3$ heat and soaked in SBF for 7 days. Results showed that Ti metal did not form apatite when soaked in SBF. However after chemical and thermal treatment surface is covered with spherical particles. These spherical particles are assigned to bone like apatite. EDX analysis results further confirmed these spherical particles to be calcium and phosphate (apatite).
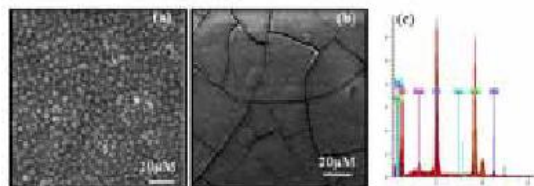
Fig. 6: SEM images of Ti metal treated with (a) H_2O_2 (b) H_2O_2-100AgNO$_3$ and heat treatment and soaked in SBF for 7 days and (c) corresponding EDX pattern.

Anti bacterial activity of surface modified titanium metals was studied by the method of inhibition zone. Fig. 7 shows the antibacterial study of the surface modified Titanium samples against Staphylococcus aureus. The results show that the pure titanium and H_2O_2 treated samples had no antibacterial activities against the S. aureus. Silver treated sample shows clear bacterial inhibition zone. The average inhibition Zone against the S. aureus for the samples is 0.6 cm.
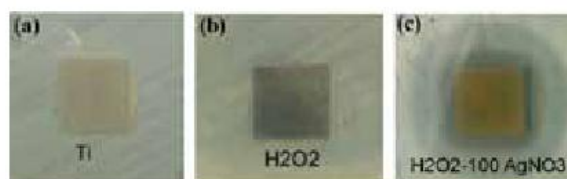
Fig. 7: Antibacterial study of Ti metal (a) as-polished (b) treated with H_2O_2 and (c) H_2O_2-100 AgNO$_3$ treatment

From the zone of inhibition against S.aureus confirmed that the silver ions from the titanium surface are able to kill the bacteria and thereby prevent the bacterial colonization. The silver incorporated on the hydrogen titanate network surface diffuses out when it come in contact with any fluid. This diffused silver ions will act on the surrounding bacterial cells and destroy the cell membrane of bacteria and thus inhibits bacterial growth.The exact mechanism how the silver acts on the bacterial membrane is still unknown. A lots of assumptions were proposed on the mechanism of action of silver ions on bacterial [14-16]. Some reported that the silver will unspecifically bind on the cell membrane and enter into the bacterial cytoplasm. Inside the cell it binds to the thiol group of enzymes, inactivate them and finally leads to cell death [17]. The silver can also interact with DNA to enhance pyrimidine dimerization and possibly prevent the DNA replication [18].

Therefore, this attempt to give antibacterial property to the Titanium implant is accomplished with this agar plate zone formation study. Eventhough 100 mM Ag treated Ti shows antibacterial effect with clear zone of inhibition, the minimum amount of

silver is only accepted to the human body. Higher concentrations can cause cytotoxicity. 10mg/l is the acceptable limit of silver concentration to the human body [19].

Ti metal treated with H_2O_2 forms hydrated titania gel layer that accelerate the calcium phosphate or apatite deposition on its surface. However, H_2O_2 treatment did not show any antibacterial activity as seen in Fig. 7. This might cause infection during implantation if proper care is not taken by the surgeons during the time of surgery. Therefore, it is essential if antimicrobial agent can be incorporated to the medical devices. Silver nano particles incorporated Ti metal prepared in the present study clearly showed the zone formation in Staphylococcus aureus. These silver ions are gradually released as reported earlier observed from the AAS result as measured in SBF solution [12]. Thus released silver ions are expected to kill the bacteria present in the implantation site. Further studies is in progress to optimise the silver concentration without any cell cytotoxity and the detail result will be published elsewhere. Thus the doping of titanium surface with silver provides an antibacterial activity to the metal, so that it can be applied as a bone implant in the biomedical field. The titanium surface pre treated with H_2O_2 can give excellent bioactivity (20-23) and also it will induce antibacterial activity after doping of silver to the titanium surface. Silver ions could be encapsulated in the network structure formed on the titanium surface as a result of H_2O_2 pre treatment. The amount of silver ions released from the surface modified titanium is significant for preventing bacterial colonization and thereby bacterial infection.

Liao et. al. prepared a silver nanoparticle-modified titanium (Ti-nAg) surface using silanization method and proved that about 4.6% silver present on the Ti surface was able to inhibit the activity of 94% of S.aureus and 95% of E.coli [9]. However, the amount of incorporated Ag to cell cytotoxicity was not studied.

Summary

Silver nanoparticles were successfully incorporated into the hydrogen peroxide pre-treated titanium surface by simple chemical treatment method. The incorporated silver nanoparticles were able to induce the bioactivity of titanium while comparing to the only hydrogen peroxide treated samples, which is studied by soaking the surface modified samples in simulated body fluid. The antibacterial property of thus developed titanium sample is proved against Staphylococcus aureus.

References

1. Douglas C. Hansen, The Electrochemical Society Interface, (2008).

2. James M Anderson, Biological responses to materials, Annu. Rev. Mater. Res. 31, 81-110, (2001).

3. Xuanyong Liu, Paul K. Chu, Chuanxian Ding, Surface modification of titanium, titanium alloys and related materials for biomedical applications, Mat. Sci. & Engg. R, 47, 49–121, (2004).

4. Rabih O. Darouiche, Gregory Green and Mohammad D Mansouri, Antimicrobial activity of antiseptic-coated orthopaedic devices, Int. J. Antimicrobial Agents, 10(1), 83-86, (1998).

5. S. D. Elek and P. E. Conen, Br. J. Exp. Pathol., 38(6), 573–586, (1957).

6. Christof von Eiff, Bernd Jansen, Wolfgang Kohnen and Karsten Becker, Infections associated with medical devices, pathogenesis, management and prophylaxis, Drugs, 65(2), 179-214, (2005).

7. Valentin Antoci, Jr., Christopher S. Adams, Javad Parvizi, Helen M. Davidson, Russell J.

Composto, Theresa A. Freeman, Eric Wickstrom, Paul Ducheyne, Donald Jungkind, Irving M. Shapiro and Noreen J. Hickok, The inhibition of Staphylococcus epidermidis biofilm formation by vancomycin-modified titanium alloy and implications for the treatment of periprosthetic infection, Biomaterials, 29(35), 4684-4690, (2008).

8. Carla Renata Arciola, Davide Campoccia, Pietro Speziale, Lucio Montanaro, John William Costerton, Biofilm formation in staphylococcus implant infections - a review of molecular mechanisms and implications for biofilm-resistant materials, Biomaterials, 33(26), 5967-5982, (2012).

9. Liao Juan, Zhu Zhimin, Mo Anchun, Li Lei and Zhang Jingchao, Int. J. Nanomedicine, 5, 261-267, (2010).

10. Tadashi Kokubo and Hiroaki Takadama, 'How useful is SBF in predicting in vivo bone bioactivity', Biomaterials, 27(15), 2907–2915, (2006).

11. Xiao-Xiang Wanga, Satoshi Hayakawa, Kanji Tsuru and Akiyoshi Osaka, 'Bioactive titania gel layers formed by chemical treatment of Ti substrate with a H2O2/HCl solution', Biomaterials, 23, 1353-1357, (2002).

12. Archana Rajendran, G. Vinoth, V. Shanthi, R. C. Barik and Deepak K. Pattanayak, 'Silver nano particle incorporated Ti metal prepared by chemical treatment for antibacterial and corrosion resistance study', Mat. Tech.: Adv. Biomat., 29(B1), B26-B34, (2014).

13. Johanna Loberg, Ingela Mattison, Stig Hansson, Elisabet Ahlberg, 'Characterisation of titanium implants I: Critical assessment of surface roughness parameters', The Open Biomaterials Journal, 2,18-35, (2010).

14. G. McDonnell and A. D. Russell, 'Antiseptics and disinfectants: activity,action, and resistance', Clin. Microbiol. Rev., 12, 147-179, (1999).

15. S. Pal, Y. K. Tak and J. M. Song, 'Does the antibacterial activity of silver nanoparticles depend on the shape of the nanoparticle? A study of the gram-negative bacterium Escherichia coli', Appl. Environ. Microbiol., 73, 1712-1720, (2007).

16. I. Sondi and B. Salopek-Sondi, 'Silver nanoparticles as antimicrobial agent: a case study on E. coli as a model for Gram-negative bacteria', J. Colloid Interface Sci., 275, 177–182, (2004).

17. S. Y. Liau, D. C. Read, W. J. Pugh, J. R. Furr, and A. D. Russell, 'Interaction of silver nitrate with readily identifiable groups: relationship to the antibacterial action of silver ions', Lett. Appl. Microbiol., 25, 279-283, (1997).

18. A. D. Russell and W. B. Hugo, 'Antimicrobial activity and action of silver', Prog. Med. Chem., 31, 351-370, (1994).

19. Alan B. G. Lansdown, 'A pharmacological and toxicological profile of silver as an antimicrobial agent in medical devices', Volume 2010, Article ID 910686, 16 pages doi:10.1155/2010/910686.

20. D. K. Pattanayak, T. Matsushita, H. Takadama, T. Nakamura and T. Kokubo, 'Effect of HCl concentrations on apatite-forming ability of NaOH–HCl- and heat-treated titanium metal', J. Mater. Sci.:Mater. Med., 20, 2401–2411, (2009).

21. X. X. Wang, S. Hayakawa, K. Tsuru and A. Osaka, 'Bioactive titania gel layers formed by chemical treatment of Ti substrate with H_2O_2/HCl solution', Biomaterials, 23, 1353-1357, (2002).

22. H. M. Kim, F. Miyaji, T. Kokubo and T. Nakamura, 'Preparation of bioactive Ti and its alloy via simple chemical surface treatment', J. Biomed. Mater. Res., 32, 409-417, (1996).

23. S. Nishiguchi, S. Fujibayashi, H. M. Kim, T. Kokubo and T. Nakamura, 'Biology of alkali- and heat-treated titanium implants', J. Biomed. Mater. Res., 67A, 26-35, (2003).

CARBON CONTROL IN POWDER METALS SINTERING, PARTICULARLY IN METAL INJECTION MOULDING FURNACES

Akin Malas[1], Joachim Von Scheele[2], Debashis Roy[2]
[1]Linde AG, Germany
[2]Linde India Limited, Kolkata, India

Abstract: *C- potential control of Powder Metal (PM) Sintering furnaces has been one of the technological improvements in the PM component manufacturing. Extending the possibility of C- potential control in Metal Injection Moulding (MIM) furnaces has been considered but due to higher process temperature, it was not the focus of the development. Advantages of using MIM to improve the mechanical properties of PM components have been compromised by the problems of carbon control in the sintering process. Decarburisation is a difficult issue to address in high temperature furnaces where the reactions are fast and diffusion rates are high. While the PM industry is dealing with cost pressures and challenges of economical crisis all over the world, high quality sinter production is becoming the primary factor in making the buying decision. The quality of any production is directly related to control of process parameters. The metallurgical properties and especially the microstructural changes in a powder metal component can only be controlled by controlling the surrounding furnace atmosphere accurately; however the carbon control of the sintering process has always been incomplete in total process control. It is therefore the primary objective of this paper to give details of a new technology developed by Linde Gas for conventional furnaces for the successful control of carbon potential in a MIM sintering process and leveraging the advantage of the control to produce higher quality product and at the same time to facilitate the lower cost production.*

1. Introduction

High quality sinter production should mean a process in which all parameters are controlled to achieve all product specifications. A failure to control the furnace atmosphere would risk the total quality control. Nevertheless, it has been common practice not to control furnace atmosphere where carbon plays a major role in product quality.

A patented furnace atmosphere control system, SINTERFLEX®, for controlling the C- potential in sintering furnaces specifically designed through cooperation between Höganäs AB, and Linde Gas is described in this paper[1-2]. Details include the results of an industrial scale case study which was carried out in MIM sintering process.

Atmospheres and Furnaces in The Sintering Process

An atmosphere can be neutral, carburizing, decarburizing, oxidizing or reducing, each of which can be a required function for different purposes in the manufacturing industry[3]. In a sintering furnace however, different functions are expected in different zones of the furnace, making sintering furnace atmospheres more challenging in terms of control and optimization.

Similar to traditional lower temperature sintering operations the furnace atmospheres in MIM furnaces also employ nitrogen and hydrogen although in different proportions due to the concerns in protecting furnace components due to higher processing temperatures. Requirements for oxidation/reduction and decarburisation/carburisation functions of a furnace atmosphere in sintering are the same in principle with other heat treatment operations. However the functions expected to work in harmony in the sintering process are somewhat more complex as listed below. These are:

CARBON CONTROL IN POWDER METALS SINTERING, PARTICULARLY IN METAL INJECTION MOULDING FURNACES

1. *Delubrication (or dewaxing or debinding) during preheating :* Since there is a pre-debinding process before the sintering operation in MIM sintering, which transforms the "green body" to a "brown body", this is not considered a primary issue for the process. However the furnace still needs to be capable of oxidizing the binder to be removed from the final expected sinter body. Some furnaces employ humidifiers to facilitate the delubrication process but forward flow of the existing furnace with high hydrogen content will also assist with the removal of lubricant vapours as gaseous components from the furnace.

2. *Oxide reduction at the sintering temperature:* By removing the surface oxides, solid to solid mass transport and diffusion are facilitated. Reduction of oxides can take place in the presence of hydrogen or via reactions with carbon according to the reactions (1), (2) and (3) where Me denotes the metal.

$$MeO + H_2 > Me\ H_2O \ldots\ldots\ldots\ldots\ldots\ldots\ldots(1)$$

$$MeO + C > Me + CO \ldots\ldots\ldots\ldots\ldots\ldots (2)$$

$$MeO + CO -> Me + CO_2 \ldots\ldots\ldots\ldots\ldots\ \ .(3)$$
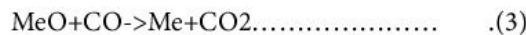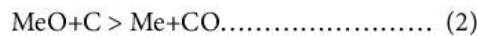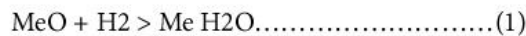
3. *Prevention of oxidation during cooling:* The atmosphere will need to have sufficient reducing agents to protect the pure metal surface from oxidising at high temperatures and the cooling (sinter hardening) down to room temperature.

4. *Control of carbon content at sintering temperature as well as during cooling:* Traditionally and more commonly this is not done in a controlled fashion. The furnaces usually employ a continuous flow of a hydrocarbon, usually natural gas, to keep carbon input in the furnace atmosphere mixture. However in MIM furnace atmospheres, this is usually not the common practice. Due to the control issues the atmosphere only contains nitrogen and hydrogen mixtures. Therefore carbon control and decarburisation has always been considered as a "common problem" in

MIM sintering process. In lower temperature component manufacturing, where a hydrocarbon is used, to increase the C- potential at the sintering temperature by changing the gas composition has been shown to be impractical, as well as producing a high carbon potential at lower temperatures, leading to sooting and excessive carbide formation. This is somewhat more complex and in some cases much more defined in MIM furnaces since there can be sealed zones with internal doors particularly for pre-heating and sintering zones. The control of heat treatment furnace atmospheres usually depends on the thermo chemical equilibrium of carbon and oxygen. The kinetic reactions are generally ignored for gaseous components. The equilibrium approach for sintering atmospheres is more challenging due to the factors highlighted below.

a) Small temperature differences in the overall furnace profile will lead to different carbon and oxygen activities throughout the furnace.

b) Graphite in the powder mixture will react with the atmosphere by usually decarburising

c) Sintering furnaces usually have no circulation fans to assist with convection like in carburising furnaces therefore the atmosphere will not mix completely leading to local carbon and oxygen potential variations.

d) Vaporisation of lubricants will create gas mixtures that might affect the overall furnace atmosphere in terms of carbon potential.

e) The carbon potential differences in local pores and the free atmosphere within the furnace.

Therefore it is quite common to work in ± 0.3%C process window after sintering. This number is around ±0.03%C in carburising applications. Improved carbon control is therefore a major challenge for improving the sinter steel properties. Compared to traditional lower temperature

sintering continuous furnaces, MIM sintering furnaces are smaller in scale and capacity but tighter in terms of furnace atmosphere integrity. Although there are also many batch type furnaces used in the industry, the primary objective of this study was in continuous furnaces where the capacities are higher and control of furnace atmosphere is more challenging.

A New Sintering Atmosphere Control System: SINTERFLEX®

SINTERFLEX® is a new and patented C- potential control technology developed by Linde Gas and Höganäs AB for sintering furnaces. The system uses the simple gas sampling principle of the sintering furnace and a newly designed oxygen probe and internal analysis furnace arrangement to give reference C- potential readings in the sintering zone of the furnace. The system controls the gas composition, particularly its carbon enrichment flow rate to maintain a reliable carbon potential. Knowledge of the oxygen partial pressure in the sintering zone tells the operator the actual conditions during sintering. It can be measured by an oxygen sensor, which determines whether the processed metal is oxidized or whether a metal oxide is reduced. The development study focused on two areas: a new furnace atmosphere to introduce carbon into the sintering zone which can be controllable and responsive to any changes; and a new measurement and monitoring system with an oxygen probe to control this carbon containing atmosphere. The new furnace atmospheres used are mainly mixtures of CO, hydrogen, and nitrogen and additions of propane, in proportions controlled by this new sintering atmosphere control system. A new oxygen probe was developed that could measure very low oxygen partial pressures which are common in sintering furnaces, especially in MIM furnaces, and meet C- potential control requirements.

CASE STUDY: CARBON CONTROL IN MIM SINTERING FURNACE

Linde AG worked with an MIM Company on the application of a new technology developed for conventional furnaces to implement carbon control in high temperature MIM sintering furnaces. The issues mentioned above about the carbon control of sintering furnace atmospheres are amplified by the high temperature of the MIM sintering process. Customer had been experiencing decarburization of parts with final expected specification of 0.4 – 0.6% C. The parts were produced with non-uniform carbon content on each furnace charging boat between 0.1 – 0.4%C. This was particularly a problem for post mechanical and heat treatment operations leading to usually extra cost.

BASF Catamold® FN0205 feedstock was used as the powder mixture with 0.4-0.6%C, 1.9-2.2%Ni and balance Iron. Three different components have been tested during the demonstrations. These are shown in Fig.1 below.

Fig.1 MIM test components.

The furnace is a pusher type MIM sintering furnace employing 20% hydrogen and balance nitrogen atmosphere. Total process time was 7.5 hrs with 14 minutes push each cycle. In order to establish the base line for the carbon control trials, SINTERFLEX® controller was used to monitor the existing conditions. Then the furnace atmosphere was continuously monitored during 4-day demonstrations with changes to the furnace atmosphere constituents including CO / H_2 / N_2 / C_3H_8. During the carbon control tests, the C-potential of the furnace atmosphere was controlled

automatically by SINTERFLEX® at different set points in order to optimize part quality and consistency. Over 200 sintered parts were tested for carbon content in Megamet in-house laboratories and these results are correlated to the set points and realized C- potential using SINTERFLEX®. The furnace and the setup of the SINTERFLEX® system are indicated below in Fig. 2. Base line data indicated that the parts were decarburised at different rates in every batch. Although the furnace oxygen probe readings had been around 1250 mV which suggests that the furnace was quite tight, there seemed to be a fluctuation in C- potential readings.
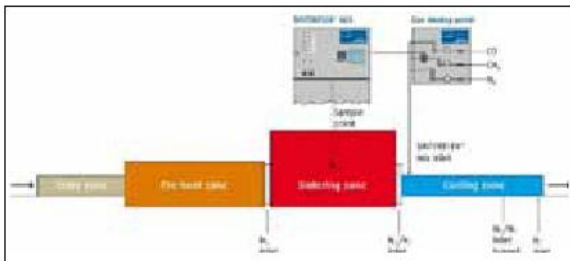

Fig.2 – Test Setup and Gases supply inlet

When the charging boat travels from the exit vestibule to the furnace discharge, hydrogen purge was used to eliminate any air ingress. Due to the pressure caused by this purging the furnace atmosphere could have been shifting in different directions to cause the atmosphere fluctuations, and this might be the cause of the different carbon reading on each part in one single boat. Base line data showed erratic carbon content results ranging from 0.2 to 0.7%C both within and between boats. The graphs below in Fig.3 show the carbon concentration on parts 1 and 2 under existing atmosphere.
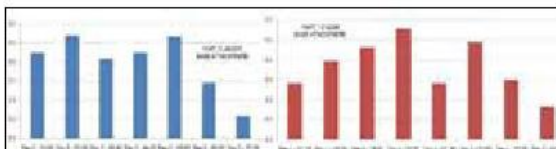
Fig.3 - %C Parts under base atmosphere for parts # 1 and 2

Fig.4 shows the microstructure examination of part 1 under base atmosphere. Decarburisation on the surface and in the core can be clearly seen as white structures.
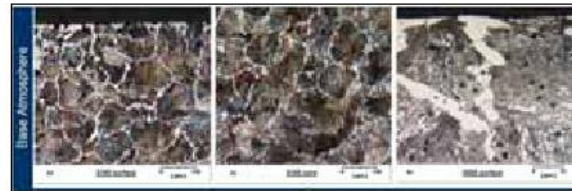
Fig.4 – Microstructure of Part 1 sintered under base atmosphere

The furnace atmosphere then replaced with atmosphere mixture for carbon control. The mixture contained nitrogen, hydrogen, carbon monoxide and propane for enrichment. The trials started with a CO addition of 2% in order to achieve the base atmosphere for the carbon control. However, this value had actually increased the carbon content of the parts up to 1 – 1.4% C on the surface. In addition, surface of these parts with high carbon content was melting due to their reduced melting temperature. Fig.5 shows the phase diagram for mixture of Fe, 2%Ni at different carbon contents. The graph shows that there will be partial melting at 1280°C where the C% is around 1.5.

The tests continued by reduced CO levels but at increasing C- potential levels higher than the current atmosphere C- potential values. SINTERFLEX® measured C- potential as 0.02% at 1280°C during the existing base atmosphere tests. The value was then set to 0.05 – 0.07% depending on different part requirements. The carbon potential setting of the furnace atmosphere was decided from calculations of the amount of oxygen and CO in the furnace. The carbon content of the components will differ depending on the chemical composition of the material being sintered. Their carbon content was calculated by using Gunnarssons' formula (4) and the carbon potential of the atmosphere.

Log Cp/ C= 0.055 (% Si)– 0.013 (% Mn)– 0.040 (% Cr)+ 0.014 (% Ni)

– 0.013 (% Mo) C…………(4)

Also the following formula (5) can be used to calculate carbon potential by using the oxygen probe milivolt values. This is the SINTERFLEX® principle while calculating the carbon potential at given temperatures.

$$Cp = f (T, V, CO, q).........................(5)$$
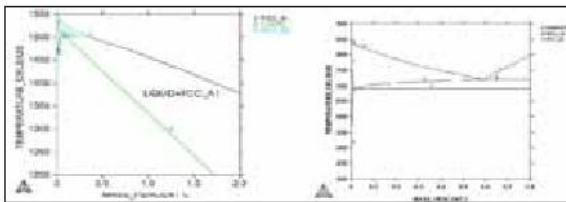
Fig.5 Phase Diagram   *Fig.6 Phase Diagram*
Fe-Ni-C   *Fe-Ni-C*

Where; Cp is the Carbon potential (%), T is the Temperature (K), V is the Probe voltage (v), CO is the Carbon Monoxide (%) and q is the steel alloy factor. Alpha iron undergoes a phase transition from body-centred cubic (BCC) to the face-centred cubic (FCC) configuration of gamma iron, also called austenite. Carburising and decarburising start when the steel microstructure shows austenitic transformation. The temperature when this transformation starts differs depending on the alloy composition. This is approximately 700°C for the alloy used in the tests (Fig.6).

Therefore the C- potential in the furnace at this temperature also plays an important role in determining the decarburisation and carburisation of MIM sintered components. The furnace has several zones where the temperature is around this temperature and it is apparent from the microstructures that the decarburisation had started in the core also after the back bone binder was removed from the brown body. After the delubrication of the sintering part the porosity was quite high and the gas interaction caused

carbon transfer in or out of the material. When the sintering started at the high temperature the decarburisation would slow down due to the low carbon potential requirement at high temperature. Thus the decarburised parts will stay decarburised. Therefore by adjusting the C- potential around 0.05%C at 1280°C will provide approximately 0.6%C at lower temperatures around 700 – 800°C when phase has been transformed to austenite.

The tests continued by keeping the C- potential at these figures for the rest of the trials. The results revealed that uniform carbon contents around 0.5%C (±0.05%) in the parts could be achieved. Fig.7 shows the carbon content of part 1 and 2 after controlled carbon trials. SINTERFLEX® measured and calculated C- potential setting and control showed consistency achieving uniform results in carbon contents in the parts.
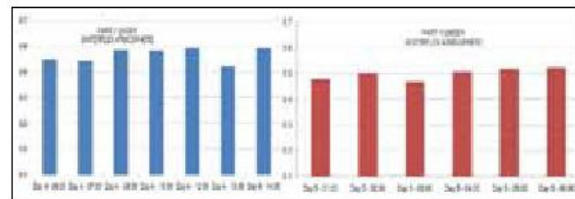
*Fig.7- %C Parts under SINTERFLEX® atmosphere and control for parts # 1 and 2*

Fig.8 also shows the microstructures after carbon control tests ,and, compared to Fig.4 the decarburisation had significantly improved and almost got eliminated in the core due to higher C- potentials at lower temperatures of the furnace. Fig.9 also shows a general overview of comparison of base atmosphere results and the results after SINTERFLEX® trials.
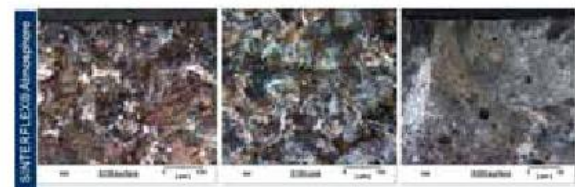
Fig.8 - Microstructure of Part 1 sintered under SINTERFLEX® atmosphere
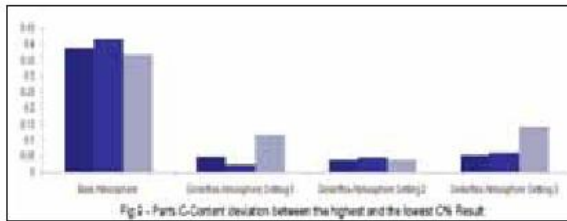
Fig.9 - Parts C-Content deviation between the highest and the lowest C% Result

Conclusions

1. SINTERFLEX® successfully controlled the C-potential of the atmosphere and helped achieve uniformity in the furnace atmosphere.

2. It was possible to establish the best furnace atmosphere conditions for Part numbers 1, 2 and 3 with SINTERFLEX® so that they stay in the 0.4 – 0.6% C content specification window.

3. MIM sintering furnaces have other zones such as pre-heating and cooling where temperatures are above 750°C with the same atmosphere. Carburization and decarburization will happen in these zones also.

4. C- potential measured in high heat temperature zone can be used to introduce trim gases in order to optimize the process and improve part quality and consistency.

5. By taking a reference point for the sampling it is possible to estimate the conditions in the other zones and therefore optimize the overall process accordingly.

6. Other enrichment agents still need to be tested to see their response to C- potential control.

7. SINTERFLEX® Atmosphere Control System is able to provide advisory information or closed-loop control of furnace atmosphere in order to deliver parts with Carbon content specification ranges.

References

1. Akin Malas*, Soren Wiberg*, Daniel Nilsson**, and Sigurd Berg**, "A New approach to sintering furnace atmosphere control and sinter hardening by gas impingement cooling", *Linde Gas Application Development, **Höganäs AB, PM2008 World Congress - Washington D.C.

2. "Sintering of Steel", White Paper, published in 2011, Linde Gas Publications

3. Christoph Laumen*, Akin Malas*, Sören Wiberg** and Sigurd Berg***, "Advanced Carbon Control in Sintering Atmospheres", *Linde Gas Application Development, **AGA Gas AB, ***Höganäs AB, Euro PM 2009 Copenhagen

DENSIFICATION MECHANISM OF OXIDE DISPERSION STRENGTHENED MARTENSITIC STAINLESS STEELS BY SPARK PLASMA SINTERING

K Vinoadh Kumar, S Kumaran

Department of Metallurgical and Materials Engineering, National Institute of Technology, Tiruchirapalli, India

Abstract: In this article, densification mechanism involved in spark plasma sintering (SPS) of oxide dispersion strengthened martensitic stainless steels is discussed. Martensitic stainless steel (410L) powders with 1.5W-1.5Nb-0.25Ti-0.25Zr-0.3Y$_2$O$_3$ powders were mechanically alloyed using planetary ball mill for 60 hours. Milled powders were sintered at 975°C, 1050°C and 1125°C using SPS. Effect of sintering temperature, current and soaking time on the relative density of sintered samples are discussed. Strong dependence of sintering temperature and soaking time was observed on the relative density of the sintered samples. At 975°C, profound influence of soaking time was noticed on the relative density of sintered samples when compared to 1050°C and above. Concepts related to current density and electro-migration are discussed in brief with respect relative density of the sintered samples.

Keywords: Oxide-dispersion strengthened steels, Mechanical Alloying, Spark Plasma Sintering, Densification mechanism

1. Introduction

High-chromium steels are considered as the major promising candidates for the structural components of next generation power plants such as fusion, accelerator driven systems or the so-called fission generation IV reactors. Currently T / P91 steel, industrial and commercially available high-chromium ferritic/ martensitic steels are considered as a good candidate structural materials applicable for such advanced nuclear systems. The aforesaid steels have superior swelling resistance and better mechanical properties at high temperatures compared to austenitic stainless steels. However, their creep resistance is limited to moderate temperature level (<850 K). Thus, to increase the efficiency of the next generation of nuclear power plants it is mandatory to develop a new material preferably steel-based that is capable of sustaining the harsh conditions. Therefore, a substantial effort is being set now a days for the development and investigation of new high-chromium steels

dispersed with nano-oxide in the matrix [1-6]. Powder metallurgy is the only technique to develop dispersion strengthened steels. Some of the problems involved with ODS production based on powder metallurgy are the anisotropy of the mechanical properties, the difficulty to produce large batches, the difficulty of joining/ welding ODS steels with large structures and the high production costs [7-10]. Recent studies report that oxide dispersion strengthened martensitic steels generally provide better void swelling resistance under irradiation than austenitic steels which has a poor creep strength at temperatures over 600°C [11]. Oxide dispersion strengthened martensitic steels have been developed using the addition of nano-oxide particles to increase the high temperature strength. A variety of techniques have been recently reported to synthesize nano-oxide particles namely spark plasma sintering (SPS), chemical methods using metallic salts such as precipitation route, the sol–gel, hydrothermal routes, pyrolysis/ carbothermal treatment, reverse

micelle method [12-13], etc. Among them, SPS is regarded as a rapid sintering method using self-heating action from inside the powder. SPS systems offer many advantages such as ease of operation and accurate control of sintering energy as well as high sintering speed, high reproducibility, safety and reliability. Although SPS has been employed for fabrication of various materials, there exists a significant gap in understanding the fundamental densification mechanisms. However, significant gap exists between the technological and fabrication achievements to the fundamental understanding of the SPS mechanisms. This gap is due to the complexity of the thermal, electrical and mechanical processes that may be involved during the SPS, in addition to their dependence on the SPS parameters. The present work intends to examine the effect of SPS parameters namely, current, temperature and soaking time on the relative densities of the sintered samples. Further, the mechanisms responsible for rapid densification during the SPS were highlighted.

2. Experimental Methods

Martensitic stainless steel (410L) powders (99% pure) along with 1.5W-1.5Nb-0.25Ti-0.25Zr-0.3Y_2O_3 powders (99% purity) were mechanically alloyed under optimized milling parameters. Powders were mechanically alloyed using a planetary ball mill (Insmart systems, Hyderabad, India) with a ball-to-powder mass ratio of 10:1, milling speed of 250 rpm and the milling medium used was toluene. Milled powders were sintered using spark plasma sintering (Dr. SinterLab, SPSS, Japan) with varying temperature and time. High dense graphite die and punches were used to consolidate the milled powders. DC pulsed current with an ON-OFF pulsing duration of 12:2 was used for sintering. During sintering, linear shrinkage and current were monitored and recorded. Density of sintered sample was determined using Archimedes principle. Densification mechanism was studied from the data recorded for every 5 sec by SPS.

3. Results and Discussion

3.1 Effect of temperature and soaking time on densification

Fig. 1 shows the relation between the sintering temperature and relative density without soaking time. Relative density of the sintered samples shows an increasing trend with increasing sintering temperature.
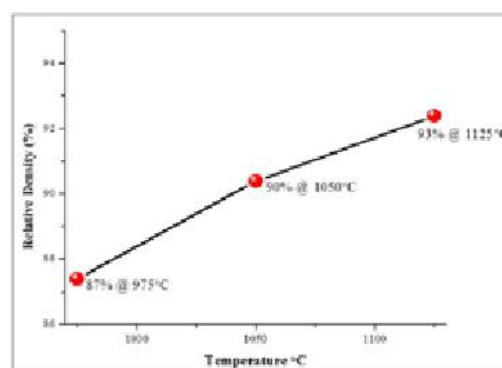
Fig. 1 Relative density of the sintered sample with increasing temperature

Fig. 2 shows the profound influence of soaking time on the relative density of the sintered specimens. There is an increasing trend with increasing soaking at a given temperature. However, the increment in density was better at 975°C when compared with high temperature (1050⁰C). In other words, milled powders responded well to the sintering temperature of 975°C than 1050°C. It is mainly due to fineness of milled powders which accelerates the current density at 1050°C thus promoting enhanced electro-migration finally leading to collision between the electrons and subsequently delaying the densification. Sintering at 975°C is the optimum temperature for better densification. The current density required for electro-migration across the samples was optimum at 975°C. Therefore, there was a substantial increase in the relative density of the sintered sample with increasing the soaking time.
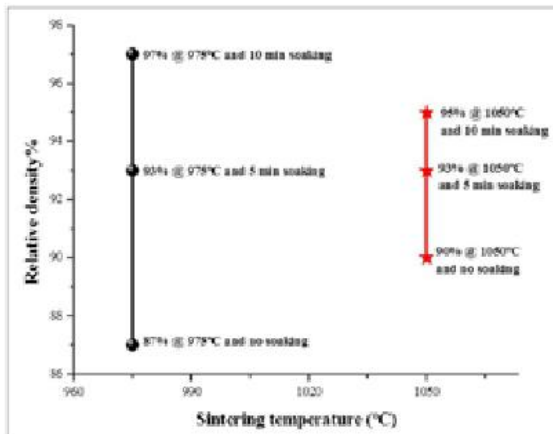
Fig. 2 Effect of soaking time on the relative density of sample with varying temperature

3.2 Effect of Current on the relative density

It is evident from Fig. 3 that there was no substantial densification phenomenon till the current reaches to 350 Amp. This is due to poor flow of electric current in the porous powder aggregates. In order to generate spark during sintering, a minimum current density, i.e., 10 KAcm^{-2} is required. Only above this current density the spark will occur, even if the condition for spark is satisfied the probability for the same event to take place across the particles is initially extremely low [14]. Due to the axially symmetric structure of the die, the pulse current passing through the sample distributes axially symmetric on its cross section thus no eddy current is produced in grains. However, due to the uneven microstructure of the green body, the current passing through the sample has an asymmetric distribution, and the magnetic flux through each grain will change with time so that an eddy current is induced in it. Each grain, being a small heat source forms the in-situ sintering and speeds up the sintering of the green body. On the other hand, the small heat capacity of the heated system and the large heat conductivity of graphite die are the other two important factors for the rapid temperature rise [15]. In the initial stages of sintering due to

relatively poor packing of powders, concentration of current along the discrete favorable paths are possible wherein complete electrical contacts across the powders are achieved. In the intermediate stages of sintering where 70-92% of densification takes place, a temperature gradient is developed near the larger pores compared to smaller pores wherein current density starts to build up in a steep manner as shown in Fig. 3. In the final stages of sintering, the applied current will become inert to linear shrinkage of the compact. The rate of interfacial energy annihilation loses its equilibrium with the rate of grain boundary annihilation. Since no more mis-orientations at crystal level and vacancies at the surface level are present in the system, grain growth becomes predominant in the forthcoming stages. Grain growth can be controlled by optimizing the soaking time of the powder compacts.
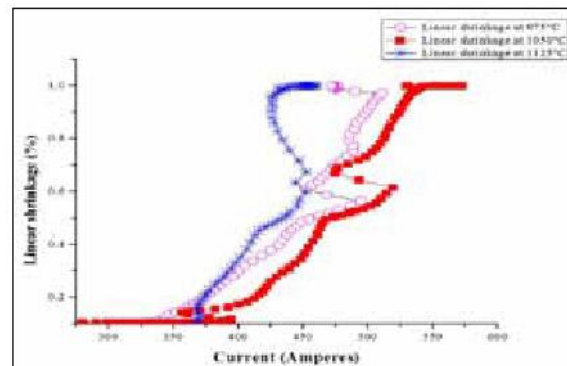
Fig. 3 Effect of Current on the linear shrinkage

3.3 Effect of sintering temperature on the densification behavior

No significant change was observed till 600°C in the linear shrinkage vs temperature curve as shown in Fig. 4. The reasons are irregular particle size, uneven crystal orientation and curvature difference between the adjacent particles, which subsequently hinders the current path across the powder particles. Rate of sintering depends upon two parameters, namely system thermodynamics and kinetics of sintering. System thermodynamics

is a function of particle size wherein kinetics of sintering is a temperature dependent parameter. In the initial stages of sintering, electro-migration is not uniform across the powder particles. Hence, there was no significant shrinkage observed till 600°C. In the intermediate stages of sintering, as the temperature increases slowly the atoms in lattice get excited wherein their bonds get broken from their parent lattice and subsequently these broken bonds develop a fresh bond with the broken bonds of adjacent particles. Since the atom gains mobility as the temperature increases the kinetics of sintering is enhanced which is evident from the steep slope after 600°C. In this stage maximum neck growth equal to 0.5 times the initial diameter of the particle is expected and the pores will be interconnected. Further number of vacant sites also increases wherein the mobile electron gets filled inside the vacant sites. In the final stage of sintering, major transport mechanism decides the densification is grain boundary diffusion. As the time passes by the mis-orientation between the adjacent particle decreases, stress levels between the solid-vapor interface decreases, atomic motion wherein mass flow reduces, interfacial energy as a function of di-hedral angle decreases, energy to create vacancy and energy to move atoms into the vacant sites also decreases. Thus a saturation point with respect to densification or linear shrinkage is observed at the end of this stage.
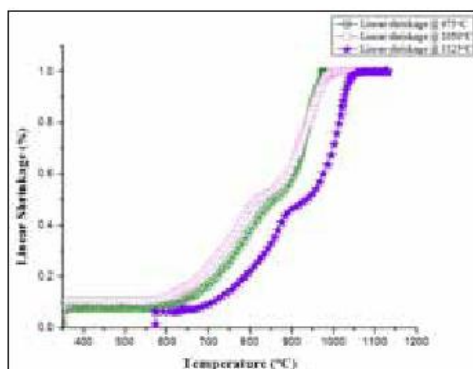
Fig. 4 Effect of sintering temperature on linear shrinkage

Conclusion

Strong dependence of sintering temperature and soaking time on relative density of the sintered samples was observed. Maximum relative density of 97% was observed at 975°C for a soaking time of 10 min. In terms of relative density of the sintered samples, mechanically alloyed powders respond well at 975°C than at 1050°C. Major reason behind the same is the perfect sync that exists between the particle size and electro-migration at 975°C, wherein at 1050°C electron discharge plays starts dominating leading to increased collision and poor densification. Effect of soaking time was also predominant at 975°C which is well complimented by the significant amount of variation in the relative density of sintered samples.

References

1. R. Lindau, A. Möslang, M. Rieth, M. Klimiankou, E. Materna-Morris, A. Alamo, A.A. F. Tavassoli, C. Cayron, A.M. Lanchad, P. Fernandezd, N. Baluce, R. Schäubline, E. Diegelef, G. Filacchionig, J.W. Rensmanh, B.v.d. Schaafh, E. Luconi, W. Dietzj, "Present development status of EUROFER and ODS-EUROFER for application in blanket concepts", J.Nucl.Mater. Vol. 75-79, 989–996 (2005). doi:10.1016/j.fusengdes.2005.06.186.

2. Z. Oksiuta and N. Baluc, "Microstructure and Charpy impact properties of 12–14Cr oxide dispersion-strengthened ferritic steels", J. Nucl. Mater. Vol. 374, 178-184 (2008). doi:10.1016/j.jnucmat.2007.08.004.

3. A. Alamo, J.L. Bertin, V.K. Shamardin and P. Wident, J. Nucl. Mater.Vol. 367-370, 54–59 (2007). doi:10.1016/j.jnucmat.2007.03.166.

4. C. Degueldre, S. Conradson and W. Hoffelner, Comp. Mater. Sci. Vol. 33, 3-12 (2005). doi:10.1016/j.commatsci.2004.12.019.

5. S. Ukai, T. Nishida, H. Okuda, M. Fujiwara and K. Asabe, J. Nucl. Sci. Technol., Vol. 34, 256-263. (1997). doi: 10.1080/18811248.1997.9733658.

6. ShigeharuUkai, Shunji Mizuta, TunemitsuYoshitake, Takanari Okuda, Masayuki Fujiwara, Shigeki Hagi and Toshimi Kobayashi, J. Nucl. Mater.Vol.283-287, 702-706. (2000). doi:10.1016/S0022-3115(00) 00114-8

7. M. Li and S. Mann, "Emergent Nanostructures: Water-Induced Mesoscale Transformation of Surfactant-Stabilized Amorphous Calcium Carbonate Nanoparticles" in Reverse Microemulsions,Advanced Functional Materials, Vol. 12, 773-779 (2002).

8. G. A. J. Hack, "Developments in The Production of Oxide Dispersion Strengthened Superalloys", Powder Metallurgy, Vol. 27, 73-79 (1984). DOI: http://dx.doi.org/10.1179/pom.1984.27.2.73.

9. Jung-Ho Ahn,Hwi-Jun Kim, Ik-Hyon Oh and Yong-Jin Kim, "Preparation of nano-sized ODS alloys by ball-milling using metallic salts", J. Alloys Compd.,Vol. 483, 247-251 (2007).

10. A.A.F Tavassoli, Present limits and improvements of structural materials for fusion reactors – a review, J. Nucl. Mater.Vol. 302, 73-88 (2002).doi:10.1016/S0022-3115(02)00794-8.

11. R.E. Gold and D.L. Harrod, "Mechanical properties of vanadium and vanadium-base alloys", International Metals Reviews Vol. 25, 163-222 (1980). DOI: http://dx.doi.org/10.1179/imtr.1980.25.1.163.

12. B.N. Singh and J.H. Evans, "Significant differences in defect accumulation behaviour between fcc and bcc crystals under cascade damage conditions", Journal of Nuclear Materials, Vol. 226, 277–285 (1995). doi:10.1016/0022-3115(95)00121-2.

13. Junyan Wu,Fei Chen, QiangShen, JulieM. Schoenung, and Lianmeng Zhang, "Spark Plasma Sintering and Densification Mechanisms of Antimony-Doped Tin Oxide Nanoceramics," Journal of Nanomaterials, Hindawi Publishing Corporation, Vol. 2013 (2013).doi:10.1155/2013/561895.

14. Maryse Demuynck, Jean-Pierre Erauw, Omer Van der Biest, Francis Delannay and Francis Cambier, "Densification of alumina by SPS and HP: A comparative study", Journal of the European Ceramic Society Vol. 32, 1957–1964. (2012). doi:10.1016/j.jeurceramsoc.2011.10.031.

15. K. Madhav Reddy, Nitish Kumar and BikramjitBasu, "Inhibition of grain growth during the final stage of multi-stage spark plasma sintering of oxide ceramics", Scripta Materialia Vol. 63, 585–588. (2010) doi:10.1016/j.scriptamat.2010.06.004.

CONSOLIDATION OF MECHANICALLY ALLOYED Al5083 -5wt% Y₂O₃ NANO-COMPOSITE BY EQUAL CHANNEL ANGULAR PRESSING (ECAP)

K. Chandra Sekhar[1], Pravir Polly[1], S. Kumaran[1], B. Ravisankar[1]
[1]Department of Metallurgical and Materials Engineering, National Institute of Technology, Tiruchirrappalli, India

Abstract: In the present work, Al-5083(99% purity) - 5wt% nano-yttria powders were milled for 10, 15 and 20hrs in a high energy ball mill under optimised process parameters. The powders were characterised by X-ray diffraction (XRD) and scanning electron microscopy (SEM). Milled powders at 10hrs exhibited nano-crystalline single phase. Consolidation of 20 hrs milled powder was done by equal channel angular pressing (ECAP) through 90o die channel angle using route A for two passes with and without back pressure. Density of ECAPed samples were measured using Archimedes principle. The density was 94% for the sample consolidated with backpressure after second pass. There was an increase in hardness with increase in number of passes.

Keywords: Mechanical Alloying, Al-5083 composite, ECAP, Characterisation.

1. Introduction

Of late, there is a tremendous demand in developing newer materials and processing techniques in order to meet the fast growing engineering fields such as automobile, aerospace etc. When compared with monolithic alloys aluminium composites give higher stiffness to density ratio and better properties at elevated temperatures [1]. Aluminium and alloys are widely used in the above said engineering fields due to their high strength to weight ratio, good corrosion resistance, etc. Further enhancement in mechanical strength of aluminium alloys is very much viable by adopting newer or non-equilibrium processing techniques such as mechanical alloying (MA), severe plastic deformation, etc. MA is a powder processing technique used for the production of nano-crystalline materials in a high energy ball mill [3]. It is a process in which the mixture of powders are milled together and material transfer takes place resulting in a homogeneous alloy. In this process the alloy will be formed in the first stage and the particle refinement will be achieved in the subsequent stages [4]. Ultrafine grained or nano structured materials can be obtained by the action

of cold welding fracturing and re-welding between metallic and ceramic particles in an activated milling media during high energy ball milling. Severe plastic deformation technique is another technique which can be used to produce bulk ultrafine grained structured materials. Ultra-fine grained structures are polycrystals having average grain size less than 1µm and will have equiaxed microstructures having high fraction of grain boundaries with high misorientations angles and high dislocation density [7].

Equal channel angular pressing is one of the severe plastic deformation process used for the grain refinement of bulk materials by the applications of high strain and has unique features such as no change in shape and minimum load requirements [8]. High shear strain in ECAP will able to disrupt the surface oxide layer and a good bond will create between particles and is an effective method for consolidation of powders at relatively low temperature and loads with no porosity [10]. ECAP is an attractive technique because it is relatively easy to setup and use an ECAP die. In this exceptionally high strains can be imposed either through repetitive

pressing or multiple pass dies and relatively large bulk materials can be produced easily [11].

Besides, consolidation of powders by normal ECAP, work had been in progress by consolidation of powders by application back pressure during ECAP.

2. Experimental Work

Elemental powders of the 5083 aluminium alloy composition (Al with Mg, Mn, Zn, Cu, Cr, Ti, Fe) and nano-yttria were chosen to synthesise nano-composite powders through high energy ball milling (Make : Insmart systems, Hyderbad). The chemical composition (wt%) of the Al 5083 alloy is given in table.1. The input powders were milled in an optimised milling parameters such as milling speed, ball-to-powder ratio, milling time, etc. The process parameters are listed in table 2. The powders were taken at regular interval in order to understand the formation of nano-structured single phase during milling.

Cr	Cu	Ti	Zn	Fe	Si	Mn	Mg	Al
0.05	0.1	0.15	0.25	0.4	0.4	1.0	4.9	Balance

Table.1 chemical composition in wt% of Al-5083

Process Parametre	Optimised Value
Milling Speed	250 RPM
Ball-to-powder ration	10:1
Milling medium	Toluene
Vials and Balls	HSS vial and stainless steel balls
Milling time	20 hours

Table.2 Process parameters

The powder milled for 20hrs was consolidated by ECAP. A schematic diagram of an ECAP die used in this study is shown in Fig.1. The die angle is 90° and the outer arc of curvature is 20°, and the diameter of the channels and the diameter of the punch were 12mm.
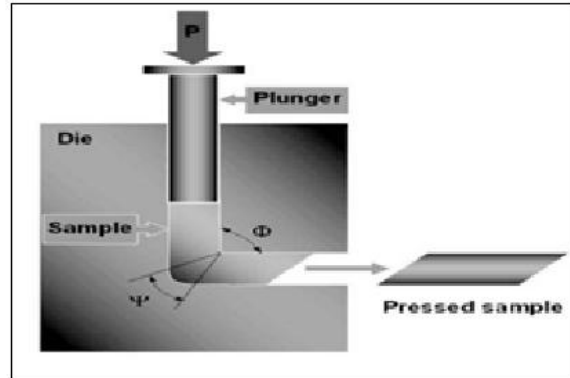
Fig. 1. Schematic representation of ECAP die

The powders were filled in aluminium can of 60mm height and 8mm diameter. The can was pressed through 90° die angle through route A. Aluminium can with powders was ECAPed with and without backpressure for two passes using hydraulic press. Can was removed by machining process after consolidation.

3. Results and Discussion

3.1 Phase and Physical Properties of Milled Powders

XRD spectrum of the mechanically alloyed Al-5083 with yttria powder with varying intervals of milling time is shown in Fig.2. Milling at 10hrs has resulted nano-crystalline structure. Solute elements such as magnesium and other traces have been dissolved in aluminium with increasing milling time. The presence nano-yttria is also identified in the powders. These patterns clearly show the broadening of peaks with increasing milling time. This is attributed by refinement of crystallite size and strain. Table.3 shows the crystallite size of the 10, 15, and 20 hours milled powder.

Fig.2. XRD Pattern of Al-5083 powders synthesised by MA at different intervals

Milling Time(hours)	Crystallite size(nm)	Particle Size(μm)
10	117	20
15	64	13
20	57	8

Table.3 Crystallite size and Particle size of 20 hour milled powder

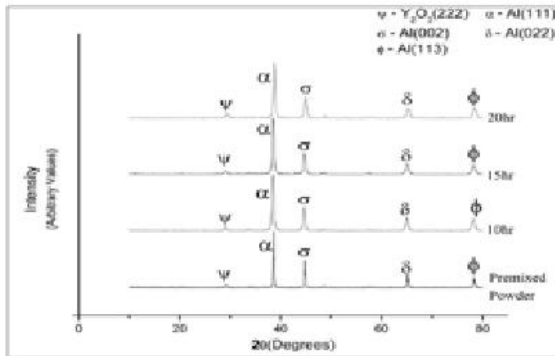Fig. 3 shows the SEM micrographs of Al-5083 nano composite milled for different milling intervals. Average particle size for 10, 15 and 20hrs milled powders is measured by SEM micrographs and Image J software. It is inferred that particle size decreases with increasing milling time. It shows that there is a severe deformation between the particles during milling. The Morphology is found to be irregular shape. The average particle size of Al-5083 composite for different milling time is listed in table 3.

3.2 Density

The actual density of Al 5083 with 5% Yttria is calculated by rule of mixture and found to be 2.81gm/cm^3. The relative density increases with increasing number of passes. It is also observed that there is a marginal improvement in density with back pressure. Table.4 shows the relative density of ECAPed samples with back pressure and without backpressure of sintered and un sintered samples. The pressure less sintering of ECAP greatly
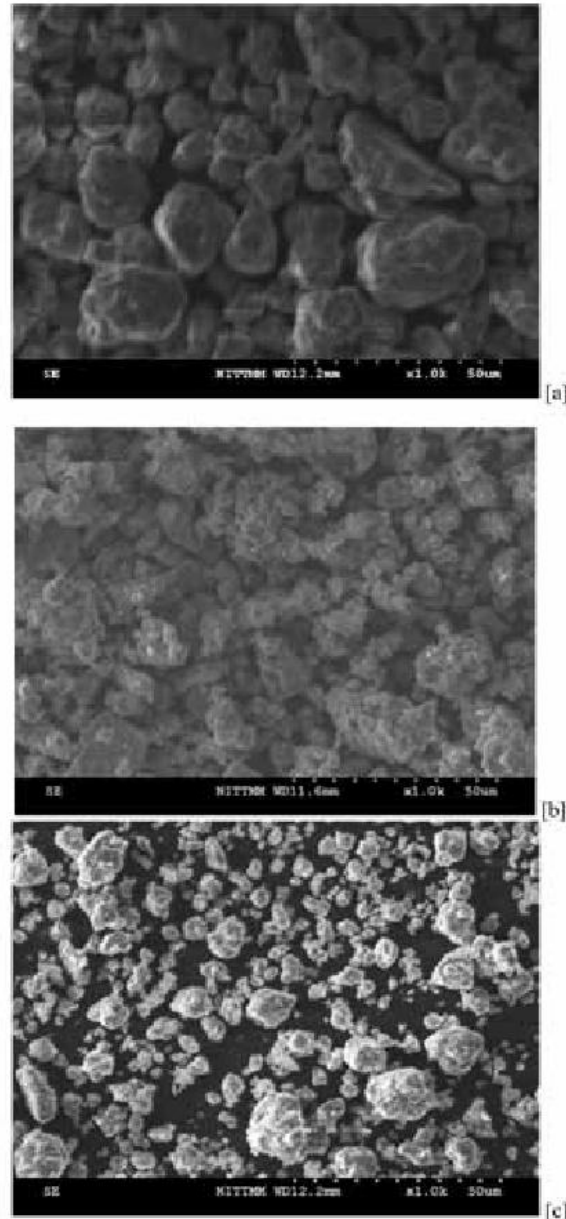

Fig.3 SEM Micrographs of Al-5083 nano composite a) 10hrs b) 15hrs and c) 20hrs

increases the density by achieving better bonding between the particles. Maximum density of 94% of its theoretical density is achieved after sintering the ECAPed samples.

3.3 Hardness

The actual hardness value of Al-5083 in annealed condition is approximately 54HRB. Hardness of Al-5083 with yttria increases to 82HRB. Presence of Y_2O_3 nano-particles in Al-5083 matrix enhances the hardness significantly both at room temperature and sintered condition. Table.4 shows the hardness of un sintered and sintered ECAP samples. The hardness increases is due to the dispersion and grain refinement.

Number of Passes	Relative Density (%)		Rockwell Hardness (HRB)	
	Without Back Pressure	With Back Pressure	Without Back Pressure	With Back Pressure
First pass	81	86	59	65
First pass Sintered	84	88	71	80
Second pass	89	90	63	78
Second pass Sintered	92	94	76	82

Table.4 Relative Density and Hardness of 20hr ECAPed sintered and unsintered samples

Usually, exposing to higher temperatures, the UFG materials may tend to grain coarsen and the hardness decreases. In the present case, decrease in hardness is not observed. Sintering improves the bonding between the particles, with less effect on grain coarsening. The Y_2O_3 dispersion may act as grain refiner to the ECAPed samples, restricting the grain growth thus simultaneously increasing hardness and density on sintering. However, a detailed study is required to understand the effect of sintering and ECAP which is in progress.

4. Conclusions

Ball milling of Al-5083 composite powder at 20hrs has resulted nanostructure with particle refinement. Crystallite size decreases with increasing milling time. Particle size decreases with increase in milling time and minimum particle size is 8μm at 20hrs of milling time. The maximum density of 94% has achieved with back pressure, for which the Hardness observed is 82HRB.

References

1. M. Khakbiz and F. Akhlaghi, Journal of Alloys and Compounds Vol. 479, 334–341. (2009).

2. Sivaiah Bathula, R.C. Anandani, Ajay Dhar and A.K. Srivastava, Materials Science and Engineering, Vol A 545 97, 102 (2012).

3. C. Suryanarayana, E. Ivanovb and V.V. Boldyrev, Materials Science and Engineering Vol A304–306, 151–158 (2001).

4. C. Suryanarayana "Mechanical alloying and milling", Progress in Materials Science Vol. 46, 1-184. (2001).

5. Z.Horita, T.Fujinami, M.Nemoto and T.G.Langdon, Journal of materials processing technology Vol.117, 288-292 (2001).

6. Nishtha Gupta, S.Ramesh Kumar, B.Ravisankar and S.Kumaran, World Academy of Science, Engineering and Technology 61 (2012).

7. Ruslan Z. Valiev and Terence G. Langdon Progress in Materials Science Vol. 51, 881–981, (2006).

8. R. Derakhshandeh. H and A. Jenabali Jahromi Materials and Design Vol. 32, 3377–3388 (2011).

9. Ramu Yarra, P.Venkatachalam, S.Ramesh Kumar, B.Ravisankar, K.Jayasankar and P.S. Mukherjee, Transactions of The Indian Institute of Metals, Vol. 63, Issue 5, 813 – 817 October (2010)

10. Jiri Dvorak, Petr Kral, Martin Balog, Frantisek Simancik and Vaclay Sklenicka METAL. (2010).

11. Terence G. Langdon, Materials Science and Engineering Vol. A 462, 3–11. (2007).

12. Cheng Xu, Kenong Xia and Terence G. Langdon Acta Materialia Vol 55, 2351–2360 (2007).

13. Roberto B. Figueiredo, Megumi Kawasaki, Cheng Xu and Terence G. Langdon Materials Science and Engineering Vol. A 493, 104–110 (2008).

14. Zenji Horita, Takayoshi Fujinami and Terence G. Langdon, Materials Science and Engineering Vol. A 318, 34–41 (2001).

15. Mahdi Rafieia, Saeed Khademzadeha and Nader Parvin, Journal of Alloys and Compounds Vol. 489, 224–227 (2010).

16. C. Suryanarayana, Journal of Alloys and Compounds Vol. 509S, 229–234. (2011).

17. E.T. Kubaski, O.M. Cintho and J.D.T. Capocchi, Powder Technology, Vol. 214, Issue 1, 25, 77-82. November (2011).

18. Li Lu and M.O. Lai, Materials & Design, Vol. 16, Issue 1, 33-39. (1995).

19. S. Rosenkranz, S. Breitung-Faes and A. Kwade, Powder Technology Vol. 212, 224–230. (2011).

20. M. Abdellaoui and E. Gaffet, Acta metall, mater. Vol. 43, No. 3, 1087- 1098, (1995).

21. Behtash Mani, Mohammad Jahedi and Mohammad Hossein Paydar, Powder Technology Vol. 219, 1–8. (2012).

22. M.H. Paydar, M. Reihanian, E. Bagherpour, M. Sharifzadeh, M. Zarinejad and T.A. Dean, Materials and Design Vol. 30, 429–432. (2009).

TENSILE AND IMPACT BEHAVIOUR OF SWAGED TUNGSTEN HEAVY ALLOYS

M Sankaranarayana, U Ravi Kiran, T K Nandy

Defence Metallurgical Research Laboratory, Hyderabad, India

Abstract: Tungsten heavy alloys with Co and Mo additions (W-6Ni-2Fe-2Co and W-6Ni-2Fe-1.5Mo-0.5Co) were synthesized by liquid phase sintering under H_2 atmosphere. This was followed by thermo-mechanical processing that comprised double swaging with an intermediate heat treatment. About 40% deformation was imparted during swaging. Subsequently, a detailed characterization of microstructure and mechanical properties that included hardness, tensile and impact was carried out. In the alloy containing higher Co, the volume fraction of matrix was found to be higher whereas the contiguity of W-W grains was relatively lower as compared to the Mo containing alloy. Also, the matrix phase in higher Co containing alloy exhibited higher W content. The difference in microstructure was found to have a profound influence on mechanical properties as the higher Co containing alloy exhibited superior tensile and impact properties. This was further corroborated by fractographic evidence. While the failed sample of higher Co containing alloy showed increasing evidence of W cleavage and ductile dimples in the matrix phase, the Mo containing alloy exhibited features related to W-W de-cohesion. Improved mechanical properties in higher Co-containing alloy were attributed to lower contiguity of W grains.

Keywords: Tungsten heavy alloy, Tensile Properties, Impact Properties, Fractography

1. Introduction

Tungsten heavy alloys are two-phase composites consisting of nearly rounded tungsten grains dispersed in a low melting point ductile matrix containing metals such as nickel, iron, copper and cobalt [1–3]. These alloys offer unique combination of mechanical properties (associated with the bcc tungsten phase and the fcc matrix), easy machinability, high modulus of elasticity, good corrosion resistance, high absorption capacity against X-Rays and Gama-Rays. Tungsten heavy alloys have been used for a long time for penetrator applications. Since, the as- sintered tungsten alloy which suffers from poor mechanical properties cannot meet the requirement, thermo mechanical processing is needed for the enhancement of mechanical properties. As a part of general thermo mechanical processing strategy, swaging combined with intermediate heat treatment is usually employed in order to realize desired properties. Boris and Katavic [4] showed that the mechanical properties of W–Ni–Fe-Co are far superior to those of W–Ni–Fe alloys. Bose et al. [5-7] added Mo to tungsten heavy alloys and observed improvement in mechanical properties, especially strength. Although earlier research on tungsten heavy alloys has mainly focused on tensile behaviour, limited data exists on charpy impact properties and their relationship with microstructure and tensile properties [8]. In the present study, two tungsten heavy alloys that contain W, Ni, Fe, Co and Mo have been investigated in detail with respect to microstructural, tensile and impact properties. The effects of volume fraction of tungsten and matrix composition on mechanical properties have also been investigated. Additionally, failed specimens of tensile and impact have been studied in a greater detail in order to explain the properties.

2. Experimental

Commercially available elemental tungsten, nickel, iron and cobalt powders, with their characteristics listed in Table 1, were used as starting materials for synthesizing the liquid phase sintered 90W-6Ni-2Fe-2Co (WNFC) and 90W-6Ni-2Fe-1.5Mo-0.5Co (WNFM) alloys.

Powder	W	Ni	Fe	Co
Purity, wt. %	99.9	99.6	99.6	99.6
Average particle size, µm	11	6	5	4
Apparent density, g/cc	4.81	1.03	3.23	2.23
Tap density, g/cc	5.84	1.36	3.53	2.81

TABLE 1: Purity and average particle size of elemental W, Fe, Ni and Co powders.

The elemental powders were mixed in a ball mill for 24 h, and the powders were reduced at 700° C in H_2 atmosphere for 2 h in order to remove surface oxides. The reduced powders were then isostatically cold-pressed applying pressure of 2.5 kbar and sintering was conducted at 1460° C for 2 h in a continuous pusher type furnace (FHD Furnace Limited, UK). The rods were vacuum heat treated for 5 h at 1150 ° C, and then oil quenched. After vacuum treatment, the sintered rods were subjected to swaging with 40% reduction in area. The microstructure of the samples was examined by optical and scanning electron microscopes. The average grain size of tungsten phase and volume fraction of phases was determined using an image analyzer. Contiguity, defined as the relative fraction of tungsten-tungsten interfacial area, was determined by placing grid lines over the binary image and counting the number of tungsten- tungsten and tungsten- matrix intercepts. It was calculated using the equation:

$$C_{SS} = 2N_{SS}/(2N_{SS}+N_{SL}),$$

where N_{SS} and N_{SL} are the number of tungsten-tungsten grain boundaries and tungsten-matrix interfaces intercepted, respectively. The tensile specimens were prepared as per ASTM standard T-145 and tested at room temperature using universal tensile testing machine (INSTRON 5500R, UK). After the tensile tests, the failure features in the fractured tensile specimens were investigated by LEO Scanning Electron Microscope (SEM). Charpy impact values were determined according to ASTM Standards (E-23) [9] using charpy sub-size un-notched specimens at room temperature. Fractographs of the broken tensile and impact test pieces were carried out using SEM. Hardness of the sintered compacts was measured using Vickers hardness tester (Vickers Instruments, Model: 1965, UK).

3. Results

Fig. 1 shows the optical micrograph of liquid phase sintered and heat treated tungsten heavy alloys. The higher cobalt containing alloy (WNFC) shows coarser tungsten particles as compared to the molybdenum containing alloy (WNFM). Fig. 2 shows the grain size, contiguity and volume fraction of matrix phase in the two alloys. Higher volume fraction of matrix phase and lower contiguity of tungsten particles are readily discernible in WNFC alloy.
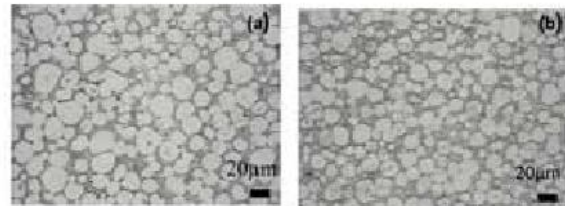

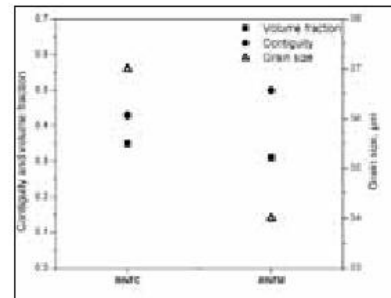*Fig 1: Optical micrographs of (a) WNFC and (b) WNFM tungsten heavy alloys.*

Fig 2: Grain size, contiguity and volume Fraction variation in WNFC and WNFM tungsten alloys.
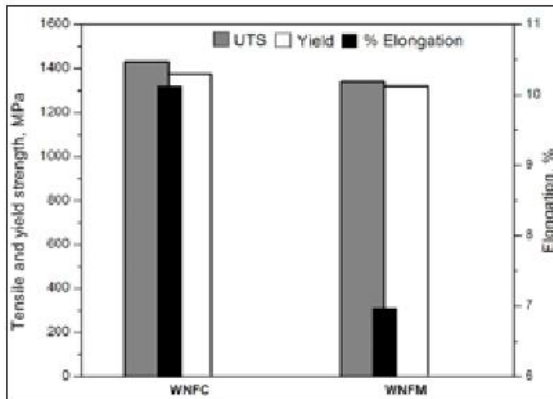
Fig 3: Comparative tensile properties of WNFC and WNFM tungsten alloys.

Fig. 3 shows comparative average tensile properties of two alloys. WNFC alloy shows superior tensile properties as compared to WNFM. Fracture surface of failed tensile specimens of both the alloys are shown in Fig.4. Cleavage fracture of tungsten grains with river line patterns are seen in the case of WNFC. Evidence of tearing in the surrounding matrix phase is also discernible. The Mo-containing alloy, on the other hand, shows frequent evidence of de-cohesion along W-W interfaces characterized by flat features. Occasionally, shallow dimples in the tearing region are also observed.
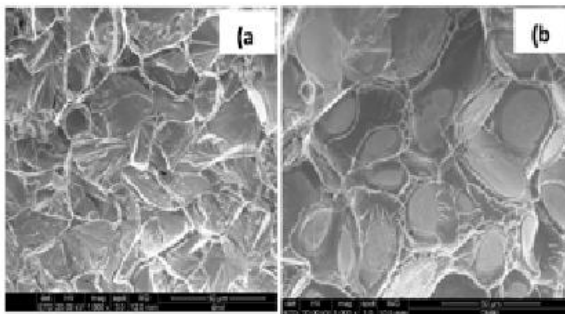

Fig 4: Tensile fractographs of (a) WNFC and (b) WNFM alloy
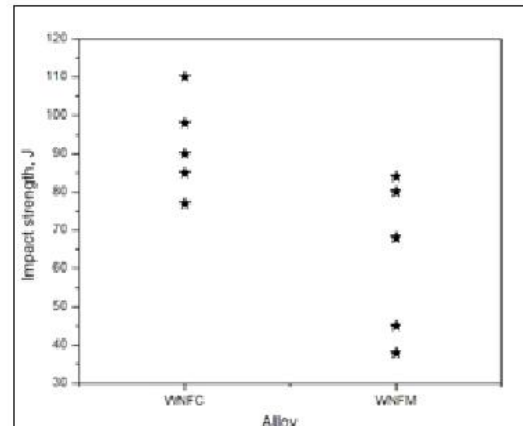
Fig 5: Impact toughness scatter in WNFC and WNFM tungsten alloys.

Impact test results are shown in Fig.5. While impact values of WNFM range from 40-90 J, those of WNFC alloy vary from 75-110 J. Fractographs of failed impact specimens for the lowest impact value in Mo containing alloy and lowest plus highest impact values in Co containing alloy are shown in Fig. 6. The Mo containing alloy show ample evidence of W-W decohesion (Fig. 6a). Such instances are mostly absent in Co-containing alloy (Fig. 6 b&d). The cobalt containing alloy shows ample evidence of ductile dimples in the tearing region (Fig. 6d) especially in high impact energy specimen, which in WNFM alloy is sparse.

Fig 6: Impact fractographs of (a) WNFM-High and (b) WNFC-Low (c) WNFC-High and (d) WNFC-High impact value tungsten alloys (Insert showing ductile tearing).

4. Discussion

4.1 Microstructure

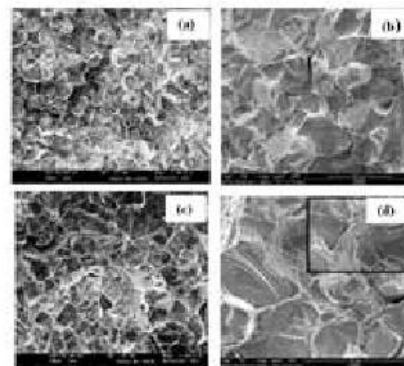Significant difference in the tungsten particle size of WNFM and WNFC alloys, which is primarily a result of different processes that occur during liquid phase sintering, is not observed. In liquid phase sintering, the initial stage involves melting of the matrix alloy, separation of W-particle agglomerates and penetration of molten matrix. This is followed by partial dissolution of W-particles and therefore reduction in the particle size. Subsequently as the equilibrium composition of the matrix is reached, the larger particles grow at the expense of smaller particles. In the final stages the particles grow by Ostwald ripening as the volume fraction of W particles remains constant. Therefore, the final particle size depends upon how these steps are influenced by alloying addition. Sintering temperature and time are same for both the alloys and therefore can be ignored. In the present study, the Mo containing alloy (WNFM) exhibits marginally finer structure as compared to the Co containing alloy. While the difference is not significant, the refinement of tungsten particles may be attributed to Mo restricting the solubility of tungsten in the matrix phase which in turn inhibits the kinetics of dissolution and re-precipitation of tungsten on larger grains. The microstructure of WNFC and WNFM are also different in terms of volume fraction of matrix phase which is significantly more in WNFC as compared to WNFM alloy (Fig.2). This may be attributed to tungsten content that is more in the matrix of the Co containing alloy. This has implications with regards to contiguity of W- W grains. For a constant particle size higher volume fraction of the matrix phase is expected to result in larger separation between tungsten particles and therefore lower contiguity. Indeed, WNFC that has lower volume fraction of tungsten shows lower contiguity (Fig.2). Attempt was also made

to measure dihedral angle (an indicator of matrix penetration between W particles) in both the alloys.

4.2 Mechanical Properties

Tensile properties (Fig.3) indicate superior properties of Co-containing alloy (WNFC) over Mo containing alloy (WNFM). Earlier work done on Mo containing alloy has established that beyond 9% Mo, there is formation of intermetallic leading to deterioration in mechanical properties [10]. However in the present work, the amount of Mo is considerably less thereby eliminating the possibility of intermetallic formation. Mo partitions to both W particle and the matrix. This leads to increase in strength and corresponding decrease in ductility in relation to the base alloy. However in this study the amount of Mo in W-phase is extremely small. Therefore the effect of Mo on the properties of the alloy is primarily through its influence on the matrix phase that has higher amounts of Mo. The improvement in tensile properties of higher Co containing alloy (WNFC) over Mo containing alloy is attributed to three microstructural factors: (1) increasing volume fraction of the matrix phase, (2) decrease in dihedral angle that suggests better penetration of the matrix phase and (3) reduced contiguity of W- W particles that is the weakest link in the microstructure. Another favourable factor is increased solid solution strengthening of the matrix phase in WNFC alloy due to higher tungsten content. Improvement in mechanical properties of tungsten alloys with the addition of Co has also been reported by Katavic and Odanovic [11]. Impact property also shows a similar trend that is WNFC alloy has significantly higher impact values as compared to WNFM. This improvement can be attributed to the microstructural parameters mentioned above. The results of the present study are in agreement with this observation as the Co containing alloy has lower contiguity than the Mo containing alloy. Additionally, evidence of ductile

dimples in high impact Co containing specimen as compared to low impact Mo containing specimen corroborated this observation. The presence of ductile dimples in WNFC may be attributed to relatively higher volume fraction of the matrix phase. It must be added here that considerable scatter in the impact properties (Fig. 5) is due to the fact that the alloys are processed by powder metallurgy and inhomogeneity in the microstructure may exist leading to variation in mechanical properties.

5. Conclusions

The investigation of the microstructure, tensile and impact properties of two tungsten heavy alloys based on W-Ni-Fe-Co (WNFC) and W-Ni-Fe-Co-Mo (WNFM) showed the following results:

1. WNFC (alloy containing higher cobalt) exhibited superior tensile properties as compared to WNFM alloy (containing Mo).

2. While tensile specimens of WNFC alloy failed by predominant cleavage of tungsten grains showing river line patterns, WNFM alloy showed flat features indicating de-cohesion along W-W grains.

3. WNFC alloy showed superior impact properties as compared to WNFM alloy. Failed impact specimens of WNFC showed more evidence of tearing and ductile dimples than WNFM.

4. Superior mechanical properties especially tensile strength, % elongation to failure and impact of WNFC over WNFM are attributed to lower contiguity of W- W grains and higher W in the matrix phase (thereby leading to solid solution strengthening) in the former alloy.

Acknowledgements

References

1. A. Upadhyaya A. "Processing strategy for consolidating tungsten heavy alloys for ordnance applications". Mater Chem Phy, Vol. 67, 101–110 (2001).

2. J. Ryu, Hong SH and Baek WH. "Microstructure and mechanical properties of mechanically alloyed and solid state sintered tungsten heavy alloys", Mat Sci Eng A, Vol.291, 91–96 (2000).

3. Y. Li and F. A. Mohamed, Rev Particulate Mater Vol. 3, 71 (1995).

4. B. Katavik and M. Nikacevic, "Properties of the cold swaged and strain aged P/M 91W–6Ni–3Co heavy alloy". Second International Conference on: Deformation Processing and Structure of Materials, May 26–28, Belgrade, Serbia and Montenegro. 135–140 (2005).

5. A. Bose and R.M. German, "Sintering atmosphere effects on tensile properties of heavy alloys". Metall Trans A, Vol. 19A, 2467–76 (1988).

6. A. Bose and R.M. German. "Rhenium alloying of tungsten heavy alloys", Powder Metall Int ,Vol. 21(3), 9–13 (1989).

7. A Bose and R.M. German, "Matrix composition effect on the tensile properties of tungsten–molybdenum heavy alloys", Metall Trans A, Vol. 21A, 1325–7 (1990).

8. K.S. Churn, J. W. Noh, H. S. Song, E. P. Kim, S. Lee, and W. H. Baek. "The Effect of Contiguity on the Mechanical Properties of 93W-5.6Ni-l.4Fe Heavy Alloy", Proceedings of International Conference on Tungsten and Tungsten Alloys, Metal Powder Industries Federation, 397, edited by A. Bose and R. J. Dowding, McLean, VA, 1992.

9. ASTM E23-0a. Standard test methods for un-notched bar impact testing of powder structural parts (2002).

10. L. Kuan-Hong and L. Shun-Tian, "Variables on the precipitation of an intermetallic phase for liquid phase sintered W–Mo–Ni–Fe heavy alloys", Int J Refract Met Hard Mater Vol.20, 401-408(2002).

11. B. Katavik, M. Nikacevic, "Properties of the cold swaged and strain aged P/M 91W–6Ni–3Co heavy alloy", Second International Conference on: Deformation Processing and Structure of Materials, May 26–28, 2005, Belgrade, Serbia and Montenegro, 135–140 (2005).

HOT UPSET FORGING STUDIES ON Al-2.5%TiO$_2$-C HYBRID POWDER METALLURGY COMPOSITE

M.Ravichandran [1], A.Naveen Sait [1], V. Anandakrishnan [2]
[1] Chendhuran College of Engineering and Technology, Pudukkottai, India
[2] National Institute of Technology, Tiruchirappalli, India

Abstract: *This paper is an attempt to study the hot forging characteristics of Al-2.5%TiO$_2$-C hybrid powder metallurgy composite preforms, which is anticipated to have large application in the near future. Aluminium with TiO$_2$ and graphite powders are ball milled in order to yield the composition like: pure Al, Al+2.5%TiO$_2$, Al+2.5%TiO$_2$+2%C, Al+2.5%TiO$_2$+4%C and Al+2.5%TiO$_2$+6%C. The compaction behaviors of powders were studied by compressibility analysis. The physical characteristics of powders such as apparent density, tap density were measured using standard density cup and the theoretical density of the various powder blends are calculated using standard formula. Sintering was done in muffle furnace at a temperature of 600ºC for a period of 3 h and the microstructure was analyzed for sintered preforms. Hot forging was done for the sintered preforms and the densification and deformation characteristics were investigated by correlating true axial stress, true axial strain, and lateral strain with percentage theoretical density. The decreased densification and deformation characteristics were observed for Al+2.5%TiO$_2$+6%C hybrid composite preforms when compared with pure Al and Al+2.5%TiO$_2$ preforms.*
Key words: *Metal Matrix Composites, Hot forging, Powder Metallurgy.*

1. Introduction

Aluminum matrix composites are used in various applications in aerospace, automobile, military and electronic industry due to low density, high toughness, good mechanical properties and high corrosion resistance [1]. So many types of reinforcements are used to produce the aluminum matrix composites. Among these, the titanium-di-oxide (TiO$_2$) is found to be good, since it has high hardness, high modulus, and wear resistance. Adding a single reinforcement to the matrix material improves the strength and hardness of the material. Hybrid aluminum matrix composites are used for high performance ceramic brake disks as it is able to withstand extreme temperatures. With the addition of solid lubricant particles such as graphite to produce hybrid composites, the tribological properties of the composites can be improved effectively [2]. Recently aluminum alloy–graphite particulate composites are being used in various applications because of their low

friction and wear, improved machinability, low thermal expansion and high damping density [3]. Mohammed T. Hayajneh et al. synthesized self-lubricated aluminum/alumina/graphite hybrid composites by powder metallurgy techniques and studied machining parameters during drilling process using artificial neural network modeling [4]. The homogeneous dispersion of fine reinforced particles in a fine grained matrix is beneficial to the mechanical properties of MMCs [5]. Mechanical milling affects the morphology and hardness of powder particles thus influencing the compressibility of milled powders [6]. The physical characteristics of powders are very important for a successful manufacturing of the product. Generally, the apparent density, tap density and true density are evaluated for study of physical characteristics [7]. There are several manufacturing techniques for particle reinforced MMCs such as liquid metal infiltration, spray decomposition, and squeeze casting, compo casting, powder metallurgy and

mechanical alloying. In order to overcome some of the drawbacks associated with the conventional stir casting techniques, powder metallurgy (PM) techniques can be employed because usually, the microstructure of PM materials is largely isotropic and texture-free and segregation-free [8]. The important issue in sintered powder metallurgy components is porosity that can be eliminated by the secondary hot forging operations by which the mechanical properties improved [9]. J.C. Shao et al studied flow behavior and hot workability of the powder metallurgy 20 vol. % SiCP/2024 Al composite and reported that large instable regions are present in the form of cavitations located at the matrix/SiCP interfaces and within the SiCP clusters [10]. G.Abouelmagd reported that generally both hardness and compressive strength are enhanced by the addition of Al$_2$O$_3$ and Al$_4$C$_3$ and their magnitudes continued to improve up to deformation temperature of 150° C during hot compression [11].

The main aim of present work is to prepare Al / TiO$_2$ / C hybrid composite by using powder metallurgy techniques and study the densification and deformation behavior during hot forging. The physical characteristics like apparent density, tap density and true density have been studied. The compressibility behaviors of the powders are also analyzed. Microstructure analysis also carried out for the sintered specimens to reveal the presence of reinforcement particles.

2. Experimental Details

Atomized aluminum (Al) powder size -325 mesh and the purity 99.7% supplied by Kemphasol, Mumbai, India was used for the matrix material and rutile phase of titanium-dioxide (TiO$_2$) and graphite powders supplied by the Acechemie (India) were used as the reinforcement material. The required mass of Al, TiO$_2$ and C were accurately weighed in an electronic weighing machine. The blending was carried out in a ball mill. The balls and powders weight ratio was 10:1 and the speed of the drum was selected as 400 rpm. Compressibility study was carried out in a 400 KN computerized hydraulic press supplied by Venus instruments, Maharashtra. The punch and die were made using high carbon die steel and accurately machined. The die was loaded with powder and the density was measured after compaction at predetermined pressure. Then the powders were compacted in same hydraulic press used for compressibility analysis for the specimen dimensions of 24 mm dia and 12 mm height. The sintering was done in a muffle furnace at the temperature of 590°C for a period of 3 hours. The cross section of the sintered sample was prepared for the microstructure analysis. The hot forging was done after heating the sintered sample to 350°C in a furnace for a period of 2 h. The uniform incremental load was applied and the change in dimensions such as height and diameter of the preforms after deformation were noted. These measured values were used to calculate the true axial stress, true axial strain lateral strain and percentage theoretical density. The density of the preforms was measured by Archimedes principle.

3. Results and Discussion

3.1 Physical properties of milled powders

Apparent density or bulk density of a powder is a density when the powder is in the loose state and the tap density is the highest density that can be achieved by vibration of powder. The theoretical density, apparent density and tap density values are provided in Table 1 for each composition. The maximum theoretical density was obtained for Al+2.5%TiO$_2$ composites because of presence of higher density TiO$_2$ particles. The theoretical density values are decreased for the Al+2.5%TiO$_2$+6%C composite because of the presence of more low density graphite particles. The apparent density and tap density was increased while adding 2.5 % TiO$_2$ to the pure aluminum matrix. The increase in density clearly indicates the lower friction between the hard reinforcement and soft matrix. The apparent and tap densities were increased as the percentage of graphite reinforcement added to the Al+2.5%TiO$_2$

composite powders due to the lubrication properties of graphite particles.

3.2 Compressibility study of milled powders

Figures 1 and 2 show the compressibility studies of Al powders mixed with various weight percentages of TiO$_2$ and C. The compaction behavior is an important characteristic for fabricating the complex shapes from metal powders. The compressibility study was carried out to identify the compaction pressure for compaction process. The plot between the density and compaction pressure is shown in Fig.1 and it is used to ensure the required density of the compacts. From the graph it is evident that the density of the compacts increases with increase in compaction pressure. The maximum compaction density (2.66 g/cc) was obtained for the Al+2.5%TiO$_2$ composite for the compaction pressure of 500 MPa, however, for the same compaction pressure the minimum density (2.52 g/cc) was obtained for the Al+2.5%TiO$_2$+6%C composite. The addition of more soft graphite particle reduces the green compact density. Fig. 2 shows the plot between the percentage theoretical density and compaction pressure. This graph was drawn to identify the compaction pressure for the desired green percentage theoretical density. The percentage theoretical density increases while increasing the compaction pressure. The maximum percentage theoretical density (97.56 %) was obtained for the Al+2.5%TiO$_2$ composite at 600 MPa.

The compressibility of the powders or compression ratio CR was measured and is given by (ρg/ρa), where ρg, green density and ρa, apparent density. The apparent density, green density and the compression or compact ratio of the composite powders at 500 Mpa compaction pressure are given in Table 2. The green density of the preforms decreased as the percentage of graphite reinforcement addition is increased. The lowest compaction ratio was achieved for the

Al+2.5%TiO$_2$+6%C composite powders and highest was obtained for the Al+2.5%TiO$_2$ composite.

Composites	Theoretical Density (g/cc)	Apparent Density (g/cc)	Tap Density (g/cc)
Pure Al	2.70	0.95	1.26
Al+2.5%TiO$_2$	2.72	0.97	1.26
Al+2.5%TiO$_2$+2%Gr	2.69	0.98	1.34
Al+2.5%TiO$_2$+4%Gr	2.67	0.99	1.34
Al+2.5%TiO$_2$+6%Gr	2.64	1.03	1.39

Table 1 Physical property of composite powders Gr, Graphite = C

Composites	Green Density (ρ_g)	Apparent density (ρ_a)	Compact Ratio (C_R)
Al+0%TiO2	2.60	0.95	2.73
Al+2.5%TiO2	2.66	0.97	2.74
Al+2.5%TiO2+2%Gr	2.60	0.98	2.66
Al+2.5%TiO2+4%Gr	2.56	0.99	2.60
Al+2.5%TiO2+6%Gr	2.52	1.03	2.45

Table 2 Green density (ρg) and Compact ratio (CR) of composite powders, Gr, Graphite = C
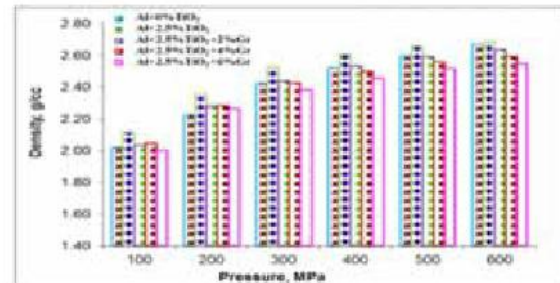
Fig.1 Plots of Density versus pressure (MPa), Gr, Graphite = C
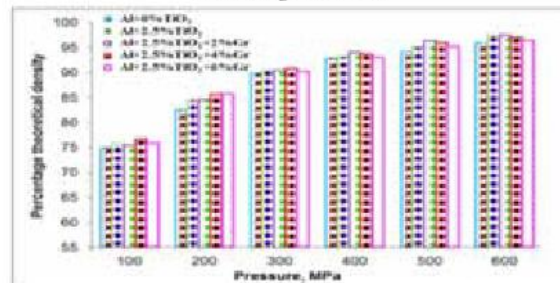

Fig.2 Plots of % theoretical density versus pressure (MPa), Gr, Graphite = C

3.3 Microstructural analysis of sintered composite

The microstructure of sintered pure Al is shown in Fig.3 (a) and composite containing various wt.

% of TiO$_2$ and graphite are shown in Fig.s 3(b-e). The uniform distribution of TiO$_2$ reinforcements in the Al matrix was observed for the Al-2.5%TiO$_2$ composite [Fig.3 (b)]. The distribution of TiO2 in the matrix along with graphite is shown Fig. 3(c & d) for the hybrid composites. Agglomeration of TiO$_2$ and graphite were identified in the composite contains 6% of graphite with 2.5% TiO$_2$. From the microstructure analysis it can be seen that, the pure Al contains pores and these pores are occupied by the reinforcement particles in Al-TiO$_2$ and Al-TiO$_2$-C composites.
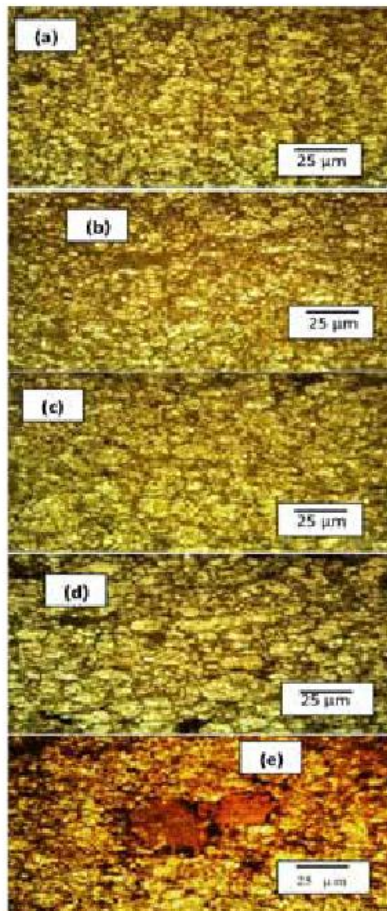

Fig.3 Microstructure of (a) sintered pure Al and (b-e) Al+2.5%TiO2, Al+2.5%TiO2+2%C, Al+2.5%TiO2+4%C and Al+2.5%TiO2+6%C composites

3.4 Hot upset forging

3.4.1 True axial stress versus True axial strain

Fig. 4. shows the graph drawn between true axial stress and true axial strain of Al, Al+2.5%TiO2, Al+2.5%TiO$_2$+2%C, Al+2.5%TiO$_2$+4%C, Al+2.5%TiO$_2$+6%C composite preforms. Evidently, the true axial stress required was more for lower rate of deformation at the initial stage while compare with final stage for all the preforms. The addition of reinforcement increases the stress level. The reason for the increase in applied stress is due to the closing of pores by the fine reinforcement particles. Among the different preforms, the sintered plain Al exhibits the largest level of deformation at lowest axial stress values. Addition of 2.5% TiO$_2$ to the Al matrix and 2, 4 and 6 % of graphite to the Al+2.5%TiO$_2$ composite required more applied stress than the stress required for pure Al preforms for any level of deformation. The sintered composite preforms containing 2.5% titanium dioxide and 6% graphite needed more applied load for the same level of deformation. Hence it is understood that, the addition of the reinforcement resists the plastic deformation during the hot upsetting. The hard reinforcement is surrounded in the soft Al matrix resulting greater resistance to plastic deformation [Fig. (6)]. Addition of these reinforcements contributed to the microstructural changes in the composites.

3.4.2 True axial stress versus Lateral strain

Fig. 5 shows the plot between true axial stress and lateral strain for Al, Al+2.5%TiO$_2$,Al+2.5%TiO$_2$ +2%C,Al+2.5%TiO$_2$+4%C, Al+2.5%TiO$_2$+6%C compacts . It is evident from these curves that the lateral deformation trend was very similar to that observed for axial deformation. However the magnitude of lateral strains (lateral deformation) was smaller than the true axial strain (axial deformation). It could be also understood that the lateral deformation was lower for Al+2.5%TiO$_2$, Al+2.5%TiO$_2$+2%C,Al+2.5%TiO$_2$+4%C,

Al+2.5%TiO$_2$+6%C composites preform than pure Al preform. Better lateral deformation was observed for the plain Al preforms and the addition of TiO$_2$ to the Al matrix and addition of graphite to the Al+2.5TiO$_2$ composite affected lateral deformation of the composites.
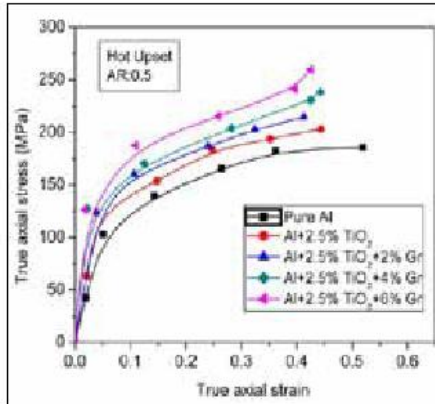

Fig. 4 Plots of true axial stress versus true axial strain, Gr, Graphite = C
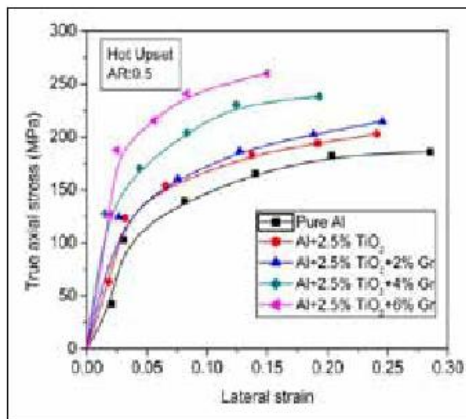

Fig. 5 Plots of true axial stress versus lateral strain, Gr, Graphite = C

3.4.3 True axial stress versus Percentage theoretical density

Fig. 6 shows the variation of percentage theoretical density with respect to true axial stress for the preforms containing various weight percentages of titanium dioxide and graphite during hot upsetting.

The better densification was observed for the plain Al preforms for the lowest applied stress. Addition of 2.5 wt. % TiO$_2$ to Al matrix decreased the densification a little and required more applied stress. In the same way, the addition of 2, 4 and 6 wt. % of graphite to Al+2.5%TiO$_2$ composite decreased the densification while the required applied true axial stress increased. In the case of pure Al preforms the pores were deformed during hot upsetting while; in the composite preforms the pores were occupied by (TiO$_2$ & C) reinforcements. The latter resisted the deformation and took more applied stress for further densification. The poor densification was observed for Al+2.5%TiO$_2$ composite containing 6 wt. % of graphite as compared with pure Al preform.

3.4.4 Percentage theoretical density versus True axial strain

Fig. 7 shows the plots of percentage theoretical density versus true axial strain used to study the densification and deformation behavior of the preforms during hot upset forging. The trend observed for all the preforms were similar and the better densification and deformation was observed for the plain Al. Addition of titanium dioxide and graphite to the Al matrix decreased the densification and deformation due to the matrix work hardening.
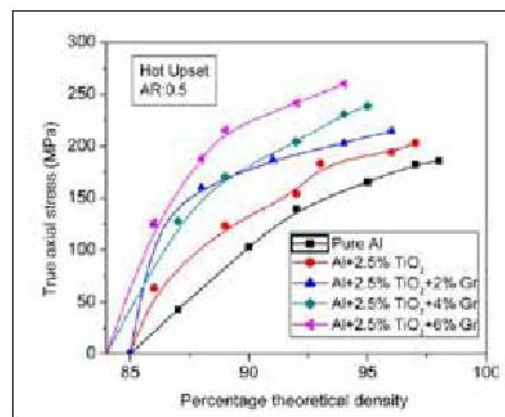

Fig. 6. Plots of true axial stress versus percentage theoretical density, Gr, Graphite = C
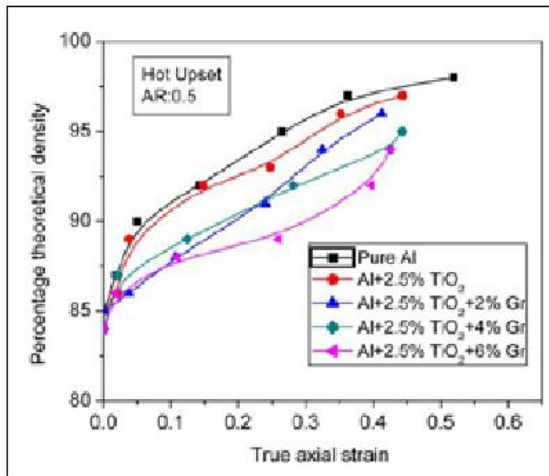
Fig.7 Plots of percentage theoretical density versus true axial strain, Gr, Graphite = C

Conclusions

- Aluminum hybrid composites containing various weight percentages of TiO$_2$ and Cwere synthesized through powder metallurgy route and their densification and deformation characteristics were studied during hot upsetting.

- The maximum apparent density, tap density and minimum compact ratio were obtained for Al+2.5%TiO$_2$+6%C composite.

- Microstructure analysis of sintered specimens revealed a uniform distribution of reinforcements (TiO$_2$ and Graphite) in the Al matrix.

- The sintered pure Al exhibits better deformation and densification during hot upsetting. Addition of TiO$_2$ and Graphite reinforcements to the matrix material decreased the axial as well as lateral deformation.

References

1. Mehdi Rahimian , Nader Parvin and Naser Ehsani, "The effect of production parameters on microstructure and wear resistance of powder metallurgy Al–Al$_2$O$_3$ composite", Materials and Design Vol. 32, 1031–1038 (2011).

2. Yahya Altunpak & Mustafa Ay and Serdar Aslan, "Drilling of a hybrid Al/SiC/Gr metal matrix composites", International Journal of Advanced Manufacturing Technology, DOI 10.1007/s00170-011-3644-4.

3. F. Akhlaghi and S.A. Pelaseyyed, "Characterization of aluminum/graphite particulate composites synthesized using a novel method termed in-situ powder metallurgy", Material Science and Engineering , Vol. A 385, 258–266. (2004).

4. T. Mohammed. Hayajneh, Adel Mahmood Hassan and Ahmad Turki Mayyas, "Artificial neural network modeling of the drilling process of self-lubricated aluminum/alumina/graphite hybrid composites synthesized by powder metallurgy technique", Journal of Alloys and Compounds Vol. 478, 559–565 (2009).

5. S. Sivasankaran, K. Sivaprasad, R. Narayanasamy and Vijay Kumar Iyer, "An investigation on flowability and compressibility of AA 6061 100–x-x wt. %TiO$_2$ micro and nanocomposite powder prepared by blending and mechanical alloying", Powder Technology, Vol. 201, 70-82. (2010).

6. Z. Razavi Hesabi , H.R. Hafizpour and A. Simchi, "An investigation on the compressibility of aluminum/nano-alumina composite powder prepared by blending and mechanical milling", Material Science and Engineering Vol. A 454–455, 89–98 (2007).

7. George E.Dieter, Mechanical Metallurgy, SI Metric Edition, McGraw-Hill Book Company, London, (1988).

8. Ali Mazahery and Mohsen Ostad Shabani, "Study on microstructure and abrasive wear behavior of sintered Al matrix composites", Ceramics International Vol. 38, 4263–4269 (2012).

9. R.E.D Mann, R.L. Hexemer Jr, I.W. Donaldson, D.P.Bishop, "Hot deformation of an Al-Cu-Mg powder metallurgy alloy", Material Science and Engineering Vol. A, 528, 5476-5483 (2011).

10. J.C. Shao, B.L. Xiao, Q.Z.Wang, Z.Y.Ma and Y.Liu, K.Yang, "Constitutive flow behavior and hot workability of powder metallurgy processed 20 vol.%SiCP/2024Al composite", Material Science and Engineering Vol. A, 527, 7865-7872 (2010).

11. G.Abouelmagd, "Hot deformation and wear resistance of P/M aluminum metal matrix composites", Journal of Materials Processing Technology Vol. 155-156, 1395-1401 (2004).

CONTINUOUS HOT ISOSTATIC PRESSING – POSSIBLE DESIGN CONFIGURATIONS

[1]Y.V. Satya Kumar, [2]Yogendra Singh, [2]Bidit Nath
[1] School of Engineering and Technology, Ansal University, Gurgaon, India.
[2]School of Engineering and Technology, Sharda University, Greater NOIDA, India.

Abstract: *Hot Isostatic Pressing (HIPing) is an effective bulk manufacturing process of materials for advanced, strategic, engineering or priority applications. However, HIPing's main deficiency is its nature of batch processing, which limits its utility in industry for bulk processing. A simple conceptual framework proposed recently by the main author of this paper drew upon some ideas from different fields such as Space Technology, Inter-Ocean Travel, Glove Boxes, In-line Annealing, besides small Components in use for VHP or HT environments. However, to illustrate the idea further to enable development by teams of engineers, detailed designs are developed with perspective views for three possible configurations. Two of these include mechanical automation for material handling within the Zones. The proposed design is expected to make HIPing, when further developed, into a widely usable and more affordable bulk manufacturing process adaptable by many more genres of industries than presently possible in its existing batch avatar.*
Key Words: *Continuous Hot Isostatic Pressing, Continuous HIPing, C-HIPing, Design Configurations, Batch HIPing, Near Net Shape, Production Capability Enhancement.*

I. Introduction

Hot Isostatic Pressing (HIPing), in its sixth decade of service to the P/M communities around the World, continues to receive much attention [1-3] by academicians and researchers in materials processing and industrial managers with dedicated and regular conferences, reviews, overviews, patents and process HIP modeling software. Due to the utility of HIPing as an important and potential net shape manufacturing process in emerging economies such as India, the PM Conferences in India have in the recent past witnessed discussion of summary [2] of HIPing process and utility, difficulties associated [4] with densification during HIPing, porosity development during use of HIPed samples [3,4], conceptualization for extension of HIPing into a continuous process [5] for broader utility, affordability and wider practice in manufacturing and the causes for and containment of porosity development [3,4] in compacts upon HIPing. The recent paper on Continuous HIPing [5] first provided a simple conceptual framework using examples of existing technologies in Inter-Ocean Travel through Channels, Vacuum/Gas Handling in Glove Boxes, Conveyor Systems in In-line Annealing, Space Technology for Spacewalks, besides small Components/Accessories developed for use in various VHP and HT environments. Presently, the trend in near-net shape manufacturing has been toward developing bigger and bigger Batch HIP Units. The largest HIP was indicated to be [6] the Giga-HIP® owned and operated by Metal Technology Co. Ltd. and made by Avure Technologies with loads up to 28 metric tons at temperatures up to 1350 °C and pressures of 118 MPa and dimensions of 4.2 m by 2.05 m. Avure announced recently the development of the largest and fastest HIP [7], TeraPi, for manufacture of impellers, turbines and manifolds. TeraPi is capable [6] of handling 75 ton load with a work zone of 3.14 m by 5 m and is provided with automated

loading and unloading of parts. In reality, most engineering industries in emerging markets may not be able to easily justify expensive operation of Batch HIP, which tends to be prohibitive except for high-end components. To realize its full potential, it is imperative that Batch HIP has to evolve into a Continuous HIP process such as that of a Blast Furnace by adapting features presently in other technologies or by developing other necessary features and by integrating them. To this end, three design configurations are presented to serve as a starting point for development by HIP manufacturers, who are also inclined [8].

II. Engineering Design - A Few Relevant Fundamentals as per Dieter and Schmidt

As per Blumrich [9] "Design establishes and defines solutions to and pertinent structures for problems not solved before, or new solutions to problems which have previously been solved in a different way." National Research Council concluded [10] that the real key to world competitive products lies in high quality product design. Summarizing the Importance of Engineering Design Process, Dieter and Schmidt [11] observed that

1. "Decisions made in the design process cost very little in terms of the overall product cost but have a major effect on the cost of the product"

2. "You cannot compensate in manufacturing for defects introduced in the design phase"

3. "The design process should be conducted so as to develop quality cost-competitive products in the shortest time possible."

Dieter and Schmidt [11] had also defined the Four C's of Design as Creativity, Complexity, Choice and Compromise. The Complete Design Process had been divided into 7 Phases by Asimow [12] in what he termed as Morphology of Design, which saw slight changes by Dieter and Schmidt [11] (as below) to the Asimow's Terminology to conform to

current practice: Conceptual Design, Embodiment Design, Detail Design, Planning for Manufacture, Planning for Distribution, Planning for Use, and Planning for Retirement of the Product.

The present paper deals with Embodiment Design, while a preceding paper [5] at PM-10 dealt with the Conceptual Design. As per Dieter and Schmidt [11], the Phases of Conceptual and Embodiment Design may be considered to be composed of different aspects as below:

Conceptual Design [11]:

Define problem, Gather information, Concept generation, Evaluate and Select component.

Embodiment Design [11]:

Product architecture, Configuration design, Parametric design and Detail design.

Here, the present paper deals with the Product Architecture. Dieter and Schmidt [11] defined Product Architecture as determining the arrangement of physical elements of the design into groupings, called modules that are also known as subsystems or clusters.

Based on the Type of Interface, Dieter and Schmidt [11] classified Modular Architectures as the following:

1. Slot-Modular (with each interface being different type)

2. Bus-Modular (a common interface or bus to which modules attach and detach)

3. Sectional-Modular (common and identical type interface between modules attached permanently)

Accordingly, the proposed Architecture here may be termed as Sectional-Modular sub type.

All the Design Phases are discussed in much further detail by Dieter and Schmidt [11] in their seminal compilation on Design, which would be useful for

any Design Team from any type of Industry. One may argue that the proposed design herein (and its preceding Conceptual Design Proposal [5] by the Main Author in a previous PMAI Conference) for Continuous HIPing process is justified in the attempt to improve productivity (and thus improve cost effectiveness for more possible applications) in an otherwise almost prohibitively expensive near-net shape P/M manufacturing Batch HIPing process, especially in emerging markets.

III. Proposed Approach to Continuous HIP Design

A concept model for Continuous HIPing with 5 zones (pressure vessels) and 4 intermittent locks

(Fig. 1) had recently been suggested [5]. The three alternative design configurations proposed here share the common ideas of zones (with steady temperature and pressure being maintained within each zone and inevitable slight variations due to adjoining locks), intermediary locks between the zones (with ramping up or down of temperature and pressure for equalization with preceding or succeeding zones for opening of adjoining doors), differential conveyors, sliding doors for locks and regular subsystems found in Batch HIPing for maintaining temperature, pressure, vacuum and gas levels along with corresponding instruments for measurement and control. In addition, provision is made for stacks and automated/ robotic manipulation in two of these specific configurations with a single conveyor for storage of samples or components undergoing HIPing within each zone. Conveyors proposed are of differential nature, which are either limited to within each zone and within each lock or may straddle the adjoining zone and lock as per final design and practical convenience. The robotic manipulators/arms may be modeled after a human functionality for maneuverability with primary arm (body), secondary arm (upper arm), tertiary arm (forearm), quaternary arm (palm) and knuckled grippers (fingers with knuckles). Although these

designs are presented as a first step, the idea behind them may be developed further with considerations of different operating variables, suitable materials for Pressure Vessels, stresses involved at operative temperatures and pressures and safe operating variables. The exact dimensions and shapes of the pressure vessels (zones), locks, conveyors, robotic manipulators and stacks would depend on rigorous analyses.
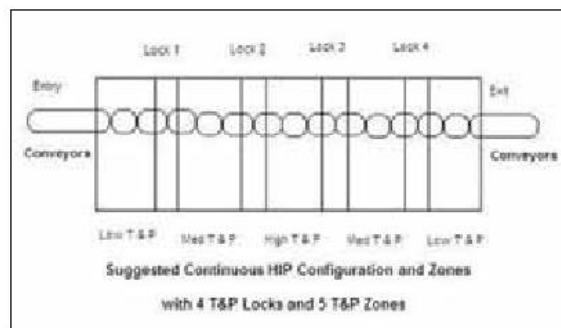

Fig. 1: Sketch of Conceptual Design of Continuous HIPing [5]

IV. Design Configuration - 1 Cylindrical - Single Conveyor - with Robo-Arm for Storage Stacks

A cylindrical shaped pressure vessel is easy for fabrication with cost benefit and provides an advantage in terms of associated stresses when compared to more complex shapes. Each Cylinder serves as a Zone.

Z_i Zone (i = 1, 2, 3, S, 5, 6, 7)

a ambient conditions/zone

s soak conditions/zone

T_i, P_i Temperature and Pressure (i = a, 1, 2, 3, S, 5, 6, 7, a)

Cir Conveyor Roller (i = 1, 2, 3, S, 5, 6, 7) and (r = A or B)

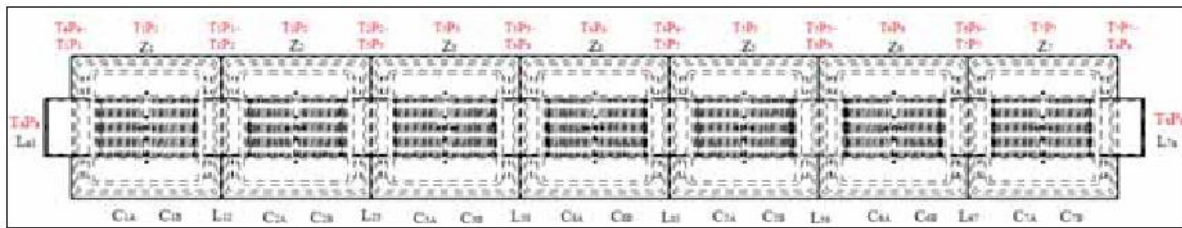L_{xy} Lock b/w Zone x and Zone y (x, y = a, 1, 2, 3, S, 5, 6, 7, a)

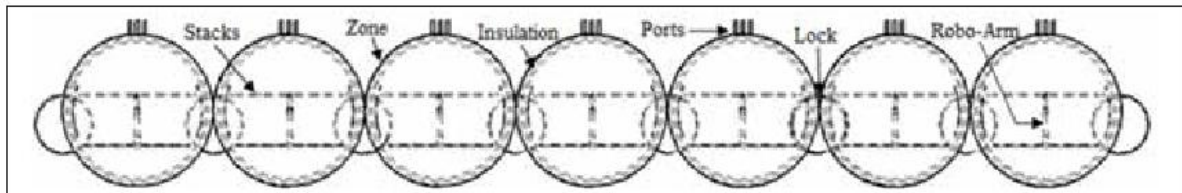Fig. 2: Top View of Cylindrical Zones in Series with One Lock adjoining Two Zones

Fig. 3: Front View of Cylindrical Zones in Series with One Lock adjoining Two Zones
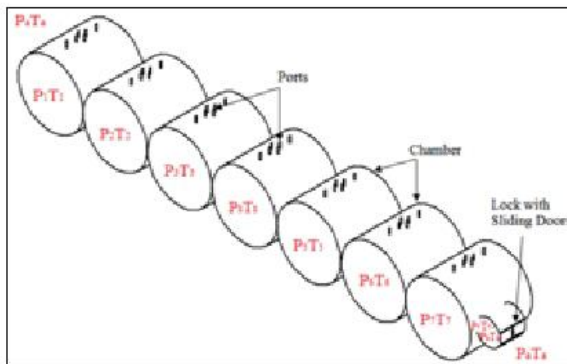

Fig. 4: Isometric View of Cylindrical Zones in
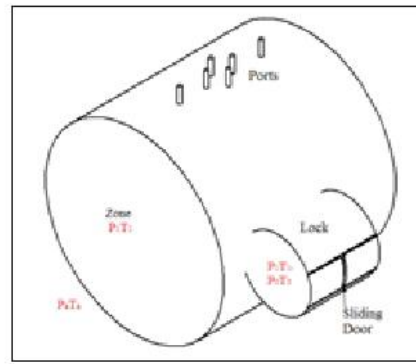Series with a Lock adjoining 2 Zones

Fig. 5: Isometric View of a Cylindrical Zone with a
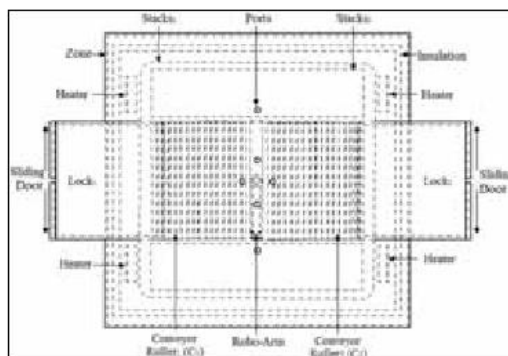Lock on either side

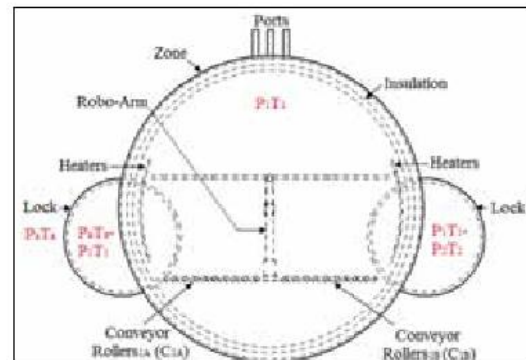Fig. 6: Top View of Single Cylindrical Zone with a
Lock on either side

Fig. 7: Front View of Single Cylindrical Zone with
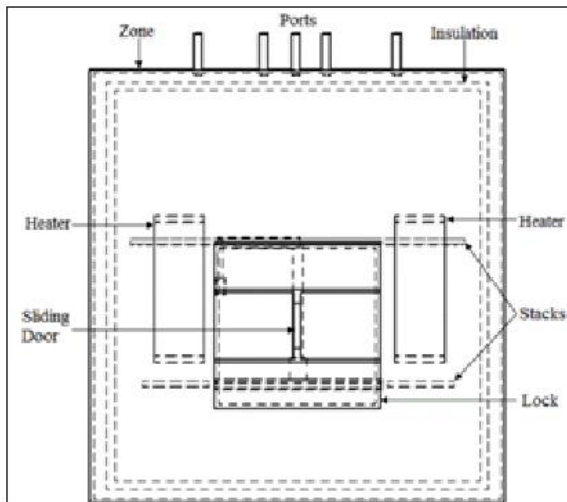a Lock on either side

*Fig. 8: Right View of a Cylindrical Zone with a
Lock on either side (in forefront)*

A series of cylinders (Figs. 2 to 4) interconnected with interspersing locks can provide a means of achieving Continuous HIPing. Fig. 5 provides an Isometric of a single cylinder. In this configuration, the storage is provided within each zone as stacks, with provision for robo-arm (Figs. 6 to 8). The heaters and insulation are arranged within each zone and ports may be clubbed together in one central port or separated as allowed by stress considerations. The parts enter through one end of the series of pressure vessels and progressively go through increasing stages of temperature and pressure within each zone, before reaching the target temperature and pressure in the soak zone at the central cylinder. Then these parts are passed through the subsequent zones with consecutively decreasing temperature and pressure after soaking for required duration in the central cylinder and by the time of ejection through the opposite (exit) side they reach ambient temperature and pressure. Of course the ambient temperature and pressure (entrance side and exit side) can be higher than room temperature and atmospheric pressure if the material system sees no degradation for those conditions. The stacking and part handling can be done by robo-arm within each zone. The robo-arm is at the center of each zone with a feed conveyor and relay conveyor before and after robo-arm base situated at the center. Robo arm is further explained in a subsequent section.

V. Design Configuration - 2 Cylindrical - Double Conveyor - without Robo-Arm or Storage Stacks

In the case where a robo-arm is considered not feasible due to the severe operating conditions or not adaptable due to the increased installation costs or operational difficulties, it is essential to provide more space to facilitate zone-soak by use of double conveyors, which may be independently operated. Figs. 9 to 11 show the series of cylinders interconnected by locks, while Fig. 12 is that of a single cylinder. Figs. 13 to 15 provide detailed views of the twin parallel conveyors within each zone that serve the dual purpose of material movement and soak-storage. Unlike in previous configuration with two discrete conveyors, one before and one after robo-arm assembly within each zone, here, the conveyors are continuous within each zone as there is no robo-arm assembly at the center of conveyor. However, in this configuration two such parallel conveyors are there within each zone to provide operational flexibility besides soak-storage space in lieu of storage stacks with robo-arm handling the parts in the previous configuration. For any of the proposed configurations, the sliding doors placed on the interconnecting locks open to enable entry, exit or transfer of parts between zones. The smaller size/volume of the locks (compared to the zones) also allow easy, economical and fast ramp up/down cycles of temperature and pressure. The equalization of temperature and pressure within the lock with the temperature or pressure of either the succeeding/preceding zone just before opening of the lock doors, allows such process to easily enable the handling, transfer or movement of the parts from one zone to another zone without any load differentials on the doors either to open/close.

a   ambient conditions/zone

s   soak conditions/zone

T_i, P_i Temperature and Pressure (i = a, 1, 2, 3, S, 5, 6, 7, a)

Cir Conveyor Roller (i = 1, 2, 3, S, 5, 6, 7) and (r = F or R) (F = Front; R = Rear)

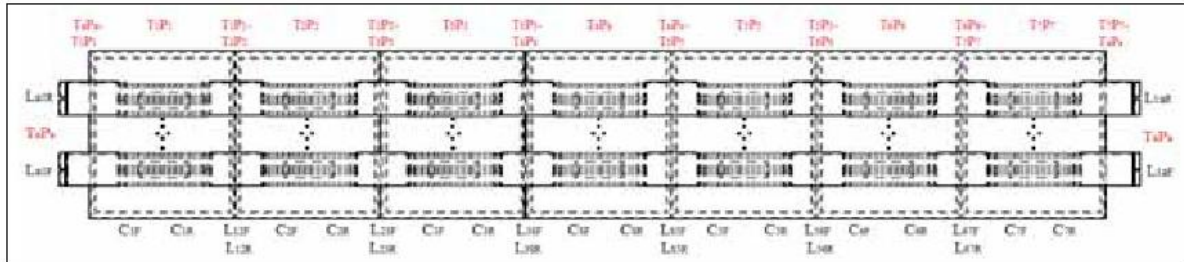Lxyz Lock b/w Zone x and Zone y (x, y = a, 1, 2, 3, S, 5, 6, 7,a) (z = F or R)

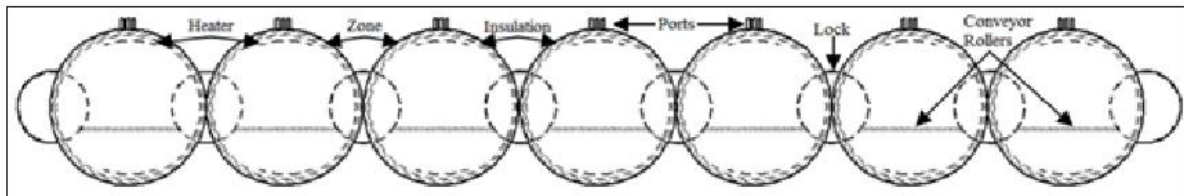*Fig. 9: Top View of Cylindrical Zones in Series with Two Locks adjoining Two Zones*

Fig. 10: Front View of Cylindrical Zones in Series with Two Locks adjoining Two Zones
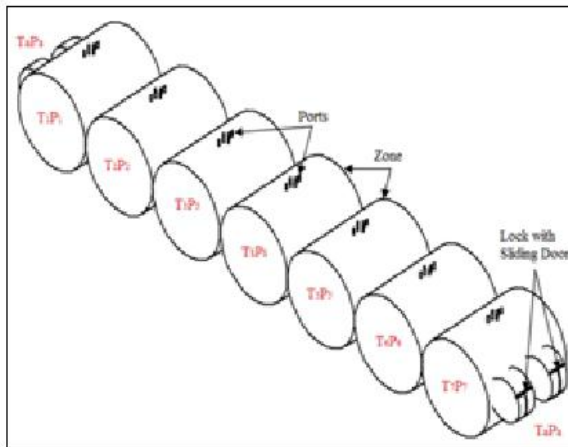

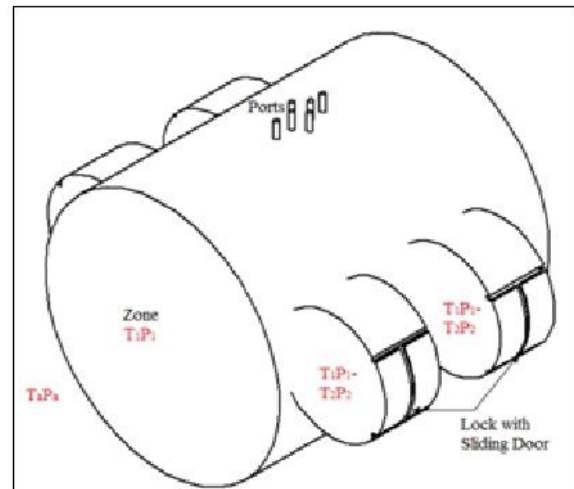*Fig. 11: Isometric View of Cylindrical Zones in Series with two Locks on either side*

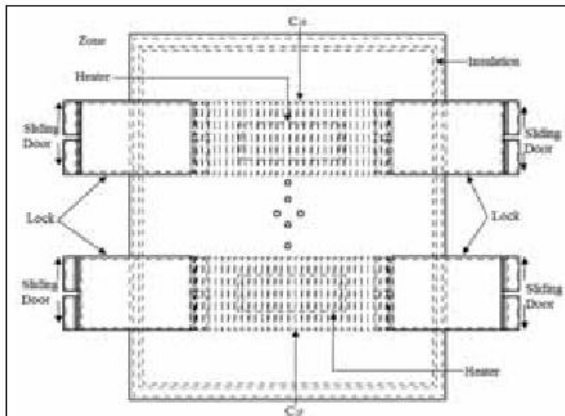*Fig.12: Isometric View of a Cylindrical Zone with adjoining Two Locks on sides*

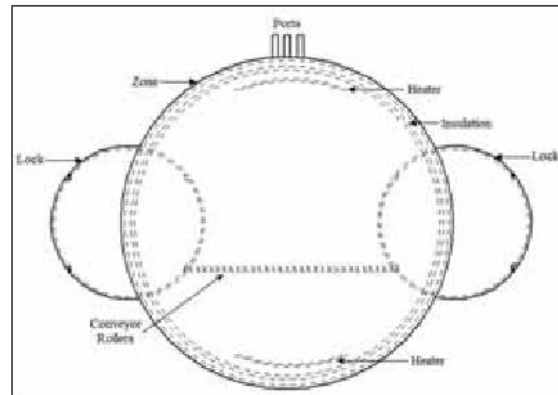*Fig. 13: Top View of Single Cylindrical Zone with Two Locks on each side*

Fig. 14: Front View of Single Cylindrical Zone with Two Locks on each side

VI. Design Configuration - 3 Cuboid - Single Conveyor - with Robo-Arm for Storage Stacks

If a box-shaped configuration is preferred, a cuboid-shape may substitute for the cylindrical pressure vessels. However, as a preliminary consideration, the cuboid shapes may not be preferable over the cylindrical shapes due to stress concentrations at corners. The rigorous analyses of suitable

Z_i Zone (i = 1, 2, 3, S, 5, 6, 7)

T_i, P_i Temperature and Pressure (i = a, 1, 2, 3, S, 5, 6, 7, a)

C_{ir} Conveyor Roller (i = 1, 2, 3, S, 5, 6, 7) and (r = A or B)

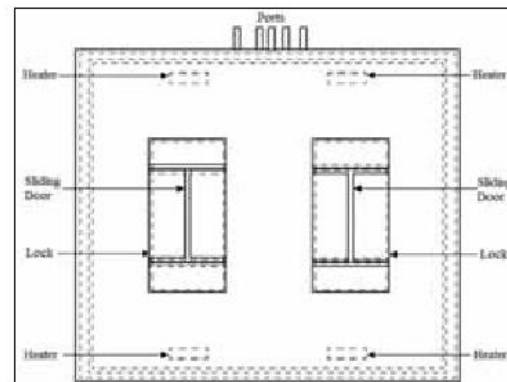L_{xy} Lock b/w Zone x and Zone y (x, y = a, 1, 2, 3, S, 5, 6, 7, a)

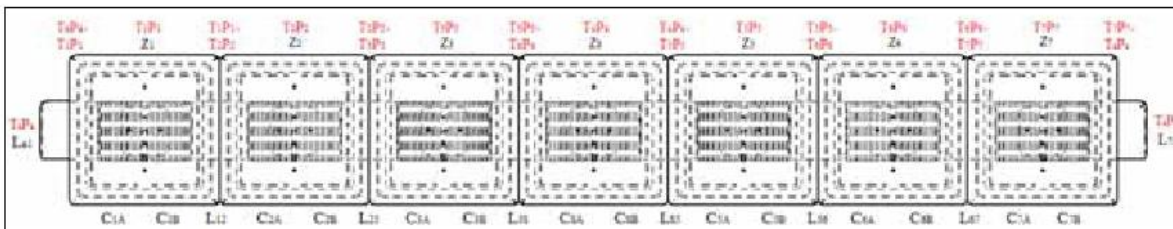*Fig. 15: Right View of a Cylindrical Zone with Two Locks on each side (in forefront)*

Fig. 16: Top View of Cuboid Zones in Series with One Lock adjoining Two Zones
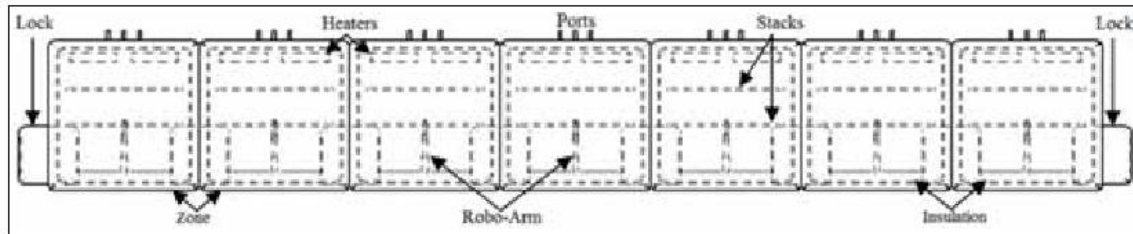
Fig. 17: Front View of Cuboid Zones in Series with One Lock adjoining Two Zones
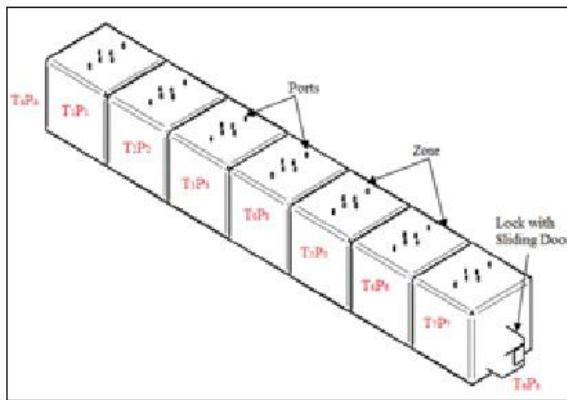
Fig. 18: Isometric View of Cuboid Zones in Series with a Lock adjoining 2 Zones
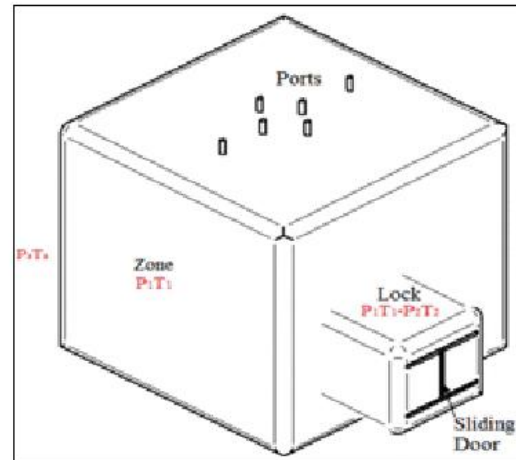
Fig.19: Isometric View of a Cuboid Zone with a Lock on either side
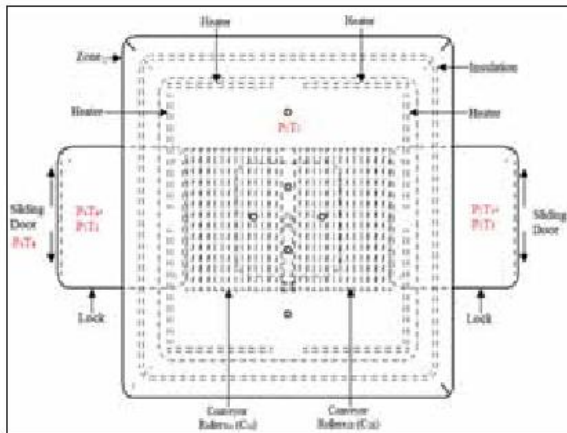
Fig. 20: Top View of Single Cuboid Zone with a Lock on either side

configurations, which could form the next step in the development of a Continuous HIPing process can help decide which type of configuration is suitable considering all relevant factors of design, fabrication and material performance at the expected operating conditions of the equipment. As earlier discussed in the first two configurations, **Figs. 16 to 18** provide different views for a series of cuboid pressure vessels and **Figs. 19 to 22** provide detailed views of an individual pressure vessel.

Robo-arm Assembly in this configuration is explained further in the next section. All the three configurations suggested so far consider 7 zones, with 6 intermittent locks and one entry lock and one exit lock. The exact number of zones and locks may also depend upon the final designer, while taking into account the temperature and pressure limits
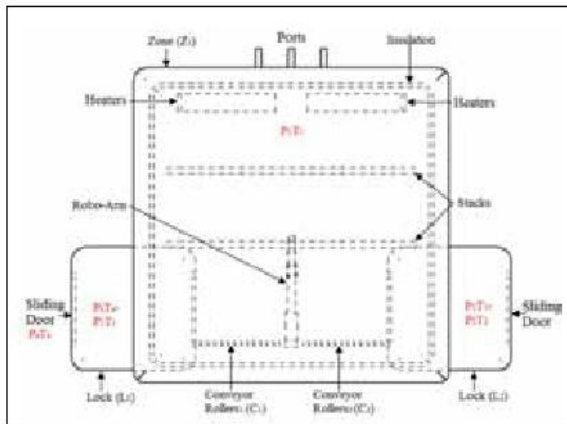
Fig. 21: Front View of Single Cuboid Zone with a Lock on either side
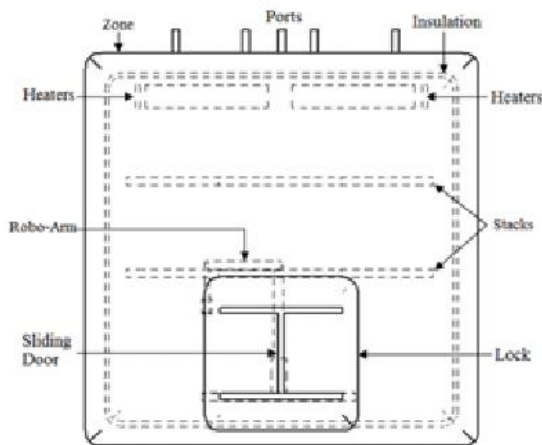
Fig. 22: Right View of a Cuboid Zone with Lock on either side (1 in forefront)

of the soak zone, needed ramp-up and ramp-down cycles and the time ranges needed for the entire HIP cycle for different kinds of materials.

VII. Design of Robo-arm Assembly

A suitably designed robo-arm (Figs. 23 to 25) may be developed by taking into consideration the final designs of zones (pressure vessels), locks, conveyors and stacks that can be accommodated within zones. As to the electronics/ mechanics of robo-arm, the nuclear and under-sea exploration industries could

give pointers on existing robo-arms for extreme operating conditions of temperature and pressure.
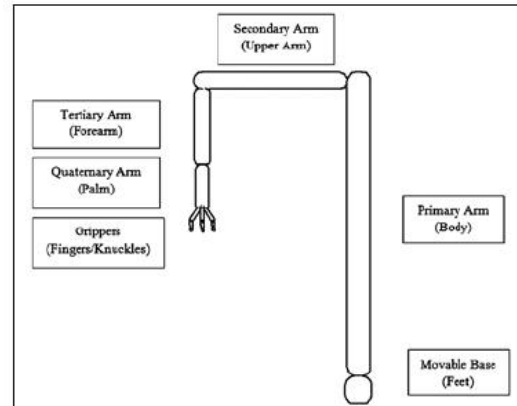
Fig. 23: Side View of Robo Arm
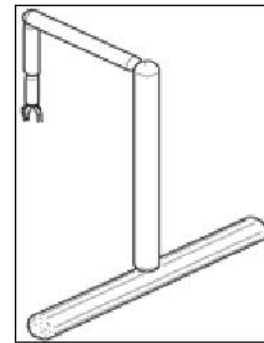
Fig. 24: Isometric View of Robo Arm

Fig. 25: 3D-view of Gripper

VIII. Suggestions for Further Work

Continuous HIPing complicates the process of modeling the effects of simultaneous application of temperature and pressure even further due to the added feature of continuous movement of parts to be HIPed through Zones and Locks and the need for feedback and control loops about temperature and pressure due to their minor fluctuations while opening and closing of the locks to facilitate the material movement between zones. Continuous HIPing as a process would require dedicated teams consisting of design engineers, materials engineers, electronic engineers, high pressure physicists, mathematical and physical modeling and CFD experts (to understand the very dynamic and simultaneous influences of temperature, pressure, time and spatial movement) and computer visualization experts (for precise positioning during stacking by robo-arm and movement of parts by differential conveyor systems). Although developing Continuous-HIP may appear to be much effort, the successful outcome could dramatically further boost the appeal of HIPing as a bulk manufacturing process for near-net shape products of all materials and for all kinds of applications. It has been estimated recently that 1000 HIP systems have been installed [13] since 1970. With projected growth of PM industry, which is presently fueled by Automobile sector, other Sectors such as [6] Oil and Gas production, Power Generation are also presently significantly purchasing HIP PM products. Hence the design and development costs for this continuous process of HIPing can be justified for any established HIP manufacturer.

IX. Conclusions

Essentially Continuous HIPing (or C-HIPing), for most part, converts the temporal scale of a Batch HIPing (with one pressure vessel) into the spatial scale of Continuous HIPing (with a series of pressure vessels) with consequent savings in time and costs. As can be easily understood from proposed configurations, this approach bestows continuous nature to the process of HIPing while reducing the time-line with potential to make the process very cost effective for other engineering components as well. Other benefits of Continuous HIPing would include higher productivity and easier adaptability for other routine engineering components. However, this process requires much computer-based visualization, automation for material handling, maintenance-free compatible design and higher installation costs. The safety aspects would also require careful scrutiny due to even more complex operations than in Batch HIPing process.

References

1. Y.V.S. Kumar, "Hot Isostatic Pressing for Near-Net or Net Shape Processing of Advanced Materials - an Overview," In: Proc. of IV Asian Powder Technology Symp. Innovations in Particle Technology - APT-2009, Sep 14-16, New Delhi, Indian Inst. of Metals, Indian Inst. of Mineral Engineers and TCS, Paper No. 141, 603-609, (2009).

2. Y.V.S. Kumar, "Hot Isostatic Pressing for Near-Net or Net Shape Components for Automotive and Engineering Industry," In: Proc of Intl. Conf. & Exhibition on Powder Metallurgy for Automotive and Engineering Industries: Cost Effective Solutions through PM - PM-11, Feb 3-5, Pune, Powder Metallurgy Association of India, (2011).

3. Y.V.S. Kumar, "Causes for and Containment of Porosity Development in Compacts upon Hot Isostatic Pressing," In: Intl. Conf. on P/M for Automotive and Engineering Industries- Precision and Additive Manufacturing - PM-13, Feb 7-9, Pune, Powder Metallurgy Association of India, (2013).

4. Y.V.S. Kumar, "Isostatic Pressing for Bulk Net Shape Processing of Silicides and SEM for Analysis of Non-Densification and their Thermal Unstability," Transactions of Powder Metallurgy Association of India, Vol. 36, 111-116, (2010).

5. Y.V.S. Kumar, "Adapting Hot Isostatic Pressing into a Continuous Process for Industrial Use – Design Conceptualization," Transactions of Powder Metallurgy Association of India, Vol. 36, 121-126, (2010).

6. S.J. Mashl, "Hot Isostatic Pressing (HIP) of Large PM Products: An Industry poised for Growth," Powder Metallurgy Review, Vol. 2, No. 2, 31-39, (2013).

7. Avure, "Some Thing Big is Here: TeraPi – Animation", Avure Technologies, http://info.avure.com/l/8012/2012-10-02/36h6r6 (viewed, Jul 16, 2013).

8. A. Eklund and M. Gärdin, private communications, Avure Technologies, Sweden, Feb 27-Mar 6, (2013).

9. J.F. Blumrich, "Design," Science, Vol. 168, 1551-1554, (1970).

10. National Research Council, "Improving Engineering Design," National Academy Press, (1991).

11. G.E. Dieter and L.C. Schmidt, "Engineering Design," 4th Ed, Intl. Ed., McGraw Hill, (2009).

12. I.M. Asimow, "Introduction to Design," Prentice-Hall, (1962).

13. IPMD Inovar Communications Ltd., "Recent Trends in Host Isostatic Pressing (HIP) Technology: Part 1, Equipment," Jun 6, (2012). http://www.ipmd.net/articles/001746.html (viewed, Jul 16, 2013).

A COMPARATIVE STUDY OF NANO-SIZE REINFORCEMENT ON PEAK BROADENING ANALYSIS OF Al 6061 ALLOY NANOCOMPOSITE

D. Jeyasimman[1], R. Ponalagusamy[2], R. Narayanasamy[1], R. S. Kambali[3], Vijayakumar Iyer[3]

[1]Department of Production Engineering, National Institute of Technology, Tiruchirappalli, India.
[2]Department of Mathematics, National Institute of Technology, Tiruchirappalli, India.
[3]Powder Metallurgy Shop, Heavy Alloy Penetrator Project, Tiruchirappalli, India.

Abstract: In the present study, mechanical alloying was successfully employed to synthesis nano-crystalline Al 6061 alloy powders reinforced with 2 wt.% TiC and 2 wt.% Al$_2$O$_3$ at nano level. The crystallite size of Al 6061 matrix powder was affected by the addition of various nano reinforcements. Using Williamson-Hall analysis, the crystallite size and lattice strain of various aluminum composite powders were investigated with broadening of X-ray diffraction (XRD) peaks. Lattice parameters of nanocomposite powders were estimated by using XRD. The effect of reinforcement and milling time on nanocomposite were also studied. XRD results showed that the crystallite size of aluminum reached 68 and 57 nm respectively, after 30 h of milling in the case of Al 6061+2 wt .% TiC and Al 6061+2 wt .% Al$_2$O$_3$ nanocomposite powders with uniform particle size distribution.

Keywords: Mechanical alloying; Characterization; X-ray diffraction

1. Introduction

Aluminum metal matrix composites (AMCs) are attractive for structural, automotive and aerospace applications due to their light weight and moderate specific strength [1-2]. Recently, the interest to increase aluminum strength for applications in the aerospace and aeronautic industries has motivated the study of aluminum matrix composites (AMCs), which can exhibit better mechanical properties at medium and room temperatures. Most of the aluminum alloys possesses the density of 2698 kg/m^3 which is near that of pure aluminum. The melting point of pure aluminum is 660°C which is relatively low melting temperature compared to other potential matrix metals. These characteristics facilitate on processing of Al-based MMCs by solid state routes, such as powder metallurgy, and also by casting methods [3]. Around 20% of aircraft components are being manufactured by Al-based MMCs [4]. Among all the aluminum alloys, Al 6061 posses excellent formability in addition to high strength and good corrosion resistance[5]. Various

solid state and liquid state processing methods have been attempted and discussed to synthesize nano alumina reinforced AMCs. One of the important advantages of solid state processing methods to produce nanocomposites is that it is possible to introduce a high volume fraction of reinforcement and still achieve a uniform distribution [6].

Powder Metallurgy (PM) is one of the common and versatile processes used in the fabrication of Aluminum metal matrix composites by mixing the metallic matrix powder and reinforcements followed by compaction and high temperature consolidation. Mechanical alloying (MA) is a solid state powder processing that allows production of homogeneous materials starting from blended elemental powder mixtures. The high-energy ball milling process generally involves repeated cold-welding, fracturing and re-welding of powder mixtures in a planetary ball mill [7]. This is now known as mechanical alloying or mechanical milling. The process in which mixtures of powders are milled together is denoted by mechanical alloying (MA); it involves material

transfer to obtain a homogeneous alloy by repeated deformation /welding /fracture mechanisms. Mechanical alloying leads to uniform distribution of the reinforcement as well as inducing a significant reduction in crystallite size and increase in lattice strain. The most common reinforcements for aluminum are SiC, TiO_2, TiC, B_4C, AIN, Al_2O_3 and CNTs. Addition of ceramic reinforcements such as SiC, Al_2O_3, TiC, B_4C and ZrO_2 to metal matrix improves hardness and thermal shock resistance [8]. Al-TiC composites combine the ductility and toughness of the aluminum matrix with the strength, stiffness, hardness and wear resistance of the TiC particles and are attractive candidates for structural applications, especially in the automotive sector. Among all ceramics, alumina has high hardness, compressive strength, wear resistance, thermal and chemical stability and high elastic modulus [9]. Al-Al_2O_3 composites have a high potential for very specific applications such as aerospace and military weaponry [6]. Thus, we used nano level TiC and nano level alumina as reinforcements due to high availability, low cost and over all good properties.

The main aim of this work is to investigate the effect of the above two reinforcements and milling time on crystallite size, lattice strain and lattice parameter in Al 6061 matrix.

2. Experimental work

2.1. Materials

Aluminum alloy 6061 was produced by blending the entire high pure elemental powders with composition as per table 1. The pure aluminum powder of average particle size of less than 45 μm as a major matrix material and other pure elemental powders such as silicon, iron, copper, manganese, chromium, zinc and titanium as remaining matrix materials supplied by Alfa Aesar, USA were used. The chemical composition and mesh size of the pure elemental powders used in this study is shown in Table 1.

The reinforcements were used as follows:

❖ Titanium Carbide of 95% purity, <200 nm particle size supplied from Sigma Aldrich, China.

❖ The gamma phase nano size alumina of purity 99.5% with an average particle size 40-50 nm APS powder supplied by Alfa Aesar, USA.

2.2. Synthesis of composite powder

The elemental powders required to make Al 6061 were blended in a two station (Insmart Systems, Hyderabad, India) planetary ball mill, at 280 rpm for 2 h. No grinding media and process control agents were used during the blending process. The blended powders were regarded as the 0 h mechanically milled powders. The nano size TiC and nano size alumina were added initially with 0 h mechanically milled powders in the same planetary mill. The milling was performed under high pure wet agent (Toluene) to avoid the formation of intermetallic compounds during milling as reported in the earlier works [10]. Highly hardened nine steel balls of 20 mm diameter of each 33.5 g mass (totally 301.5 g) together with 30 g mass of Al 6061, 2 wt% reinforcement powder mixture and toluene ($C_6H_5CH_3$ supplied by Ranbaxy, India) were sealed in a hardened stainless steel vial. The ball to powder (BPR) ratio was approximately 10:1. The plate speed of mill was set to 100 rpm and the corresponding bowl/ vial speed was 280 rpm. The MA processing time was 30 h: however, in order to avoid significant temperature rise, 20 minutes of milling was alternated with 20 minutes of cooling. The milled powders were taken out at regular intervals of time 1, 5, 10, 20 and 30 h for crystal structural analysis.

Name of Elements	Silicon Si	Iron Fe	Copper Cu	Manganese Mn	Magnesium Mg	Chromium Cr	Zinc Zn	Titanium Ti	Aluminum Al
Element concentration (gravimetric, wt. %)	0.600	0.700	0.275	0.150	1.000	0.195	0.250	0.150	Bal

*All powders are more than 99 % purity and mesh size of -325.

Table 1 Chemical composition to make the Al 6061 alloy powder.

2.3. Powder Characterization

X-ray diffraction analysis was carried out to determine the crystallite size and lattice strain of the milled powder samples on D/Max Ultima III; XRD machine (Rigaku Corporation, Japan). The samples were exposed continuously to Cu Kα radiation (λ=1.5406 A^0) at a scanning speed 2^0 per min operating at 30 mA and 40 KV. It's scanning range of 20^0-80^0 in steps of 0.02. Crystallite size and micro strain were determined using the standard Williamson-Hall analysis [11].

$$\beta_{hkl}.\cos\theta_{hkl} = \left[\frac{k\lambda}{t}\right] + 4\varepsilon.\sin\theta_{hkl} \qquad (1)$$

Where k is the shape factor (0.9), λ is the wavelength of X-ray (1.5406), θ_{hkl} is the Bragg angle and t is the crystallite size normal to the reflecting planes and ε is the lattice strain. The instrumental broadening corrected line profile breadth, β_{hkl} as a full width at half maximum (FWHM) were calculated based on each reflection of 2θ. The first four Al reflections (1 1 1), (2 0 0), (2 2 1) and (3 1 1) were used to construct a linear plot of β_{hkl} cos θ_{hkl} against 4 sin θ_{hkl}. Crystallite size (t) was obtained from the intercept c (i.e. c= kλ/t) and the strain (ε) from the slope (i.e. m=ε).

The actual lattice parameter was determined for each of the Al diffraction planes (1 1 1), (2 0 0), (2 2 0) and (3 1 1) from XRD patterns. The actual lattice parameter was obtained from the intercept [11], by constructing a linear plot between the calculated lattice parameter for each Bragg's angle and the corresponding value of $\cos^2\theta/\sin\theta$. The value of lattice parameter depends on the level of atomic diffusivity.

3. Results and discussion

3.1. XRD analyses

The XRD patterns of the as received powders such as pure aluminum, pure titanium carbide and pure alumina powders are shown in Fig. 1(a)-(c). All the major peaks (1 1 1), (2 0 0), (2 2 0) and (3 1 1) of

aluminum were identified as belonging to Al with the FCC crystal structure and a lattice parameter of a=0.40504 nm. All the five peaks (111), (200), (220), (311) and (221) of TiC were identified as belonging to TiC with the lattice parameter a=0.4329 nm. The XRD pattern from the 50 nm alumina particle size powder was identified with three peaks (1 1 0), (1 1 1) and (2 1 1) as belonging to alumina with the lattice parameter a= 0.3923 nm. The diffraction peaks are broad due to small particle size.

Fig. 2 (a)-(b) shows XRD patterns of Al 6061-2 wt.% TiC and Al 6061-2 wt. % Al$_2$O$_3$ nanocomposite powders after 0, 1, 5, 10, 20 and 30 h of MA. Fig. 2 (a)-(b) shows that the peaks of aluminum for the (1 1 1), (2 0 0) and (2 2 0) planes identified the Al 6061-x wt. % TiC and Al 6061-2 wt.% Al$_2$O$_3$ nanocomposite. Peaks for Si, Mg, Fe, Cu and Mn, which are related to Al 6061 alloy, were not detectable due to their low volume fraction [12]. These components were expected to dissolve in the Al lattice. Some peaks of nano level titanium carbide were observed. However, alumina peaks could not be identified. It is reported that, the Al$_2$O$_3$ particles formed during milling are very small in size about 25 nm and exhibit amorphous structure [13-14]. However, once amorphous alumina is formed, if the strong Al-O band will suppress the atomic mobility necessary for rearrangement of the atomic structure. Then alumina remains amorphous and the peaks of this phase cannot be identified in the XRD patterns [15]. This result is in good agreement with those reported by Tavoosi et al. [15] and Sivasankaran et al [16]. Table.2 shows grain size and lattice strain of powders after 5, 10, 20 and 30 h of milling.

Powder	Grain size in nm Milled Powder (h)						Lattice Strain in % Milled Powder (h)					
	0	1	5	10	20	30	0	1	5	10	20	30
Al 6061-2 wt. % TiC nanocomposite	310	195	144	105	87	68	0.025	0.06	0.09	0.152	0.176	0.224
Al 6061-2 wt. % Al$_2$O$_3$ nanocomposite	245	210	167	91	63	57	0.05	0.09	0.104	0.124	0.167	0.186

Table .2. Grain size and lattice strain of powders after 0, 1, 5, 10, 20 and 30 h of milling.

Fig.2. XRD patterns of (a) Al 6061-2 wt. % TiC nanocomposite powders after 0, 1, 5, 10, 20 and 30 h of MA. (b) Al 6061-2 wt. % Al$_2$O$_3$ nanocomposite powders after 0, 1, 5, 10, 20 and 30 h of MA.

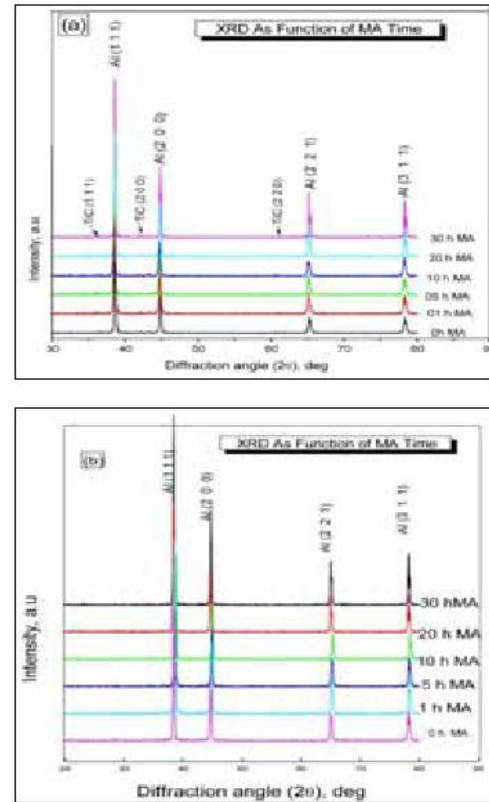**Fig.1. XRD pattern of as received pure Powders (a) Al (b) TiC (c) Al$_2$O$_3$**

Fig. 3 (a)-(b) shows FWHM intensity of four diffraction planes as a function of milling time for Al 6061-2 wt.% TiC and Al 6061-2 wt.% Al$_2$O$_3$. For the above two cases, FWHM value increased with increase in milling time. For (1 1 1) and (2 0 0) planes TiC reinforced Al 6061 nanocomposite had low values compared with Al$_2$O$_3$ reinforced Al 6061 nanocomposite. However, after 30 h of MA (2 2 0) and (3 1 1) planes had almost same value for TiC and Al$_2$O$_3$ reinforced Al 6061 nanocomposites. As the milling time increased, significant reduction in peak height and increase in width was observed as explained by earlier researchers [7, 17-18] and this may be described to a severe lattice distortion and grain size refinement.

Fig.3. Full width at half maximum intensity of four diffraction planes as a function of milling time: (a) Al 6061-2 wt. % TiC (b) Al 6061-2 wt. % Al₂O₃.

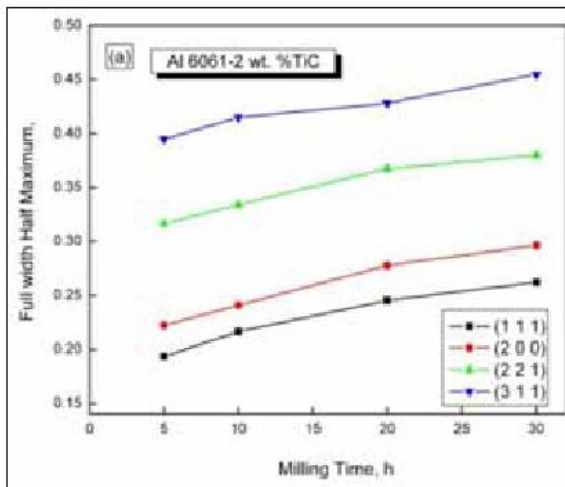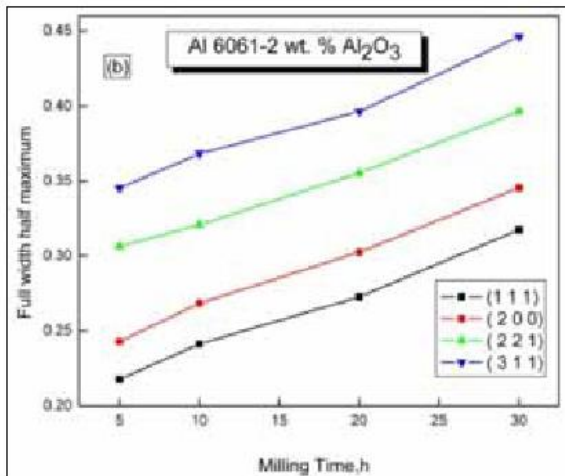*Fig.3.(Contd.) Full width at half maximum intensity of four diffraction planes as a function of milling time: (a) Al 6061-2 wt. % TiC (b) Al 6061-2 wt. % Al₂O₃.*

Fig.4 (a) shows the crystallite size decreased significantly from around 310 nm to 68 nm and lattice strain was increased from 0.032 % to 0.224 % with increase in milling time 0 to 30 h. The crystallite size began to steadily decrease up to a

processing time of 10 h. Further processing (up to 30 h of MA) slightly decreased the crystallite size. Conversely, the lattice strain remarkably increased up to 10 h and continued to slightly increase thereafter. The slight decrease in the crystallite size and slight increase in the lattice strain indicated the attainment of steady state milling at 30 h. From Fig. 4(b), it appears that the reduction of crystallite size had occurred from initial stages and the refining effect weakened when the milling time was longer than 20 h. Further processing (up to 30 h of MA) slightly decreased the crystallite size. The initial crystallite size was about 250 nm and after 30 h, it reduced to about 50 nm. However, the lattice strain remarkably increased up to 30 h. The lattice strain increase with milling time was due to distortion effect caused by dislocation in the lattice [15].
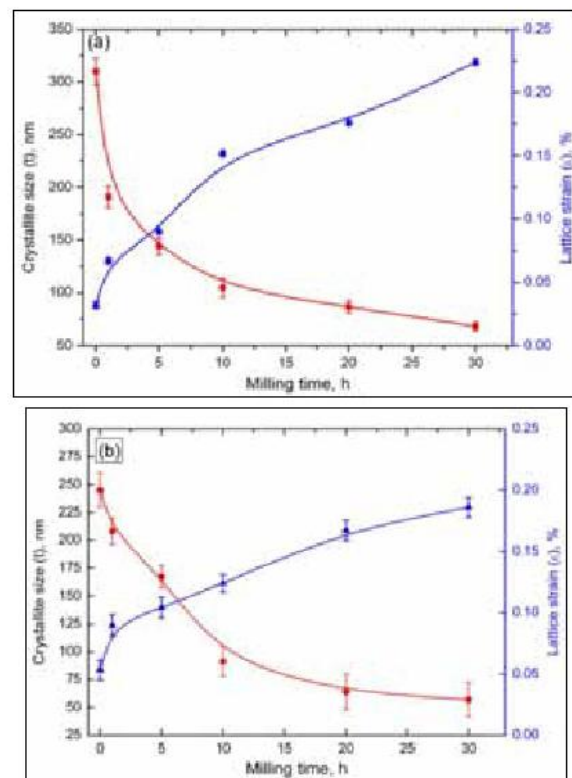

Fig.4. Variation in crystallite size and lattice strain with milling time (a) Al 6061-2 wt. % TiC (b) Al 6061-2 wt. % Al₂O₃

The lattice parameter reported for the pure FCC-Al at room temperature was 4.0496 Å [19]. The lattice parameter reported for Al 6061 nanocrystalline was 4.0473 Å for milling 40 h [10]. In this investigation, the lattice parameter for Pure Al was 4.0504 Å and also Al 6061 nanocrystalline without reinforcement was 4.0485 Å for 30 h of MA. Lattice parameter had decreased from 0.40485 nm to 0.40475 nm with increase in milling time from 0 h to 30 h for the 2 wt.% nano TiC addition as shown in Fig. 5(a). From the Figure, it is clear that the lattice parameter began to decrease as the function of milling time from 0 h to 30 h. The lattice parameter had decreased from 0.40492 nm to 0.40455 nm with increase in milling time from 0 h to 30 h for the 2 wt.% nano Al_2O_3 as shown in Fig. 5 (b). This effect was expected due to the dissolution of other minor alloying elements related to Al 6061 and the milling agent [16].
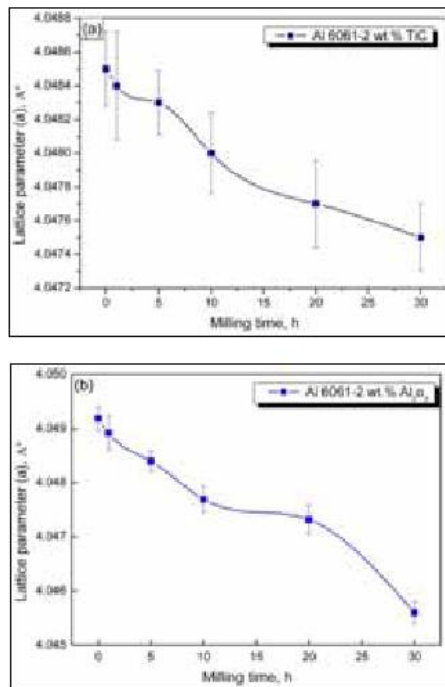

Fig.5. Lattice parameter variations with milling time (a) Al 6061-2 wt. % TiC (b) Al 6061 -2 wt. % Al_2O_3

4. Conclusion.

The present study examined the synthesis, structural evolution, characterization and mechanical behavior of Al 6061-2 wt. % TiC and Al 6061-2 wt. % Al_2O_3 nanocomposite powders prepared by MA.

The following conclusions were obtained during this study.

❖ The bulk nanocrystalline Al 6061 matrix reinforced with 2 weight percentage of nano TiC and alumina particles of nanocomposites were successfully produced by MA.

❖ The crystallite size of nanocomposite powders with function of milling time were investigated and reported. It was found that the addition of hard ceramic particles of nano TiC and nano Al_2O_3 influenced more on the matrix powder crystallite size.

❖ Around 68 and 57 nm of matrix crystallite size was achieved after 30 h MA for Al 6061-2.0 wt. % TiC and Al 6061-2 wt. % Al_2O_3 nanocomposites.

❖ The lattice strains induced in the powders had increased with increasing milling time.

❖ The lattice parameter had also decreased with increasing milling time for Al 6061-2 wt. % TiC and Al 6061-2 wt. % Al_2O_3 nanocomposite powders.

References

1. T.W. Clyne and P.J.Withers, An Introduction to metal matrix composites, Cambridge. UK.(1995).

2. T.Graziani, A.Bellosi and D.D.Fabbriche. "Effect of some iron-group metals on densification and characteristics of TiB$_2$". Int.J.Refer.Met.Hard. Mater. Vol 11, 105-112 (1992)

3. Composite materials hand book. Metal Matrix composites, Department of Defense, USA, MIL-HDBK-17-4A, 2002:4:44-61.

3. Serope Kalpakjian and Steven R.Schmid. Manufacturing Engineering and Technology, Fourth Edition, Pearson Education, Singapore (2005).

4. C.S. Ramesh, A.R.Anuar Khan, N.Ravikumar and P.Savanprabu. "Prediction of wear coefficient of Al 6061-TiO$_2$ composites". Wear Vol 259, 602-608 (2005).

5. C.Suryanarayana, Nasser Al-Aqeeli. "Mechanically alloyed nanocomposites". Progress in Materials Science Vol.58, 383-502. (2013).

6. C. Suryanarayana. "Mechanical alloying and milling". Progress in Mater Science Vol.46, 1-184 (2001)

7. M.A.piggott, Load bearing fiber composites, Pergamon press.London.(1980).

8. J.K.Wessel, The hand book of advanced materials, John Wiley & Sons. New York.(2004).

9. S.Sivasankaran, K.Sivaprasad, R.Narayanasamy and Vijay Kumar Iyer. "Journal of alloys and compounds", Vol. 491, 712-721, (2010)

10. G.K.Williamson and W.H.Hall. "X-ray line broadening from field aluminium and wolfram", Acta Metall. Vol. 1(1), 22-31, (1953).

11. B.D.Cullity. Elements of X-ray diffraction. 2nd edition Addision-Wesley (1978)

12. J.M.Wu, "Nano-Sized amorphous alumina particles obtained by ball milling ZnO and Al powder mixture", Materials Letters, Vol 48, 324-330, (2001)

13. M.Uma Devi. "New phase formation in Al$_2$O$_3$-based thermal spray coatings", Ceramics International Vol. 30, 555-565 (2004).

14. M.Tavoosi, E.Karimzadeh and M.H.Enayati, "Fabrication of Al-Zn /α-Al$_2$O$_3$ nanocomposite by mechanical alloying", Materials letters Vol. 62, 282-285 (2008).

15. S.Sivasankaran, K.Sivaprasad, R.Narayanasamy and P.V.Satyanarayana, "X-Ray peak broadening analysis of AA 6061100-x –x wt. % Al$_2$O$_3$ nanocomposite produced by mechanical alloying", Materials Characterization, Vol. 62, 661-672 (2011)

16. Viseslava Rajkovic, Dusan Bozic and Milan T.Jovanovic. "Properties of copper matrix reinforced with nano- and micro- sized Al$_2$O$_3$ particles", Journal of Alloys and Compounds, Vol. 459, 177-184 (2008)

17. Hafeez Ahamed and V.Senthilkumar, "Role of nano-size reinforcement and milling on the synthesis of nano-crystalline aluminum alloy composites by mechanical alloying", Journal of Alloys and Compounds, Vol. 505, 772-782 (2010)

18. V.A.Lubarda, "On the effective lattice parameter of binary alloys", Mech Mater Vol. 35, 53-68 (2003)

DEVELOPMENT OF IMPREGNATED AGGLOMERATE PELLETIZATION (IAP) PROCESS FOR FABRICATION OF (Th,U)O$_2$ MIXED OXIDE PELLETS

P.M. Khot, Y.G. Nehete, B.K. Shelke, S.K. Shotriya, K.Subbarayal, Neeraj Kumar, B.Surendra, M.K. Yadav, A.K. Mishra, P.G. Behere, Mohd Afzal

Advanced Fuel Fabrication Facility, Bhabha Atomic Research Centre, Tarapur, India.

Abstract: Impregnated Agglomerate Pelletization (IAP) technique has been developed at Advanced Fuel Fabrication Facility (AFFF), BARC, Tarapur, for manufacturing (Th, ^{233}U)O$_2$ mixed oxide fuel pellets, which are remotely fabricated in hot cell or shielded glove box facilities to reduce man-rem problem associated with ^{232}U daughter radionuclides. This technique is being investigated to fabricate the fuel for Indian Advanced Heavy Water Reactor (AHWR). In the IAP process, ThO$_2$ is converted to free flowing spheroids by powder extrusion route in an unshielded facility which are then coated with uranyl nitrate solution in a shielded facility. The dried coated agglomerate is finally compacted and then sintered in oxidizing/reducing atmosphere to obtain high density (Th,U)O$_2$ pellets. In this study, fabrication of (Th, 3%U)O$_2$ mixed oxide pellets was carried out by IAP process. The main motive for developing the present IAP process was to further reduce powder-handling, man-rem and improve the homogeneity of fuel pellets.

The pellets obtained were characterized using alpha autoradiography. The results obtained were compared with the results for the pellets fabricated by other routes such as Coated Agglomerate Pelletization (CAP) and Powder Oxide Pelletization (POP) route.

Keywords: IAP, CAP, (Th,U)O$_2$ MOX

1. Introduction

Thorium utilization is an important aspect of Indian three stage nuclear power program. Construction of thorium based 300 MWe Advanced Heavy Water Reactor (AHWR) is an important step for this purpose. ThO$_2$ containing nearly 4% ^{233}UO$_2$ (composition in wt.%) is the proposed fuel for the Advanced Heavy Water Reactor (AHWR) [1,2]. The mixed oxide pellets are generally prepared by the conventional powder metallurgy route. The high gamma dose associated with daughter products of ^{232}U and the high specific radioactivity of ^{233}U makes fabrication of (Th,^{233}U)O$_2$ fuel difficult. The daughter products of ^{232}U (half life 68.9 y) are ^{212}Bi and ^{208}Tl, which emit strong gamma radiation of 1.8 MeV and 2.6 MeV, respectively [3]. Handling of ^{233}U bearing materials therefore, requires remote and automated operation in hot cells or shielded glove boxes to protect the operators from radiation [4-7]. Alternatively the process should be made

fast enough to avoid the accumulation of dose from the daughter nuclides of ^{232}U. The well established conventional 'Powder Oxide Pelletization' route is suitable for fabrication of high-density (Th, ^{233}U) O$_2$ pellets. It has, however, the disadvantage of 'radiotoxic dust hazard' as it involves handling of fine fuel particles. The conventional method has many mechanical steps such as mixing, milling, precompaction and final compaction which require automation at every stage of operation in shielded glove box facility to reduce dose. But, fine powders have poor flowability, which makes automation and remote fabrication difficult [4].

Other methods of fuel fabrication such as (a) Sol–Gel Microsphere Pelletization (SGMP), (b) Impregnation, and (c) Coated Agglomerate Pelletization (CAP) have been proposed to minimize the number of process steps requiring shielding operation, which in turn reduces the man-rem problem. The CAP route involves extrusion,

spherodization, coating of ThO$_2$ spheroids with desired amount of UO$_2$ powder, final compaction and sintering. Advantages of the CAP technique to produce (Th,U)O$_2$ fuel are [8]:

- Minimization of number of process steps which require shielding.

- Reduction of powder handling procedures.

- Reduction of man-rem to operators.

Despite these advantages, the CAP route has certain disadvantages such as sticking of U$_3$O$_8$ powder during coating to processing equipments and glove boxes, non-uniform microstructure and inhomogeneous uranium concentration in thoria matrix [9]. A new fabrication technique Impregnated Agglomerate Pelletization (IAP) has been developed at Advanced Fuel Fabrication Facility (AFFF), Bhabha Atomic Research Centre (BARC), Tarapur for making (Th,U)O$_2$ mixed oxide pellets. The main motive for developing the present IAP process was further to reduce powder-handling, man-rem and improve the homogeneity of fuel pellets.

This paper deals with the procedure for fabrication of Thoria based mixed oxide pellet by IAP route using ThO$_2$ spheroids and uranyl nitrate solution as the starting material and characterization of fuel pellets. (Th,U)O$_2$ pellet fabricated by IAP route was characterized by alpha autoradiography to verify distribution of fissile element which is criteria for the selection of manufacturing process [10]. The results obtained from the IAP route were compared with the properties of the pellets fabricated by CAP and POP route. In this work, natural U was used to simulate ^{233}U.

2. IAP process

Impregnated Agglomerate Pelletization (IAP) technique was developed at Advanced Fuel Fabrication Facility (AFFF), Bhabha Atomic Research Centre (BARC), which uses uranyl nitrate solution for coating instead of UO$_2$ powder used in

CAP route. The flow-sheet for fabrication of (Th,U)O$_2$ pellets by IAP process is divided into the work of shielded and unshielded facilities as shown in Fig. 1. The schematic diagram of IAP process is shown in Fig. 2. Characteristics such as apparent density, tap density of ThO$_2$ used in this study are given in Table 1. As received ThO$_2$ powder was milled in attritor at 200 rpm for 40 min using high chromium steel ball so as to break its platelet morphology. The milled ThO$_2$ powder was converted into free flowing spheroids by extrusion. The extrusion route involves mixing of milled ThO$_2$ powder with organic binder (polyethylene glycol), lubricant (oleic acid) and water in an appropriate proportion (1:1:8 wt.%) with the help of planetary mixer. The ThO$_2$ paste obtained was extruded through the perforated rollers. ThO$_2$ extrudes so obtained were dried by heating in an oven at 70–100°C for 1 h to achieve sufficient handling strength for spherodization. The dried extrudes were converted into the spheroids with the help of spherodiser. The spheroids obtained from spherodiser were sieved to remove the fines. All the above operations were carried out in normal alpha tight glove box facility, since only ThO$_2$ was handled up to the sieving stage.

The following operations were carried out in the shielded facility:

(a) Spray coating of ThO$_2$ spheroids with uranyl nitrate solution and drying of coated spheroids.

(b) Compaction of coated spheroids.

(c) Sintering in air and reducing atmosphere (N$_2$ + 7%H$_2$).

(d) Pellet loading and encapsulation into fuel rods.

BET surface area (m^2/kg)	3.72×10^{-3}
Apparent density (kg/m^3)	1.05×10^3
Tap density (kg/m^3)	1.262×10^3
Particle size (μm)	3.75
Total impurities (ppm)	< 1000

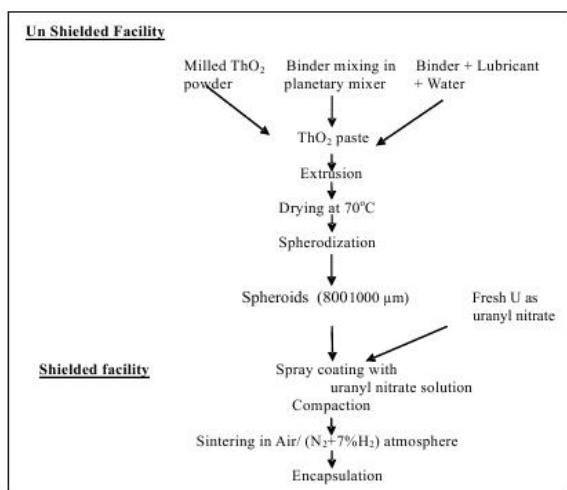***Table 1 Characteristics of starting ThO$_2$ powders***

Fig.1 Flow sheet for the fabrication of (Th,^{233}U)O$_2$ pellets by IAP process
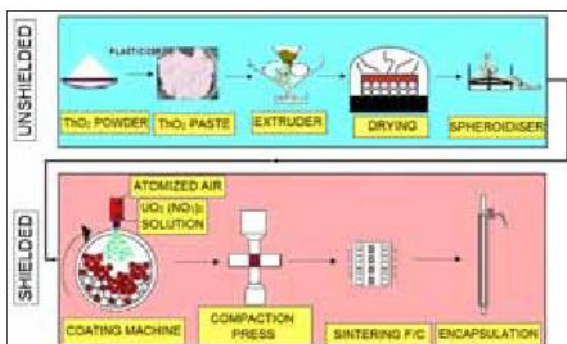

Fig.2 Schematic diagram of IAP process for fabrication of (Th,^{233}U)O$_2$ pellet.

3. Experimental

3.1 Extrusion and Spherodization

As received ThO$_2$ powder is milled in attritor at 200 rpm for 40 min using high chromium steel ball so as to break its platelet morphology. The milled ThO$_2$ powder is converted into free flowing agglomerate by extrusion route. The extrusion route involves mixing of milled ThO$_2$ powder with 1% organic binder (polyethylene glycol), 0.8 % lubricant (oleic acid) and 8 % water in desired proportion with the help of planetary mixer. The ThO$_2$ paste obtained

is extruded through the perforated rollers. ThO$_2$ extrudes so obtained are dried in an oven at 100°C for 2 hrs to achieve sufficient handling strength for spherodization. The dried extrudes are converted into the agglomerate with the help of spherodiser. Optimum organic emulsion addition eliminates the external lubrication requirement during compaction and helps in attaining good strength of pellet [11]. From Table 2 it is observed that agglomerates obtained through extrusion spherodisation route shows higher tap density and narrower particle size distribution.

Agglomerate	Binder %	Apparent density	Tap density	Size
Precompacts granules	2	2.54	3.34	- 20 #
Spheroids	2	2.70	3.44	< 1000 μm

Table 2 Physical characteristic of Agglomerate

3.2 Preparation of uranyl nitrate solution

Uranyl nitrate was prepare\d by dissolving a required amount of nuclear grade uranium dioxide (UO$_2$) powder in concentrated HNO$_3$ solution. The uranyl nitrate solution was evaporated and diluted with lower molarity HNO$_3$. The solution was analyzed for uranium content by both gravimetry as well as volumetric method. Gravimetric analysis was carried out with an aliquot of solution containing 150-200 mg of uranium. The aliquot was taken in a pre-weighted silica crucible. The sample was heated to 200°C till dryness and then to 800°C in air until a constant weight was obtained. The weight of the sample so obtained was taken as the weight of stoichiometric U$_3$O$_8$. Alternatively, uranium was also analyzed volumetrically in which an aliquot of the solution containing approximately 200 mg of uranium was first reduced from U (VI) to U (IV) by an excess of Fe (II) in concentrated H$_3$PO$_4$ medium. The selective oxidation of excess Fe (II) was carried out by HNO$_3$ in presence of Mo (VI) as a catalyst followed by titration of U (IV) with standard K$_2$Cr$_2$O$_7$ solution after dilution with 1 M H$_2$SO$_4$.

3.3 Coating of ThO$_2$ spheroids

Spray coating was also tried. Coating of uranyl nitrate solution on ThO$_2$ spheroids was carried out

in tablet coating pan with baffle rotating at 50 rpm. The spray nozzle which atomizes the uranyl nitrate solution in fine droplet with the help of compressed air was attached with the coating pan. The hot air dryer was also attached with the coating pan for drying the coated spheroids. The calculated amount of uranyl nitrate solution was spray coated on ThO$_2$ spheroids rotating in coating pan to achieve the desired composition. The amount of uranyl nitrate solution coated on ThO$_2$ spheroids was determined from weight gain of spheroids after coating.

3.4 Pelletization of coated ThO$_2$ spheroids and sintering

The coated spheroids containing 3 to 5 % UO$_2$ which had been prepared by IAP process using ThO$_2$ spheroids (1 mm size) and uranyl nitrate solution (2 M) were cold compacted into (Th,U)O$_2$ mixed oxide green pellets. The compaction pressure was varied from 250 to 300 MPa. The green density of the compacts was in the range 62-65% of the theoretical density. The green pellet was nominally 11.2 mm in diameter and 10 mm in length. The sintering of ThO$_2$-4%UO$_2$ pellets made by IAP route was carried out in air at 1400°C for 4 h. Pre-calcination treatment before sintering was not carried out for the pellets which were made in oxidizing atmosphere. However, the pellets which were made in reducing atmosphere were pre-calcined in air at 500°C for 2 h so as to convert uranyl nitrate to uranium oxide form i.e. UO$_2$ or U$_3$O$_8$. Afterwards, the pellets were sintered in reducing atmosphere at 1650°C for 4 h. The pellets sintered in air at 1400°C for 4 h had a nominal diameter of 9.6 mm and length 9 mm.

4. Results and discussion

(Th,U)O2 mixed oxide pellets were characterized by the following measurements:

- Geometrical density
- Thermogravimetry (O/M)
- Alpha-autoradiography

4.1 Density

The green and sintered density was measured geometrically. The density of the pellets sintered in oxidizing atmosphere (air) at 1400°C for 4 h was compared to that of the pellets sintered in reducing atmosphere (N$_2$+7%H$_2$) at 1650°C for 4 h (Table 3).

From the above results it was clear that high density (Th,U)O$_2$ pellet can be fabricated using IAP process. It was possible to make high density (Th,U)O$_2$ pellet by IAP process without addition of any conventional dopants such as Nb$_2$O$_5$, CaO and MgO. The density of (Th,3%U)O$_2$ pellets sintered in air at nearly 1400°C was 94.6 % TD.

In reducing atmosphere, however, a higher sintering temperature of 1650°C was needed to have the same composition, and the density was only approximately 90% TD (Table 3).

4.2 O/M ratio

O/M ratio of the sintered pellet was measured thermogravimetrically. The O/M ratio of pellet sintered in air was slightly higher than that of pellet sintered in reducing atmosphere due to the interstitial oxygen introduced into the fluorite lattice during sintering in air.

Composition	Density (%TD)		O/M ratio	
	Oxidizing	Reducing	Oxidizing	Reducing
(Th, 3%U)O$_2$	94.6	90.9	2.01	2.00
(Th, 3.75%U)O$_2$	93.1	91.4	2.01	2.00

Table 3 Density and O/M ratio of (Th,U)O$_2$ pellets sintered in oxidizing and reducing atmosphere

4.3 α-autoradiography

Macroscopic homogeneity i.e. the distribution of fissile element-rich particles was evaluated by means of alpha-autoradiography. The CR-39 film was initially immersed in hot water for 1 h and then pre-etched in 6 M KOH solution at 343 K for 4 h. The mounted specimen was ground and polished to get a uniform and flat surface layer. The pre-treated

alpha sensitive film was then put over the prepared specimen and fixed with the help of adhesive plastic tape. The inverted specimen was put over a smooth flat surface and a load was applied to have a close contact between the mount surface and the alpha film. After exposure for sufficient time, the film was removed and etched in 6 M KOH solution at 343 K for 1.5 h. Alpha-autoradiograph of the pellets fabricated by IAP route was compared with those of the pellets fabricated by CAP and POP route.

When the size of fissile element-rich particle is large, the temperature of the region around the particle rapidly increases under the condition of transient operation of reactor due to increase in localized fission reaction, which may lead to local melting in the worst case. The presence of fissile rich zone in the pellet affects the fuel performance as they act as hot spots generating high temperature. It enhances fission gas release resulting in increase of fuel pin internal pressure [12-13]. So it is necessary that the size of agglomerate should be as low as possible and its distribution through the matrix should be uniform.

Fig.3 shows α-autoradiograph of (Th,3.75%U)O$_2$ pellet fabricated by IAP route. Alpha-autoradiograph of IAP pellet sintered in air at 1400 °C showed uniform distribution of uranium in thorium matrix. It did not show any fissile rich or deficient area. On the other hand, the α-autoradiograph of (Th,3.75%U)O$_2$ pellet fabricated by CAP route showed non-uniform distribution of uranium in thorium matrix. The solid arrow in Fig.4 indicates fissile rich area in the pellet, while the dotted arrow indicates fissile deficient area. Fig.5 shows α-autoradiograph of (Th,4%U)O$_2$ pellet fabricated by POP route sintered in reducing atmosphere at 1650°C, which indicates the uniform distribution of uranium in thorium matrix. The homogeneity of the pellet fabricated by CAP route was slightly inferior as compared to that fabricated by POP route. From Figs.3 and 5 it is seen that the homogeneity of the IAP pellet sintered in air at 1400°C was comparable

to that of the pellet fabricated by POP route sintered in reducing (N$_2$+7% H$_2$) atmosphere at 1650°C.

From the above discussion it becomes clear that the homogeneity of the pellet fabricated by IAP route is better than that of the pellet fabricated by CAP route and comparable to that of the pellet fabricated through POP route.

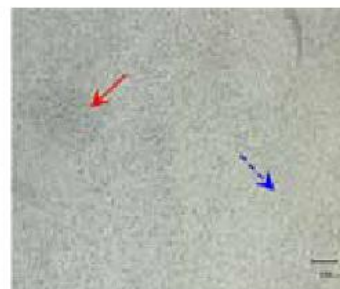*Fig.3 α-autoradiograph of (Th,3.75%U)O$_2$ pellet fabricated by IAP route sintered in air at 1400°C for 4 h*

Fig.4 α-autoradiograph of (Th,3.75%U)O$_2$ pellet fabricated by CAP route sintered in air at 1400°C for 4 h

Fig.5 α-autoradiograph of (Th,4%U)O$_2$ pellet fabricated by POP route sintered in N$_2$-7%H$_2$ at 1650°C for 4 h.

5. Advantages of IAP process

Advantages of IAP over CAP technique to produce (Th,U)O$_2$ mixed oxide fuel:

1. Reduction of powder handling procedures.

2. In the IAP process, highly radioactive ^{233}UO$_2$ powder, which tends to stick to processing equipments and may cause man-rem problem to operators, is not used. Moreover, the steps to use ^{233}U are decreased in the fabrication route.

3. The process can be coupled with the reprocessing plant. The use of purified uranyl nitrate fed from ion exchange columns for coating of ThO$_2$ spheroids may simplify the fuel reprocessing operations. This will eliminate precipitation or washing operations which were required to be carried out in shielded area and thus reduce the amount of radioactive waste produced.

Advantages of IAP over POP technique to produce (Th,U)O$_2$ mixed oxide fuel:

1. Reduction of powder handling procedures.

2. Reduction of man-rem to operators.

3. Reduction of the number of steps which requires shielding.

6. Conclusions

In this study it was demonstrated that high density ThO$_2$-UO$_2$ pellets can be fabricated by IAP route using ThO$_2$ spheroids and uranyl nitrate solution. The sintered pellet was characterized in terms of uranium distribution and grain size. The following conclusions have been drawn:

1. Homogeneity of pellet fabricated by IAP route was better than that by CAP route as the latter showed non-uniform distribution of uranium in thorium matrix.

2. Homogeneity of the pellet fabricated by IAP route sintered in air at 1400°C was as good as the pellet fabricated via the POP route which had been sintered in reducing (N$_2$-7%H$_2$) atmosphere at 1650°C.

The high sintered density, uniform microstructure, optimum grain size, good homogeneity, coupled with reduction of powder handling and man-rem indicate that the Impregnated Agglomerate Pelletization (IAP) method has emerged as a suitable alternative to the conventional powder oxide pelletization (POP) route for the fabrication of (Th,U)O$_2$ mixed oxide fuel.

References

1. A.Kakodkar, 46th General Conference of the International Atomic Energy Agency, IAEA, Vienna, 2002.

2. "Design and development of the AHWR—the Indian thorium fuelled innovative nuclear reactor", Nuclear Engineering and Design, Vol. 236, 683–700 (2006).

3. Nuclide 2000, version 2, BNM-CEA/DTA/LPRI<Nuclear and Atomic Decay Data, 30th June, (2004). Available from: www.bnm.fr.

4. "Thorium fuel cycle — Potential benefits and challenges", IAEA-TECDOC-1450, 49-64 May (2005).

5. Philip E. MacDonald, "Advanced Proliferation Resistant, Lower Cost, Uranium–Thorium Dioxide Fuels for Light Water Reactors", US Department of Energy Nuclear Energy Research Initiative, NERI 99-0153, (1999).

6. "Thorium fuel utilization: option and trends". IAEA-TECHDOC 1319, 69-76 November (2002).

7. Y. Alta and M. Eral et al. J.Nucl.Mater. Vol. 249, 46-51 (1997).

8. T.R.G. Kutty, K.B. Khan, P.S. Somayajulu, A.K. Sengupta, J.P. Panakkal, Arun Kumar and H.S. Kamath, J.Nucl.Mater. Vol. 373, 299–308 (2008).

9. T.R.G. Kutty, P.S. Somayajulu, K.B. Khan, Arun Kumar and H.S. Kamath, J.Nucl.Mater. Vol 384, 303–310 (2009).

10. H.S.Kamath, Proc.14th Annual Conference of Indian Nuclear Society, IGCAR, Kalpakkam, December, 17–19 (2003).

11. P.S.Somayajulu, Y.G.Nehete, P.D.Sughathan, S.Mishra, A.K.Mishra, Arun Kumar and H.S.Kamath, "New Technique in Powder Processing and Pelletization in Nuclear Fuel Fabrication", Trans. PMAI, 2000

12. A.G.Leyva, D.Vega, V.Trimacor and D.Mar, J.Nucl.Mater. Vol 303, 29. (2002).

13. Status and Advances in MOX Technology, Technical Report Series No. 415, 37-41, IAEA Vienna (2003).

CORROSION BEHAVIOR OF IN-SITU TiB-TiC REINFORCED TITANIUM MATRIX COMPOSITES

K. Srinivasa Vadayar[1], A. Jyothirmayi[2], V.V. Bhanu Prasad[3], G. Poshal[4]

[1] JNTUH, CEH, Hyderabad, India
[2] ARCI, Balapur, Hyderabad, India
[3] DMRL, Kanchanbagh, Hyderabad, India
[4] IARE, Dundigal, Hyderabad, India

Abstract: *Titanium Matrix Composites (TMCs) should have adequate corrosion resistance in air and acid environment apart from having good mechanical properties. The matrix microstructure, shape and vol.% of the reinforcement and interface play an important role in controlling these properties. Ti-(TiB+TiC) composites were prepared by sintering of titanium and B_4C (different sizes and vol.%) compacts. Corrosion behavior of unreinforced titanium and composites were investigated by Potentiodynamic test and Electrochemical Impedance Spectroscopy (EIS) in a simulated marine environment consisting of 3.5% NaCl solution. The study revealed that the composites exhibit marginally lower corrosion resistant than unreinforced titanium. In case of composites, corrosion resistance is found to be decreasing with decreasing B_4C particle size and increasing vol.% of the TiB-TiC reinforcement. This aspect is further established from impedance graphs. Preferential corrosion attack, possibly due to galvanic effect at the interface between second phase and the matrix is demonstrated through SEM studies.*

Keywords : *Titanium Matrix Composites, B_4C particle, corrosion, Potentiodynamic test, Electrochemical Impedance Spectroscopy.*

1. Introduction

Technology is taking great strides in areas of aero space, chemical, marine, thermal managing systems, electronic packaging system and recreational goods etc, thereby creating the necessary impetus for development of tailor made materials. Among the tailor made materials titanium matrix composites (TMCs) are leading in the forefront due to their inherent attractive characteristics like high temperature properties, wear resistance and oxidation resistance [1]. Some areas of use for titanium based composites in non aerospace areas are valve spring retainers and valves, automotive springs, steam turbine blades etc. [2-5]. Just as important as the mechanical properties of TMCs is their corrosion resistance. TMCs are multi component systems which introduce additional variables to the kinetics of corrosion during electrochemical activity.

The present work aims at determining the corrosion characteristics of Ti-(TiB+TiC) composites fabricated through pressureless sintering process using varying volume fractions and particle sizes of B_4C powders as initial reinforcements in de-aerated 3.5% NaCl solution at room temperature which simulates the marine environment. PDS & EIS tests were carried out. The study aims to understand the degradation mechanism of Ti-(TiB+TiC) composites, which causes loss of their properties under marine environmental conditions. The effect of initial B_4C particle size and volume fraction of TiB-TiC reinforcement on corrosion resistance of TMCs are also examined.

2.0 Experimental Study

2.1 Materials

The raw materials chosen for the preparation of the composites in the present work are powders

of commercially pure (CP grade) titanium (Ti) as matrix material, boron carbide (B₄C) as reinforcement. Titanium powder [d_{50} ≈13μm] was obtained from M/s Yasoda Special Metals Pvt Ltd, Hyderabad and was produced by Hydride-Dehydride route. The chemical composition of CP grade titanium powder is given in the Table 1. Three different sizes of boron carbide powders (500#, 800# and 1200#) were procured from M/s Electro Abrasives, USA.

Element	Fe	Mg	Ni	Cr	Si	P
Weight (%)	0.451	0.087	0.063	0.117	<0.005	0.0192
Element	C	O	N	H	Ti	
Weight (%)	0.058	1.15	0.08	0.0260	≈ 97.94	

Table 1 : Chemical analysis of the titanium powder

2.2 Synthesis of Composites

Ti-B₄C system was used to fabricate a composite having TiB and TiC as final reinforcements in the titanium matrix. The powder metallurgy process involving pressureless sintering was adopted for in-situ production of reinforcements. The in-situ reaction is

$$5\ Ti + B_4C \rightarrow 4\ TiB + TiC \qquad (1)$$
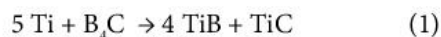
Initially excess titanium over and above the stiochiometric Ti content based on eq. (1) was taken so as to have metallic titanium matrix in which the in-situ formed TiB-TiC reinforcements are distributed. The initial contents of titanium and B₄C powders were so adjusted to have 10 to 30 vol.% reinforcement (TiB+TiC) in the final composites in the increments of 10 vol.%. The initial B₄C powders having mesh sizes of 500# [d_{50} ≈16μm], 800# [d_{50} ≈ 8μm] and 1200# [d_{50} ≈3μm] were used in synthesis of composites and d_{50} values of these powders are referred to as initial powder particle sizes for convenience. The powders of titanium and boron carbide in predetermined quantities were weighed using an electronic balance with an accuracy of ±

0.01 gm. The weighed powders were placed in a cylindrical plastic container and subjected to mixing for 24 hours using a roller mill rotating at 30 rpm. The blended powders were cold compacted into 25mm dia. x 20mm thick compacts at a pressure of 60 MPa for 30-45 seconds. The green compacts so obtained were subjected to pressureless sintering under 2x10⁻³ mbar vacuum at a temperature of 1723 K (1450°C) for a period of 1 hr. Sintering resulted in fully densified integral compacts which are free from cracks and warpage. Shrinkage of 16-18% has been observed in the dimensions of the cold compact as a result of sintering. For simplicity various samples fabricated were numbered using alphabets and prefixes as shown in Table 2. Unreinforced CP titanium was designated as 'A'. These designations were used throughout the text for brevity and simplicity.

Designation	Vol.% of (TiB+TiC) reinforcement	Particle size of B₄C	Vol.% of Ti matrix
A	--	--	100
B₃₀	30	# 500 (16 μm)	70
B₂₀	20	# 500 (16 μm)	80
B₁₀	10	# 500 (16 μm)	90
C₃₀	30	# 800 (8 μm)	70
C₂₀	20	# 800 (8 μm)	80
C₁₀	10	# 800 (8 μm)	90
D₃₀	30	# 1200 (3 μm)	70
D₂₀	20	# 1200 (3 μm)	80
D₁₀	10	# 1200 (3 μm)	90

Table 2 : Designation of different composites under study based on initial B₄C particle size and final reinforcement vol.%

2.3 Specimen Preparation

Disc specimens of 14 mm diameter and 3 mm thickness cut from the composites were mounted in epoxy and polished using various grits of 200, 400 and 600 followed by cleaning with distilled water and then with acetone. These specimens were exposed to the corrosive environment in such away that the exposed surface area of the specimen was 1 cm². Potentiodynamic polarization measurements and electrochemical tests were carried out for

corrosion studies. The corrosion test cell had the classic configuration of three electrodes a Platinum electrode as counter electrode, a saturated calomel electrode as reference electrode and the coated metallic sample composite sample as working electrode shown in Fig. 1. For this all samples were immersed for 1 hour in 3.5% NaCl solution purged with N_2 gas. Polarization data and impedance data were collected using a computer controlled Solartron Electrochemical interface (Model SI 1286) and Impedance analyzer (Model SI 1260). Potentiodynamic scans were performed by applying potentials from -1v to +2.5v open circuit potential (OCP) with a scan rate of 1 mV/s. Corrware and Corrwiew software are used for performing experiment and analyzing the data respectively.
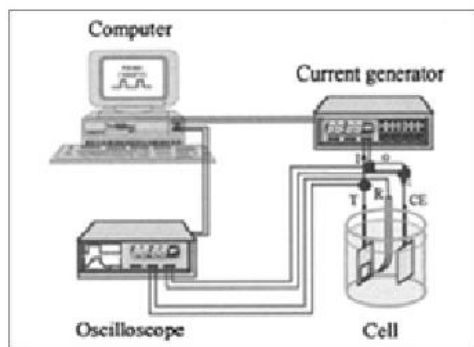
Fig. 1 : Schematic diagram of electrochemical testing equipment

The electrochemical impedance scan was carried out using an AC signal of 10 mV amplitude applied over a bandwidth from 100 kHz to 0.01 Hz. at OCP through Z plot software. The data obtained is given in the form of Bode plots. The impedance data is fitted with suitable equivalent circuit models using Zview2 software and the results were analyzed. All the tests were carried out three times to check the reproducibility. After the corrosion test the samples were examined by SEM to study the nature of corrosion attack.

3. Results & Discussion:

The influence of initial B_4C particle size and reinforcement volume (TiB + TiC) in titanium matrix composites on corrosion behavior were investigated by potentio dynamic polarization method and electrochemical impedance spectroscopy (EIS).

Figs. 2, 3 and 4 illustrates the potentiodynamic polarization plots for B, C and D composites with varying volume fraction of reinforcement in comparison with bulk titanium. One common feature among Figs. 2 to 4 is that, the transpassive region decreased and the corresponding current density increased to higher values at a constant potential with increasing volume fraction of reinforcement compared to CP titanium. Upon analyzing the polarization test results, the parameters such as corrosion current and polarization resistance can be obtained and the same can be utilized for quantification of corrosion magnitude. The outcome of such an exercise is presented in Fig. 5.
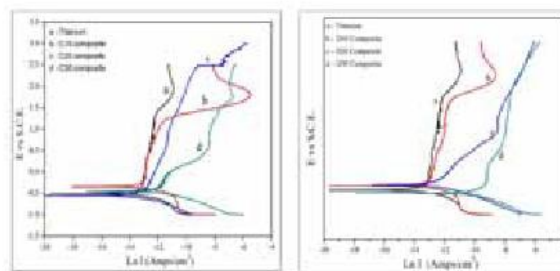

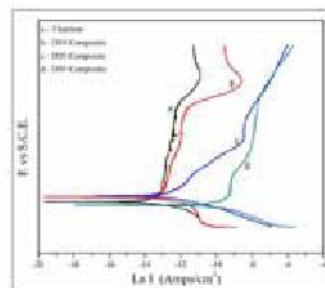*Fig. 2 : Polarization curves for B composites*

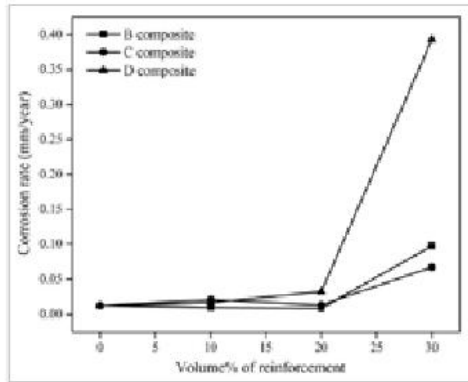*Fig. 3 : Polarization curves for C composites*

Fig. 4 : Polarization curves for D composites

The variation of corrosion current I_{corr} a measure of corrosion rate, as a function of vol. fraction of reinforcement is shown in Fig. 5. Although I_{corr} increased marginally up to 20 volume% of reinforcement, subsequently I_{corr} increased significantly at 30 vol.%. Amongst the composites, F composite clearly depicts highest corrosion current. The effect can be depicted more clearly in Fig. 6 wherein, the corrosion rate (mm/year) is plotted against the particle size. It is clear from Fig. 6 that 30 volume% reinforced titanium exhibits highest corrosion rate as illustrated above. Thus, it is clear that the presence of reinforcement decreased the overall corrosion resistance of titanium.
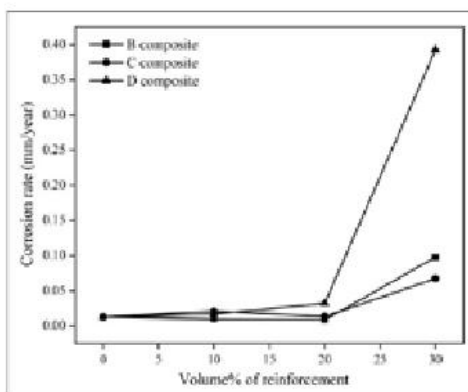

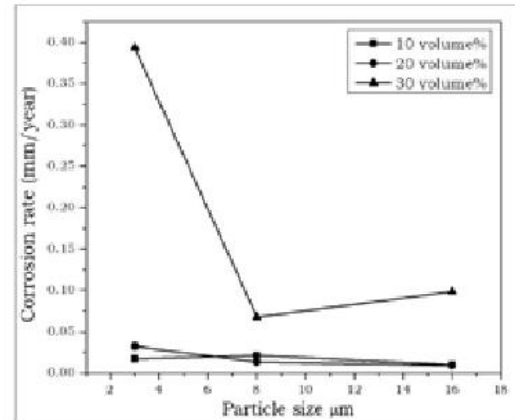*Fig. 5: Corrosion rate vs. volume% of reinforcements of the B, C and D composites*

Fig. 6 : Corrosion rate vs. particle size

Covino & Alman. [6] studied corrosion of titanium matrix composites and revealed that the sintered titanium (d_{50} 44 μm) showed an active passive behavior and no trans passive region in their potentiodynamic polarization studies in acidic medium and varying temperatures[6]. The polarization curves for Ti + TiC and Ti + TiB$_2$ composites showed increased currents for higher particulate concentrations and at higher temperatures. Secondary passivation peaks were observed in the Ti + TiC composites which was not shown in the Ti + TiB$_2$ composites due to the presence of TiC phase in the former composite.

The more insight can be brought in by means of micrographic analysis of samples after the corrosion tests. Towards this purpose, the corroded samples were subjected to SEM examination after removing them from the solution, cleaning in distilled water and drying under hot air. Fig. 7 illustrates the SEM micrograph of unreinforced titanium. A clear grain boundary attack is visible. It might be due to the fact that grain boundaries are high energy sites and can easily be attacked under the corrosive environment. The presence of Fe in CP grade titanium as an impurity (Table 1) also contributes to corrosion process by galvanic effect. However, titanium always has natural oxide film over its

surface which protects it from corrosive attack. Therefore, the presence of higher passive region as seen in Fig. 2 is thus understandable. On the other hand when reinforced titanium composite is subjected to corrosion, the presence of secondary phases contributes to corrosion activity by providing easy sites for attack by the way of galvanic effect as these phases are more noble in nature as compared to CP titanium. If this is true, then the corrosive attack should take place at the interface between reinforcement and the Ti matrix. To get more insight into this aspect, the titanium matrix composites were also subjected to SEM analysis. Fig. 8 illustrates the SEM micrograph of B_{10} composite after the corrosion test. The presence of corrosion activity at the reinforcement and titanium matrix is clearly evident. Thus, the higher the volume% of reinforcement, the less would be the area fraction of passive film over titanium. Therefore, such relatively lower passivation drives the material towards corrosion attack. The less is the size of particles the more is the surface area under attack. Therefore with the increase in volume%, the passive region decreased to lower potential with concurrent increase in current density as illustrated in Figs.2 to 4. Thus, the increased corrosion rate can be quite understandable.
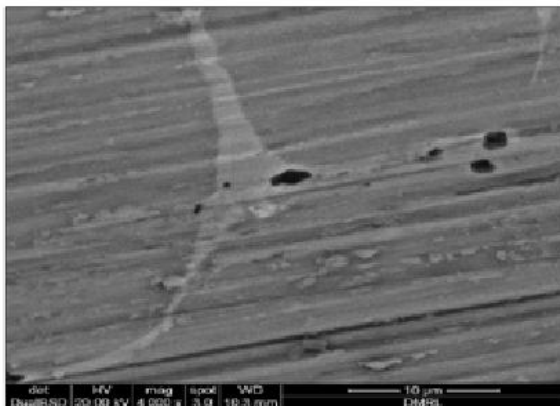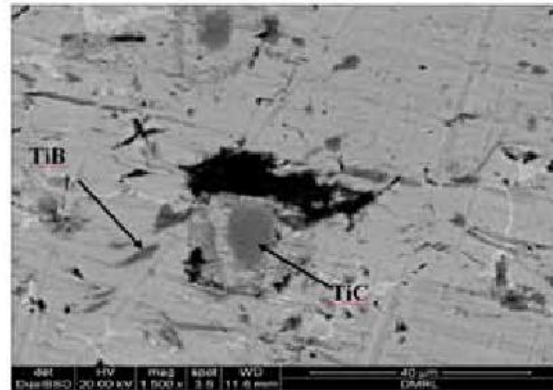

Fig. 8 : SEM image of B_{10} composite after corrosion

Although above analysis provides a clear evidence of corrosion mechanism in titanium matrix composites, it did not provide the mechanistic approach to corrosion. For that purpose, electrochemical impedance analysis was carried out on the same samples just before polarization tests in 3.5% NaCl. The electrochemical impedance spectra obtained after perturbation of 10 mV are presented in the form of Bode plots. Fig. 9 (a) - (b), Figure 10 (a)-(b) and Fig. 11 (a)-(b) represents bode plots for B, C and D composites respectively. The charge transfer resistance obtained after fitting RC circuit is depicted in Fig. 12.
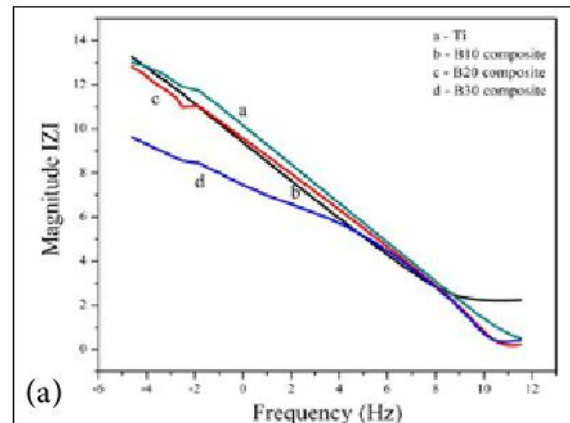
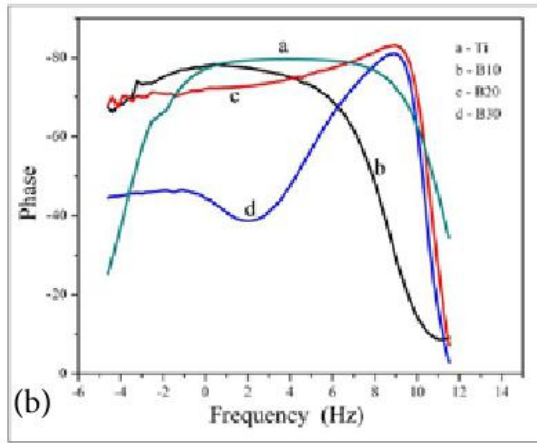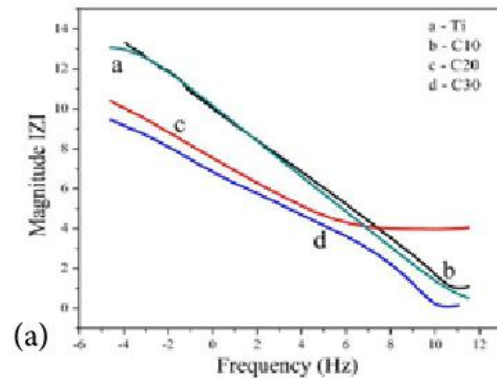*Fig. 7 : SEM image of titanium after corrosion*

*Fig. 9: Bode plots for B composites (a) Magnitude
vs. frequency (b) Phase vs. frequency*

*Fig. 11 : Bode plots for D composites (a)
Magnitude vs. frequency (b) Phase vs. frequency*

*Fig. 10: Bode plots for C composites (a)
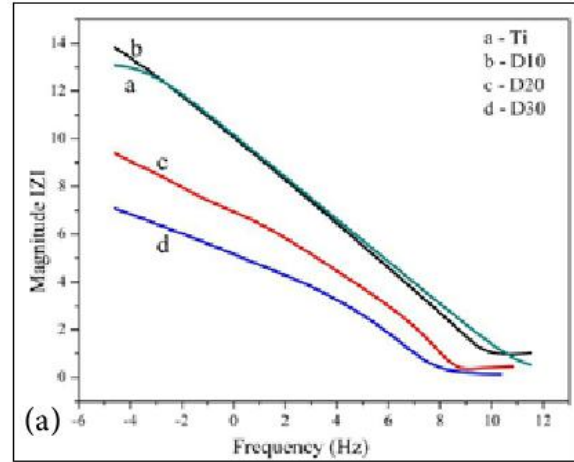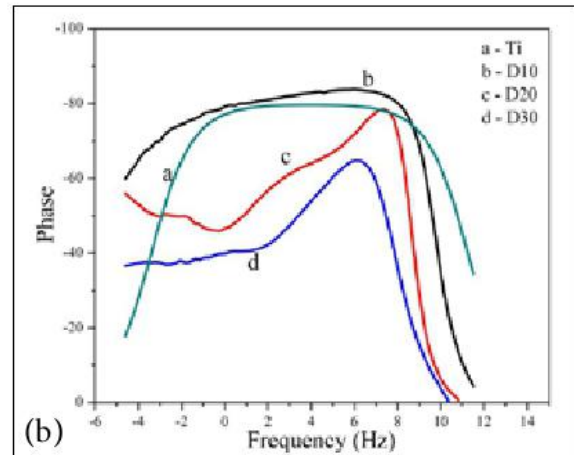Magnitude vs. frequency   (b) Phase vs. frequency*

*Fig. 12 : Rct vs. volume% of reinforcement of the
composites*

The perusal of Figs. 9 to 12 suggests the following :

(a) CP Ti clearly depicts single time constant (1 RC combination) and highest impedance.

(b) Two time constants (2 RC combinations) were observed in Ti reinforced composites. The second time constant becomes distinctly noticeable with the increase in volume% of second phase.

(c) The magnitude of impedance decreased with increase in volume% of reinforcement.

The presence of single time constant in titanium is due to the presence of highly passive film on its surface. Therefore titanium exhibits highest impedance among all the composites. If the mechanism of corrosion process as examined and proposed based on the polarization and corresponding post corrosion SEM examination of titanium matrix composites is true, the presence of active interface between the matrix and second phase should reflect as a second time constant during the impedance analysis. In line with this explanation, the appearance of second time constant with the increase in volume% of reinforcement is due to the interface between titanium and reinforcement. Due to presence of reinforcement the passive film over titanium is not continuous thereby indicating lower impedance (Fig. 10). Therefore, the higher the volume% of reinforcement, the higher the interfacial attack between matrix and second phase and the lower would be the corresponding impedance.

4. Conclusions :

The PDS method revealed the increase in corrosion current density and the start of passivation easily with increase in volume% of second phase for all composites. Increasing volume% of second phase increases the propensity to corrosion by providing easy sites (active) for localization. The interface between second phase and the matrix is attacked preferentially, may be due to galvanic effect. From impedance graphs it can be concluded that the pure titanium shows passive (capacitive) behavior. Increasing volume% of second phase clearly delineates two time constants thereby providing direct evidence of interfacial attack. The second time constant becomes more pronounced with increasing volume% of second phase.

References :

1. S. Ranganath, J. Mater. Sci. Vol. 32, 1-16 (1997).

2. S. R. Seagle, Mater. Sci.Eng. Vol. A 213, 1-7 (1996).

3. M. Yamada, Mater. Sci.Eng. Vol. A 213, 8-15 (1996).

4. R. Vandermark, JOM, Vol. 49 (6), 24-27 (1997).

5. S. M. Abkowitz, P. Weihrauch, H. L. Heussi and S. Abkowitz, The Institute Materials London: (1996).

6. B. S. Covino and D. E. Alman Albany Research Center, U.S. Department of Energy, Albany, OR USA, DOE/ARC-02-011.

INVESTIGATION ON PIEZOELECTRIC AND DIELECTRIC PROPERTIES OF Sr DOPED BNKT CERAMICS

S. Rastogi[1], P. Divya[2], B. Praveenkumar[2], Ashavani Kumar[3]
[1]DRDO HQ, NewDelhi, India
[2]PZT Centre, Armament Research and Development Establishment, Pune , India
[3]Dept of Physics, National Institute of Technology, Kurukshetra, India

Abstract: *Lead zirconate titanate ceramics with exceptional dielectric and piezoelectric properties are causing lead pollution and environmental problems because of high toxicity of lead oxide and its volatility during heat treatment. Currently the research trend is towards the development of lead-free piezoelectric ceramics with reasonable piezoelectric properties. In the present paper lead-free piezoelectric ceramics BNKT, $Bi_{0.5}(Na_{0.85}K_{0.15})1-xSrxTiO_3$(where x=0, 0.02, 0.04, 0.06) are prepared by conventional solid state route. XRD studies are carried out to confirm the perovskite crystal structure. Calcination studies are carried out to optimize the properties. The powders are pressed into disc shape of 10 mm diameter and 1.0 mm thickness. The green bodies are sintered around 1200ºC to improve the density. The relative densities of all the samples are determined by Archimedes method. The effect of Sr doping on piezoelectric properties like piezoelectric charge coefficient (d33), and coupling coefficient (Kp) are discussed. Dielectric properties are studied by varying the strontium (Sr) doping. Partial doping of Sr on BNKT ceramic improved the piezoelectric and dielectric properties substantially. The electric measurements reveal that the ceramic with x=0.04 & 0.06 has better piezoelectric and dielectric properties. The obtained properties are piezoelectric charge coefficient (d33), 140 pC/N, dielectric constant (ε), 850 and dielectric loss (tan δ), 0.045. The developed BNKT ceramics are highly used in sensing, energy converting and energy generating applications.*

Keywords: BNKT; Dielectric; Piezoelectric; XRD.

Introduction

Lead free piezoceramics are namely of three types tungsten bronze type, bismuth layered structure and perovskite type ferroelectrics. Except perovskite these structure have small piezoelectric properties [1]. The perovskite type ceramics seem to be suitable for actuator and sensor applications. On the other hand bismuth layered structured ferroelectric ceramics seem to be a good material for ceramics filter and resonator application [2]. Perovskite structured $Bi_{0.5}Na_{0.5}TiO_3$ [BNT] ceramics as reported by Jaffe are considered as one of the promising candidates which have properties comparable to PZT that dominates the market of piezoceramics. PZT materials generally contain more than 60 wt % lead. Lead is a heavy metal and its toxicity is well known. Some of the symptoms of lead poisoning are headaches, constipation, nausea, anemia and reduced fertility etc. Continuous uncontrolled exposure could cause more serious symptoms such as nerve, brain and kidney damage. The toxicity of lead oxide and its high vapor pressure during sintering process not only causes environmental pollution but also generates instability in composition and electrical properties. Even if the production is well managed environmentally the whole life cycle of the material needs to be considered including the end-of- life stage where PZT containing waste might end up in corrosive conditions. This must be taken seriously especially in case of large volume consumer application [3]. Hence extensive research is being carried out to develop lead free piezoceramics.

BNT has large remnant polarization, P_r (38µC/cm^2), high Curie temperature, T_c (320˚C), low piezoelectric charge coefficient d_{33} (58pC/N) and high coercive field E_c (7.3 kV/mm) compared to PZT ceramics [5, 6]. To improve the ferroelectric and piezoelectric properties lots of other perovskite ferroelectrics have been added into BNT to form new BNT based solid solutions such as BNT-BaTiO$_3$, BNT-Bi$_{0.5}$K$_{0.5}$TiO$_3$, BNT-BaTiO$_3$-Bi$_{0.5}$Li$_{0.5}$TiO$_3$, BNT-Ba(Ti,Zr)O$_3$, (Bi$_{0.5}$Na$_{0.5}$)Ti1-x(Zn$_{0.3}$Nb$_{0.6}$)xO$_3$, BNT-BT-La$_{0.5}$Na$_{0.5}$TiO$_3$ etc. Among these BNT-BT and BNT-BKT are studied intensively because of simple processing route and high piezoelectric properties [4-10]. BNT-BKT forms a complex perovskite structure with a mixed A site occupation of (bismuth, Sodium and potassium) and titanium as single ion in B site. BNT and BKT forms solid solutions of various crystal symmetries, depending on the ratio of BNT to BKT. Higher amounts of BNT forms rhombohedral phase while BKT rich compositions are tetragonal. The morphotropic phase boundary is located between ratio 15 to 20% of BKT where optimized piezoelectric parameters are obtained [11-13]. Doping of BNKT ceramics with La, Li, Pr, Ce, Co, Ta etc. has been studied by few researchers [1, 5 and 14] to obtain improved dielectric and piezoelectric properties. In the current paper, the work is dedicated towards the study of dielectric and piezoelectric properties of Sr doped BNKT ceramics.

Experimental

The conventional solid state ceramic fabrication technique was used to prepare BNKT based ceramics. Bi$_2$O$_3$, TiO$_2$, Na$_2$CO$_3$, K$_2$CO$_3$ and SrCO$_3$ were the raw materials (> 99% purity) used for preparing stoichiometric composition, Bi0.5 (Na$_{0.85}$K$_{0.15}$)]$_{1-x}$Sr$_x$TiO$_3$ (where x=0, 0.02, 0.04, 0.06). Raw materials were mixed in a ball mill using zirconia media for 24 h in ethanol. After mixing the suspension was poured into metallic dishes and ethanol was evaporated by keeping it in hot air oven for 6 h at 120˚C. The dried mixture was calcined at 1020˚C for 2.5 h and again mixed in ball mill

for better homogeneity. Discs of 10 mm diameter and 1.2 mm thickness were compacted by using hydraulic press. XRD analysis of the powder was carried out to confirm the phase formation (D8, Bruker). These pellets were sintered at temperature in the range of 1175- 1225˚C. The densities of the sintered pellets were measured by using Archimedes method. The pellets were electroded with silver paste and subsequently poled by applying high DC field of 4.5 kV/mm at 60˚C. Dielectric properties of the pellets were measured using dielectric spectrometer (Novacontrol, Germany). Piezoelectric properties were measured using d_{33} meter (Berlincourt, UK).

Results and Discussion

XRD patterns of BNKT and Sr doped ceramics are shown in Fig 1. It is observed that the ceramics possess a pure perovskite phase and there is no other secondary impurity phase is present. It also reveals that Sr has diffused into BNKT lattice to form a new solid solution. A slight broadening of peaks are observed in Sr doped BNKT ceramics which may be due to decrease in grain size.

The variation of density with increase in Sr content is shown in Fig. 2. It is observed that density increases with Sr content in BNKT ceramics. The increase in density can be explained by defect chemistry and vacancies. Increase in Sr content leads to increase in oxygen vacancies and better diffusion of Sr doping, which results in denser ceramics. But continuous increase in Sr (> 3%) content results in saturation of density.
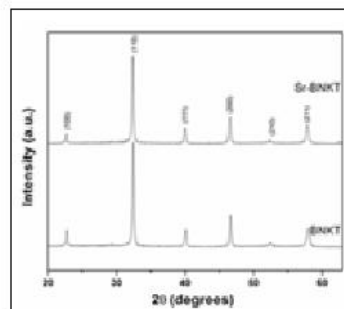

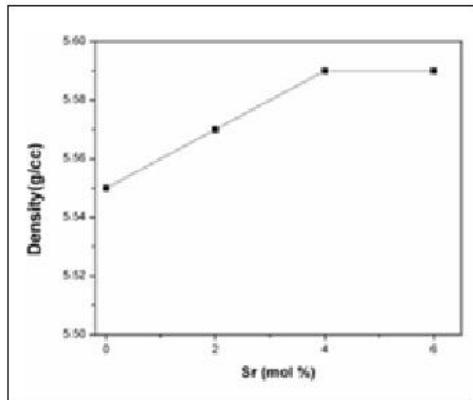*Fig. 1 XRD pattern of BNKT and Sr. Doped BNKT ceramics*

Fig. 2 Variation of density with Sr content

The variation of dielectric constant with Sr content measured at frequency of 1 kHz is shown in fig. 3. It is observed that dielectric constant increases with increase in Sr content. The result indicates that Sr^{2+} ions replace similar sized A site cations such as K^+, Na^+ and/ or Bi^{3+} ions rather than smaller B site cations (Ti^{4+}). The ionic size of Sr^{2+}, Bi^{3+}, Na^+, K^+ and Ti^{4+} are 12.7 nm, 13.6 nm, 13.9 nm, 16.4 nm and 6.4 nm respectively [14]. The increase in dielectric constant with Sr is due to the (i) increase in density, (ii) broader XRD peaks (iii) decrease in grain size and (iv) long range interaction of dipoles. The finer grain size leads to higher dipole-dipole interaction, polarization and domain wall motion.
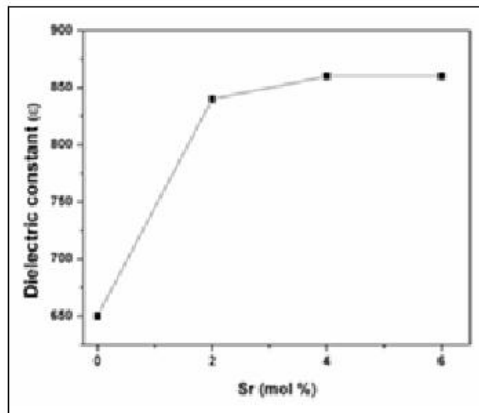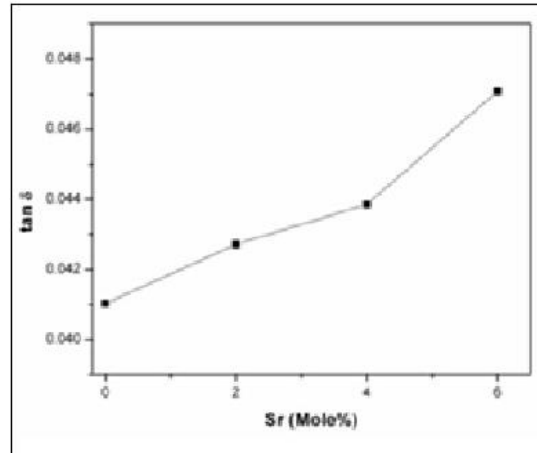

Fig. 4 Variation of dielectric loss with Sr content

The variation of dielectric loss with Sr content measured at frequency of 1 kHz is shown in fig. 4. It is observed that dielectric loss increases with increase in Sr content. It is common with the partial addition of dopant increases the conductivity (high concentration of charge carriers) of the material which in turn increases the dielectric loss. It is possibly due to the addition of Sr the conduction current and the conduction of absorption current increase resulting in increase in dielectric loss [15].
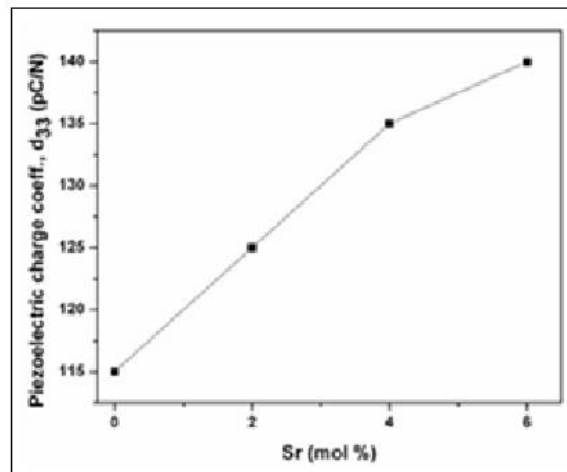

Fig. 3 Variation of dielectric constant with Sr content

Fig. 5 Variation of piezoelectric charge coefficient with Sr content

Fig. 5 shows the variation of piezoelectric charge coefficient with Sr content. The piezoelectric charge coefficient increases with increase in Sr content. Increase in piezoelectric charge coefficient is due to the increase in the density of ceramics. Increase in Sr content, increases the probability of spontaneously aligned dipoles in one of the equilibrium position which gives rise to piezoelectric response of the materials. The modification of BNKT with Sr causes more disordering in the system, which causes increased the piezoelectric charge coefficient.

Conclusions:

In this paper, Sr doping on $Bi_{0.5}$ $(Na_{0.85}K_{0.15})]_{1-x}Sr_xTiO_3$ (where x=0, 0.02, 0.04, 0.06) ceramics were studied as superior candidates for lead free piezoelectric materials to reduce environmental damage. Lead-free BNKT ceramics were prepared successfully using solid state route. The effects of variation of Sr substitution on structural, dielectric and piezoelectric properties were investigated. XRD revealed broader peak for Sr doped BNKT samples. The dielectric and piezoelectric properties of BNKT ceramics had increased with Sr doping. This material was considered to be one of the essential candidates for sensing and actuating applications.

Reference:

1. J. Yoo, D. Oh, Y. Jeong, J. Hong and M. Jung "Dielectric and piezoelectric characteristic of lead free $Ba_{0.5}(Na_{0.84}K_{0.16})_{0.5}TiO_3$ substituted by with Sr", Materials Letters Vol. 58, 3831-3835 (2004).

2. T. Takenaka and H. Nagata, "Current status and prospects of lead free piezoelectric ceramics"Journal of the European Ceramics Society, Vol. 25, 2693-2700 (2005).

3. E. Ringgaard, T. Wurlitzer, "Lead-free piezoceramics based on alkali niobates" Journal of the European Ceramics Society, Vol. 25, 2701-2706 (2005).

4. Y. Saito, H. Takao, T. Tani, T. Nonoyama, K. Takatori, T. Homma, T. Nagaya and M. Nakamura, "Lead-free piezoceramics", Nature Vol. 432, 84-87 (2004).

5. A.Herabut, A. Safari, "Processing and Electromechanical Properties of $(Bi_{0.5}Na_{0.5})(1-1.5x)La_xTiO_3$ Ceramics", Journal of American Ceramics Society, Vol. 80, (11), 2954–2958, (1997).

6. N. Feng, L. Laihui, P.Xiaoyin, Z.Yuepin and C.Hongbing, "Piezoelectric and dielectric properties of BiNaTiO-BiKTiO-BaCaTiO lead-free piezoelectric ceramics", Journal of Materials Science, Vol. 47 (7), 3354-3360 (2012).

7. T. Takenaka, K. Maruyama and K. Sakata, "$(Bi_{1/2}Na_{1/2})TiO_3$-$BaTiO_3$ System for Lead-Free Piezoelectric Ceramics", Japanese Journal of Applied Physics, Vol. 30, 2236-2239 (1991).

8. Z. T. Huang, Rong-Xia ; S. X. Zhong, P. Fei, G. J. Yong, C. L. Ying, G. H. Shuang and H. Yun-Bin, "Lead-free In_2O_3-doped $(Bi_{0.5}Na_{0.5})_{0.93}Ba_{0.07}TiO_3$ ceramics synthesized by direct reaction sintering", Applied Physics Letters, Vol. 90, (18) 182903 – 182906 (2007).

9. A.Sasaki, T. Chiba, Y. Mamiya and E. Otsuk, "Dielectric and Piezoelectric Properties of $(Bi_{0.5}Na_{0.5})TiO_3$–$(Bi_{0.5}K_{0.5})TiO_3$ Systems", Japanese Journal of Applied Physics, Vol. 38, 5564-5567 (1999).

10. Q. Zheng, C. Xu, D. Lin, D. Gao and K. W. Kwok, "Piezoelectric and ferroelectric properties of $(Bi_{0.94-x}La_xNa_{0.94})_{0.5}Ba_{0.06}TiO_3$ lead-free ceramics", Journal Physics D: Applied Physics, Vol. 41, 125411 (2008).

11. Y. Hiruma, K. Yoshii, H.T. Nagata and T. Takenaka, "Phase transition temperature and electrical properties of $Bi_{0.5}Na_{0.5}TiO_3$-$Bi_{0.5}A_{0.5}TiO_3$ (A=Li, K) lead free ferroelectric ceramics", Journal of Applied Physics, Vol. 103 (8), 084121 (2008)

12. V. A. Isupov, "Ferroelectric $Na_{0.5}Bi_{0.5}TiO_3$ and $K_{0.5}Bi_{0.5}TiO_3$ perovskite and their solid Solution", Ferroelectrics Vol. 315, 123-47 (2005)

13. L. A. Schmitt, J. Kling, M. Hinterstein, M. Hoelzel, W. Jo, H. Kleebe, et. al. "Structural investigation on lead free $Bi_{0.5}Na_{0.5}TiO_3$ based Piezoceramics", Journal of material science, Vol. 46 (12), 4368-78 (2011).

14. N.B. Do, H. B. Lee, C. H. Yoon, J. K. Kang, and J. S. Lee, "Effect of Ta-Substitution on the Ferroelectric and Piezoelectric Properties of $Bi_{0.5}(Na_{0.82}K_{0.18})_{0.5}TiO_3$ Ceramics", Transactions on Electrical and Electronic Materials, Vol. 12 (2), 64-67, (2011).

15. B. Tarrev, Physics of dielectric materials, Mir Publisher, Moscow

IT SOLUTIONS TO WAREHOUSE DESIGN APPROACH FOR ITS COST EFFECTIVE OPERATIONS

Y. V. Satya Kumar[1], Yogendra Singh[2]

[1]School of Engineering and Technology, Ansal University, Gurgaon, NCR, India.
[2]Formerly w/ School of Engineering & Technology, Sharda University, Greater NOIDA, India.

Abstract: Increased and spiraling demand for a more variety and higher volumes of the products with the ever present constraint of available space are pushing the need of optimum warehouse (re)design and its cost effective operations. IT solutions may significantly increase the efficiency and effectiveness of warehouse design process and operation through decreased labor efforts, chances for error and time needed for order picking. The paper presents the use of IT Tools in design of Warehouse and its inherent functions of inventory maintenance and order picking. Optimization of most aspects of warehouse is done by developing a computerized generic warehouse layout design that can be adapted by any industry and also tweaked for specific requirements. The ultimate goal of such optimization is to balance long term capital costs such as land and infrastructure for the Warehouse and short term functional costs such as material handling and labor consistent with projected growth.
Keywords: Warehouse design, Redesign, Information Technology (IT), PM Industry, Order Picking.

1. Introduction

Warehousing is essentially a comprehensive storage and logistics solution for efficiently attaining the organizational objectives of different kinds of entities, be they from core industry, service industry, online stores, call-to-order services, front lines of defense corps, not-for-profit organizations or emergency response agencies [1]. Warehouses must be flexible structures to provide quality, efficiency and effectiveness of the logistics operations in a very demanding, competitive and uncertain market [2]. The main aspects of a warehouse could include material handling system, warehouse operators, manual labor, maneuvering space, racks and stocks to store. An efficient and robust warehouse must balance among the costs associated with all these factors to keep operating costs down, while improving the customer service and satisfaction. The need to redesign may arise from increased volume or variety or both of products leading to a slower material movement with extra handling and heavier costs [3], an outcome which small companies cannot bear.

Use of Computer Software/ Information Technology (IT) may exponentially decrease design team's efforts. With the improvements in IT, it becomes possible to develop tools to handle warehouse and inventory issues more efficiently [4]. This may add costs to operation administration, but this cost is comparatively justified with higher profits. IT is one of the most important factors enabling effective supply-chain management [5], while guaranteeing enhanced organizational performance [6]. Several researchers have found evidence that IT is associated not only with improvement in productivity and economic growth [7]. The recent advances in IT provide many challenges and opportunities for getting inventory management right [8].

The wider use of computation and simulation [sic] (in PM Industry) has resulted in reducing the cost and processing time, while providing improved quality [9]. Computerized systems automate continual inventory monitoring functions, which become economical and efficient to implement [8]. This paper presents how Computer Software/ IT may be used in warehouse design, inventory

maintenance, material tracking and material delivery. A computerized generic design of a warehouse is presented which may be tweaked for specific requirements of a particular warehouse.

2. Research Background

2.1. Warehouse Design

The design of a warehouse is a highly complex problem, which includes a large number of interrelated decisions [10,11]. Singh and Kumar proposed [1] an integrated and lean approach to warehouse design by optimization of Material Handling, Space and Labor requirements with decreased company operating cost and better customer service and with a balance among the capital, functional and maintenance costs. In USA, the capital and operating costs of warehouses is about 22% of logistics costs [12] and around 25% in Europe [13]. As observed in the USA [14], the value of wholesale trade inventories is approximately half a trillion dollars [15] and inventory maintaining costs (interest, taxes, depreciation, insurance, obsolescence and warehousing) in 2004 have been estimated at 332 billion dollars [16]. North America, Europe and Japan are amongst the major PM parts users in automotives with the usage exceeding over 70% of the total market [17].

2.2. IT in Warehouse Design and Operations

Govindraj et al., summarized [18] computer-based tutors from the works of others [19-23] in use for the past 30 years and under improvement with advances in computing, instructional systems design, artificial intelligence and the cognitive science. Rapid development of computing hardware and solvers for optimization, simulation, and general mathematical problems, one might reasonably expect a more robust design-centric research literature [14]. Hung and Fisk presented [24] economic sizing of warehouse with the help of Linear Programming. Perlmann and Bailey developed [25] Computer-Aided Design software allowing a warehouse

design team to quickly generate a set of conceptual design alternatives. Rushton et al. presented [26] Computer Simulation to test the impact of different volume throughputs and identify the consequences on the rest of the Supply Chain, while Rowley presented [27] evaluation and assessing expected performance. Roodbergen and De Koster developed [28] an algorithm for a warehouse with three cross aisles, one in the front, one in the back, and one in the middle. Ito et al. proposed [29] an intelligent agent based system to model warehouse. Use of computer tools such as OL09 and specific modeling language IDEF0 in warehouse designing has been discussed by Kostrzewski [30]. Baker and Canassa summarized [31] the tools used in each warehouse design step. According to De Koster et al. [32] random storage policy will only work in a computer-controlled environment. More automation may reduce labor cost, but increase the investment cost [33]. Use of IT and computer software may ease warehouse operations in conjunction with complete automation and retrieval system, but due to high associated costs, integration of IT and Automation is not recommended for small scale facilities.

2.3. PM Industry Growth Potential

PM industry has its roots in 1900s since the production of tungsten filament for lamp industry and the growth potential of PM in 21st century is enormous [9] and the industry worldwide should develop global technology, statistics and standards for global technology exchange. Utilization of PM parts in automotive has increased steadily in the past decade [17].

3. Functions of Warehouse

Bartholdi and Hackman presented [34] four main reasons why warehouses are useful. Primary functions include [18] receiving, storage, order picking and consolidation, packing, and shipping and in some cases other functions such as value-added operations. They may also serve to accumulation and sorting [35], customization [36],

as a mixing point [37], to recover products, materials, and product carriers from customers to redistribute to other customers, recyclers and OEMs [38] and to transport to workstations, seal out of season products [39]. A warehouse does this by being an interface between demand and supply of the raw material, products, components, accessories, by-products, tools, consumables and donations in kind [1]. Fig. 1 shows streamlining of operations and their dependence on warehouse especially in the context of Automobile and P/M industry [1]. The Functional Structure of Warehouse [40] is shown in Fig. 2.
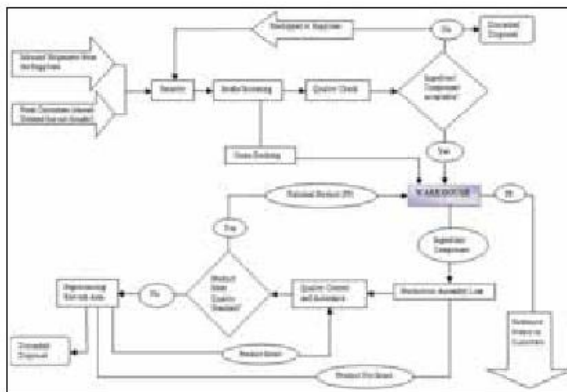

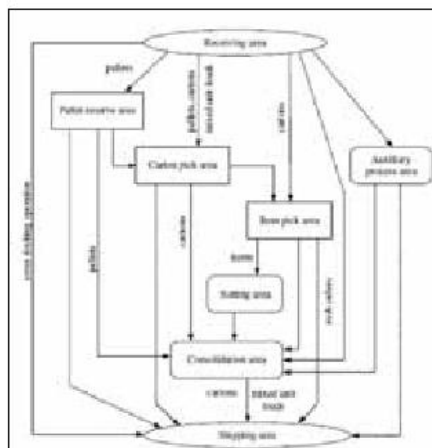*Fig. 1 Streamlining of Operations of Warehouse [1]*

Fig. 2 Functional Structure of Warehouse [40]

4. IT Solutions in Approaches to Warehouse Design

Design often requires a mixture of analytical skills and creativity [10]. Computer Software/IT Solutions have proved to be catalysts in accelerating the speed and delivery efficiency of researchers and designers resulting in increased accuracy and reliability of various functions.

4.1. Data Gathering and Analysis

4.1.1. Data Gathering: Hatton referred to use of software by some design companies to extract data from company computer systems [41]. Computerized information systems provide large historical datasets to use in the design process [42]. The kinds of data required for warehouse design had been discussed recently [1]. Data can be gathered from software such as SAP, ERP, MRP and past production history and requirements etc. The data may also be gathered by online surveys and questionnaires filled by warehouse stakeholders (warehouse manager, operators or supply personnel and production personnel) or even sourced from operation statistics.

4.1.2. Analysis: Design starts with the analysis of information provided via different databases: an item master, an inventory master, vendor shipment history and order master [43]. It may contain analysis of Part Grouping to define a Design Principle, exceptions to Design Principle and defining Trade-off Principle with optimum Labor & Material Flow and Space Utilization.

A. Design Principle/ Grouping: Design of a warehouse is a complex problem due to the large number of interrelated decisions sometimes with conflicting objectives [35]. Each part can be given a number according to its priority and frequency of use such as nnnn.hp for high priority, nnnn.hf for high frequency and correspondingly nnnn.mp and

nnnn.mf for medium and nnnn.lp and nnnn.lf for low. Here, n should be an integer for easy computer sorting. This will allow segregating all the parts with high accuracy and reliability within seconds. According to Singh and Kumar [1] Design Principle can be based on any of three criteria, i) relational grouping, ii) alpha-numerical order of part name / number and iii) priority and frequency of use. As per them a typical Grouping sequence for a PM Industry may be a) expensive parts, b) explosive or highly reactive powders and gases, c) contact frequency and complementary parts, d) heavier parts, e) stackable parts or non-stackable parts and f) alphabetical order or their part number.

B. Trade-off Principle: Microsoft Excel appears to be constrained in sorting only upon one basis. Software can be developed that can sort based on more than one criterion with a given sequence priority to each base to tradeoff among them.

a. Priority of Item vs. Frequency of Use: Different scenarios may be studied by computer simulation of parts and cost associated with the priority and frequency use. Software may be developed which can count costs associated with each and every part per unit of storage time and the loss due to delay at times with different possible scenarios. Priority may be based on the inherent value of the part, availability in the market, geographical distance of the supplier, complexity or hassles in procurement, unforeseen volatile situations that could make a part a priority item, emergency-related/ safety-maintenance equipment among other possibilities. While trading-off it becomes easier to take decisions based on cost (qualitative analysis rather than quantitative analysis, although quantitative may be more rigorous in its analysis).
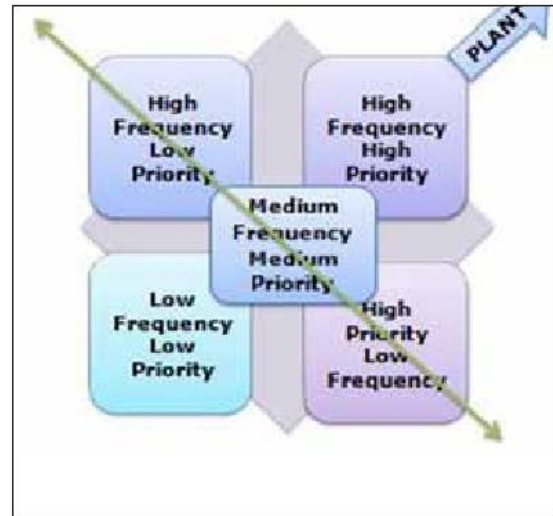

Fig. 3 Priority vs. Frequency Metric [1]

Parts associated with higher monetary value may be kept near manufacturing/ assembly facility. Fig. 3 illustrates the design decision strategy for five different such options or combinations.

4.1.3. Material and Labor Flow Analysis: Material along with its associated overhead accounts for approximately 55% of product costs [44]. Harit and Taylor introduced simulation as 45] a feasible, inclusive, and cost-effective means of evaluating alternative solution approaches and equipment components and presented framework for the design and analysis of large scale material handling systems. As proposed recently Eq. 1 illustrates the close interdependent relationship among labor costs, travel time and travel distance [1].

labor costs α travel time α travel distance --(Eq. 1)

This will lead to a holistic warehouse design with integration of optimized space, reduction of labor and material handling, more efficient operators and fork lift drivers, increased accessibility and thus reduced operating heads with optimized investment to maintain adequate reserve.
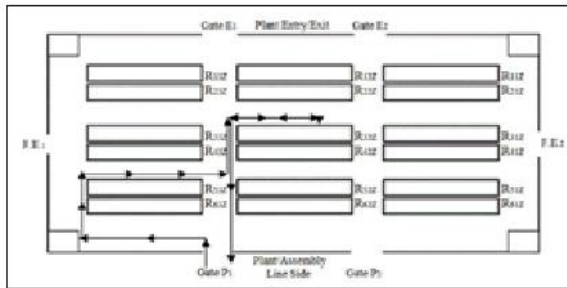
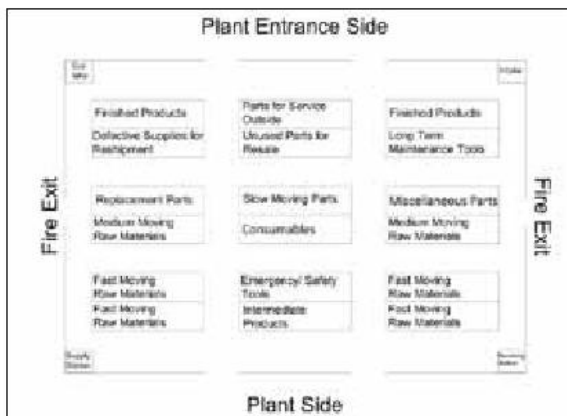*Fig. 4 Proposed Material and Labor Flow Analysis*

Fig. 5 Generic Warehouse Layout [1]

While looking at material and labor flow for multiple activities such as receiving, sorting, indexing, stacking, issuing, picking, packing and shipping, Time-Cost optimization should be considered. Fig. 4 shows a typical material and labor flow analysis for a manual operated or semi-automated warehouse, whereas Fig. 5 visualizes a generic warehouse layout design especially for PM Industry. Siemens PLM Software provides for material flow simulation which can further optimize material flow [46].

4.1.4. Computation and Iterations: Errors and limitations associated with tedious computations and consequent decision making by design team may be eliminated by the use of computational and statistical software. From the data gathered

$$N_b` = Q_{max}/Q_b \text{ --------------------------------(Eq. 2)}$$

where, Qmax, quantity to be stored,

Q_b, maximum quantity per box/carton and

N_b, is number of boxes to be stored

Rounding off the value of $N_b`$ will yield N_b.

The designer may use spreadsheets, such as MS Excel to speed-up arithmetic calculations, improve reliability and accuracy and reduce drudgery. Suggested templates for the calculation of required number of boxes are provided in Table 1 and Table 2, which are extensions of proposals made earlier [1].

Table 1: Template for Calculation of Required No. of Boxes for Storage in Warehouse (in Design)

Table 2: Template for Final Placement of any Part for Storage

4.1.5. Draft, Design and Visualization: 2-D design software such as AutoCAD can be used for graphical representation. By using AutoCAD, the designer may draft the top view of each sub-rack and front view of each rack to provide inputs about utilization of space and volume respectively for use by warehouse designer and operators. Even a 3-D model is even more desirable for real time depiction of space availability, volume utilization and actual positioning or picking of parts.

4.2. Iterative Simulation of Design Alternatives:

With the help of looped algorithms the optimum operation of proposed design can be examined before implementation for best possible accessibility.

Createsoft developed Simcad Pro Simulation Software for warehouses with the capabilities to simulate slotting, picking, receiving, congestion analysis, capacity planning, facility layout & design and ERP/WMS connectivity with optimization of schedule, staffing, congestion, slotting, picking, receiving and overall warehouse efficiency.

5. IT Solutions to Real-time Warehouse Operations

A WMS (Ware House Management System) is a set of software that directs almost all activities in the warehouse, including receiving, put away, location of storage areas, order picking, electronic data interchange with trading partners, and inventory tracking [8]. Software algorithms taking care of order grouping and release, storage slot allocation, pick location allocation, planning shipments, sequencing pick instructions, and routing order pickers are used to realize the desired performance [47]. It is proposed that degree of automation possible is limited by the capital cost and access to financing sources.

5.1. Three Dimensional Visualization

For mapping and 3D visualization of warehouse layout and storage protocols, a walkthrough virtual warehouse may be developed for each final design with size, shape and location of each storage rack and its sub-racks, volume, size and shape of each carton/bin or even of non-packageable parts. With such functional software, it would be possible to track in real time, the occupancy and available options. Many ware houses use locator systems, which is computer software that directs where any given part or product should be stored [8]. Fig. 6 is such a proposed 3-d configuration with a logical indexing scheme for easy location of parts and can be based on the 2-D layout provided in Fig. 5. The proposed scheme for indexing in Fig. 6 and Fig. 4 has 3 subscripts, with the 1st subscript referring to x-coordinate (no. of row, from plant entrance
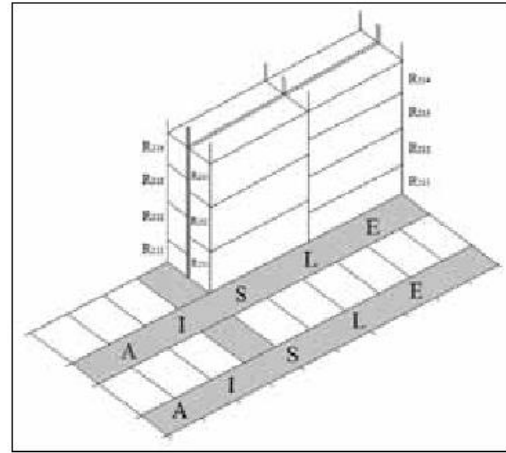

Fig. 6 Proposed 3-D Configuration and Indexing

side to plant side), 2nd subscript to y-coordinate (no. of column, from right to left) and the 3rd to z-coordinate (no. of sub-rack, from floor to ceiling).

5.2. Inventory Records

With the help of SAP, ERP, MRP the inventory record management could be very easily handled. Inventory management software permits the warehouse to have real-time information on the inventory status of all items in the warehouse [8].

5.3. Order Picking

Bar code system allows the order picker to simply run use a wand across the cases to be selected, which then confirms whether the correct item was selected in the proper quantity and may be associated by Radio Frequency (RF) system [8]. Computer tools may also be used to determine shortest order picking route [32,48]. Goetschalckx, and Ratliff presented [49] an algorithm which can be implemented in real time on a microcomputer to determine the optimal number and location of stops and to specify the items to be picked at each stop. Automated and robotized picking is only used in special cases (e.g. valuable, small and delicate items) due to its high capital investment [32]. RF

technology may further be extended using GPS systems to direct the order pickers to the right rack even, especially in Warehouses that are very huge as in the case of Online stores such as Amazon.

6. Conclusions

Warehouse design is a complex process due to the different constraints and variables. There may not be one best design solution in the strictest sense, but a clutch of optimal solutions, which can be arrived at much more easily using IT and computing power. The optimal warehousing approach and indexing schemes should allow even unskilled and semi-skilled operators to be able to easily go about their routine work without any errors being committed while storing or order picking. Simple 3-D visualization schemes may be developed along the lines suggested by each individual manufacturing unit and its associated warehouse based on their specific needs and demands and avoiding any recourse to expensive branded software solutions in this non-productive leg of the manufacturing process.

References

1. Y. Singh and Y.V.S. Kumar, 'An Integrated and Lean Approach to Warehouse Design by Optimization of Material Handling, Space and Labor Requirements', In: PM-13 Intl. Conf., PMAI, Pune, India, 07-09 Feb (2013).

2. C.A.S. Geraldes, M.S.F.B.S. Carvalho and G.A.B. Pereira, 'A Warehouse Design Decision Model -Case Study', IEEE (2008).

3. A.J. Briggs, Material Handling and Packaging Series: Warehouse Operations Planning and Management, John Wiley & Sons, 101-134 (1960).

4. G. Strack and Y. Pochet, 'An Integrated Model for Warehouse and Inventory Planning', European Jl. of Operational Research, Vol. 204, 35–50 (2010).

5. J. Hammant, 'Information Technology Trends in Logistics', Logistics Information Mgmt., Vol. 8, No. 6, 32 – 37 (1995).

6. F. Wu, S. Yeniyurt, D. Kim and S.T. Cavusgil, 'The Impact of Information Technology on Supply Chain Capabilities and Firm Performance: A Resource-Based View', Industrial Marketing Mgmt., Vol. 35, No. (4), 2006, 493–504 (2006).

7. E. Brynjolfsson and S. Yang, 'Information Technology and Productivity: A Review of the Literature', Advances in Computers, Vol. 43, 179–214 (1996).

8. J. T. Mentzer, M. B. Myers and T. P. Stank, Handbook of Global Supply Chain Management: Warehouse Management', SAGE Knowledge, 185-203 (2007.)

9. P. Ramakrishnan, 'Powder Metallurgy- The 21st Century Technology', Trans. of Powder Metallurgy Association of India: Sp. Vol. Powder Metallurgy for the 21st Century, 1-12 (2008).

10. B. Rouwenhorst, B. Reuter, V. Stockrahm, G. van Houtum, R. Mantel, and W. Zijm, 'Warehouse Design and Control: Framework and Literature Review', European Jl. of Operational Research, Vol. 122, No. 3, 515–533 (2000).

11. S. Heragu et al., 'Mathematical Model for Warehouse Design and Product Allocation', Intl. Jl. of Production Research, Vol. 43, No. 2, 432-440 (2005).

12. Establish Inc., Herbert W. Davis & Co., 'Logistic Cost and Service', In: Council of Supply Chain Managers Conference (2005).

13. ELA European Logistics Association/ AT Kearney Management Consultants, Differentiation for Performance, Deutscher Verkehrs-Verlag GmbH, Hamburg (2004).

14. J.X. Gu, M. Goetschalckx and L.F. McGinnis, 'Research on Warehouse Design and Performance Evaluation: A Comprehensive Review,' European Jl. of Operational Research, Vol. 203, 539–549 (2010).

15. BEA, Table 5.7.5B. Private Inventories and Domestic Final Sales by Industry (2008). http://bea.gov/national/nipaweb/TableView.asp?SelectedTable=153&FirstYear=2005&LastYear=2007&Freq=Qtr>

16. P.A. Trunick, 'Can we hold the line on Logistics Costs?' Logistics Today (2005). <http://www.logisticstoday.com/displayStory.asp?sNO=7359>.

17. D. Shende and V. Hariharan, 'Powder Metal Part Use- Auto OEM's Perspective,' Trans. of Powder Metallurgy Association of India, Vol. 36, 62-65 (2010).

18. T. Govindaraj, E.E. Blanco, D.A. Bodner, M. Goetschalckx, L.F. McGinnis and G.P. Sharp, 'An Online Tutor for Warehouse Design,' In: Proc. of 2000 IEEE Intl. Conf. on Systems, Man, and Cybernetics, 8–11 Oct, Nashville, Tennessee, USA, 1158–1162 (2000).

19. D.L. Bitzer and D. Skaperdas, 'Plato IV- an Economically Viable Large Scale Computer-based Education System,' in Proc. of the Natl. Electronics Conf., Dec 9–11, 1968, Chicago, IL, 351– 356 (1968).

20. D.L. Bitzer and R.L. Johnson, 'Plato- a Computer-based System used in the Engineering of Education,' Proc. of the IEEE, Vol. 59, No. 6, 960–96 (1971).

21. D. Sleeman and J.S. Brown, Eds., Intelligent Tutoring Systems, London: Academic Press (1982).

22. B.P. Woolf and D.D. McDonald, 'Building a Computer Tutor: Design Issues,' IEEE Computer, Vol. 17, No. 9, 61–73 (1984).

23. J.D. Hollan, E.L. Hutchins and L. Weitzman, 'STEAMER: an Interactive Inspectable Simulation based Training System,' AI Magazine, Vol. 5, No. 2, 15–27 (1985).

24. M.S. Hung, and J.C. Fisk, 'Economic Sizing of Warehouses : a Linear Programming Approach,' Computers & Operations Research, Vol. 11, No. 1, 13-18 (1984).

25. A.M. Perlmann, M. Bailey,'Warehouse Logistics Systems – A CAD Model,' Engineering Costs and Production Economics, Vol. 13, 229–237 (1988).

26. A. Rushton, J. Oxley and P. Croucher, The Handbook of Logistics and Distribution Management, 2nd ed., Kogan Page, London (2000).

27. J. Rowley, The Principles of Warehouse Design, 2nd ed., the Institute of Logistics & Transport, Corby (2000).

28. K.J. Roodbergen and R. De Koster, 'Routing Order-pickers in a Warehouse with a Middle Aisle,' European J. of Operational Research, Vol. 133, 32-43 (2001).

29. T. Ito, J. Abadi,S.M. Mousavi, 'Agent-based Material Handling and Inventory Planning in Warehouse,' J. of Intelligent Manufacturing, Vol. 13, No. 3, 201–210 (2002).

30. M. Kostrzewski, 'The Procedure of Warehouses Designing as an Integral Part of the Warehouses Designing Method and the Designing Software,' Intl. Jl. of Mathematical Models and Methods in Applied Sciences, Vol. 6, No. 4, 535-543 (2012).

31. P. Baker and M. Canessa,'Warehouse Design: A Structured Approach,' European Jl. of Operational Research, Vol. 193, 425–436 (2009).

32. R. De Koster, T. Le-Duc and K.J. Roodbergen, 'Design and Control of Warehouse Order Picking: a Literature Review,' European Jl. of Operational Research, Vol. 182, No. 2, 481-501 (2007).

33. L.F. McGinnis, M. Goetschalckx, G. Sharp, D. Bodner and T. Govindaraj, 'Rethinking Warehouse Design Research,' Proc. of 2000 Intl. Material Handling Research Colloquium (2000).

34. J. Bartholdi and S. Hackman, Warehouse & Distribution Science, Release 0.76. (2006). http://www.warehouse-science.com.

35. C.A.S. Geraldes, M.S.F.B.S. Carvalho and G.A.B. Pereira, 'A Warehouse Design Decision Model -Case Study,' IEEE (2008).

36. R.J.V. Stull, 'Re-Design Warehouse Plant Layout for a Food Company,' M.S. Thesis, U. of Wisconsin-Stout, U.S.A. (2004).

37. R. Akila and N. Thangavel, N., 'A Study on Warehouse Space Optimization with Reference to Pepsico India Holdings Pvt. Ltd.', Mamandur, India (2011-12).

38. R. De Koster, M.P. De Brito and M. Van de Vendel, 'Return Handling: An Exploratory Study with Nine Retailer Warehouses,' Intl. Jl. of Retail & Distribution Mgmt., Vol. 30, No. 8/9, 407-421. (2002).

39. D.E. Mulcahy, Warehouse Distribution and Operations Handbook, McGraw Hill (1994).

40. G. Salvendy, Ed. Handbook of Industrial Engineering: Technology and Operations Management. 3rd ed. John Wiley & Sons, Inc., Chap 81, 2083-2109 (2001).

41. G. Hatton, 'Designing a Warehouse or Distribution Centre,' In: The Gower Handbook of Logistics and Distribution Management, Gattorna, J.L. (Ed.), Fourth ed., Gower Publishing, Aldershot, 175–193 (1990).

42. D. Bodner, T. Govindaraj, K.N. Karathur, N.F. Zerangue and L.F. McGinnis, 'A Process Model and Support Tools for Warehouse Design,' In: Proc. of 2002 NSF Design, Service and Manufacturing Grantees and Research Conf. (2002).

43. T. Govindaraj, E. Blanco, D. Bodner, L. Goetschalckx, L. McGinnis and P. Sharp, 'Design of Warehousing and Distribution Systems: An Object Model of Facilities, Functions and Information,' In: Proc. of 2000 IEEE Intl. Conf. on Systems, Man, and Cybernetics, 8–11 Oct, Nashville, Tennessee, USA, 1099–1104 (2000).

44. P. Gabbert and D. E. Brown, 'Knowledge Based Computer Aided Design of Material Handling System,' IEEE Trans. on Systems, Man, and Cybernetics, Vol. 19, No. 2, 188-195 (1989).

45. S. Harit, and G. D. Taylor, 'Framework for the Design and Analysis of Large Scale Material Handling Systems,' 1995 Winter Simulation Conf., Dec 3-6, Arlington, VA, USA, 889-894 (1995).

46. SIEMENS, 2010, 'Material Flow Simulation' online blog release: (viewed, 3 March, 2014) http://blog.industrysoftware.automation. siemens.com/blog/tag/material-flow-simulation/; crosslink to original site of http://www.plm.automation.siemens.com/en_us/products/tecnomatix/plant_design/plant_simulation.shtml

47. R. De Koster, 'Warehouse Math', Liber amicorum. In memoriam, Eds. Jo van Nunen, L. Kroon, T. L, R. Zuidwijk, Dinalog Breda, 179-186, (2010).

48. R. De Koster and E.S. Van der Poort, 'Routing Orderpickers in a Warehouse: a Comparison between Optimal and Heuristic Solutions,' IIE Transactions, Vol. 30, 469-480. (1998).

49. M. Goetschalckx and H.D. Ratliff, 'An Efficient Algorithm to Cluster Order Picking Items in a Wide Aisle,' Engineering Costs and Production Economics, Vol. 13, No. 4, 263–271 (1988).